



HELLENIC REPUBLIC

**National and Kapodistrian
University of Athens**

EST. 1837



**UNIVERSITÉ
DE GENÈVE**

FACULTÉ DES SCIENCES
Section des sciences de la Terre
et de l'environnement

Ore mineralogy of the Serifos Granodiorite, Cyclades, Greece: Genetic relationship with the skarn deposit at southwestern Serifos



Dimitrios Xypnitos

Master of Science

October 2019

*Supervisor: Panagiotis Voudouris, Professor
Faculty of Geology and Geoenvironment, NKUA*

*Co-supervisors: Kalin Kouzmanov, Lecturer/Senior Research Scientist
Department of Earth Sciences, University of Geneva*

*Andreas Magganas, Professor
Faculty of Geology and Geoenvironment, NKUA*



Erasmus+

Table of Contents

Abstract.....	3
Acknowledgments.....	4
I.Introduction-Aim of the Thesis.....	4
II. Analytical methods.....	8
III.Gelological setting.....	8
IV.Local geology and field work.....	11
Chora prospect.....	13
Koutalas-Ganema prospect.....	14
Sotiras prospect.....	18
Kefala Hill prospect.....	20
Heliport prospect.....	20
V. Results.....	22
V.1. Optical microscopy and petrography.....	21
V.2. Ore mineralogy.....	29
V.3. Mineral identification.....	31
V.4. Raman Spectroscopy.....	32
V.5. Mineral chemistry.....	36
Feldspars.....	36
Biotites.....	40
Amphibole.....	48
Titanite.....	52
V.6. Cold Cathodoluminescence (CL).....	54
V.7. Fluid inclusion analysis.....	58
Fluid inclusion petrography.....	58
Fluid inclusion microthermometry.....	65
VI. Discussion.....	70
VII. Conclusions.....	74
References.....	76

Abstract

The Serifos district is part of the Attico-Cycladic-Pelagonian ore belt. The island is known for mining activity through the ancient times and in the last century (1880-1950), mainly exploiting an Fe-skarn deposits, as described by Salemink (1985) and Ducoux et al. (2017). Three tectono-metamorphic units have been distinguished in the island, from the bottom to the top the Continental Cycladic Basement (CCB): the Cycladic Blueschist Unit (CBU) and the Upper Cycladic Unit (UCU) along with an I-type granodiorite intrusion emplaced at 11,6 to 9,5 Ma penetrating the rocks of the CCB and the CBU units and causing contact metamorphism in the proximal marbles and schists, consequently forming calcic exo- and endo-skarns as long as carbonate-replacement ores and retrograde low-temperature veins. In the southeastern part of the island, another igneous body crops out, described recently by Voudouris (2010) as "leucogranite" and called "aplogranite" in this study. The present study has been focused on five mineralized areas within the granodiorite and the aplogranite bodies. The first prospect is located in the Chora area within the inner part of the granodiorite and consists of disseminated pyrite and chalcopyrite mineralization, along with goethite pseudomorphs after pyrite and magnetite as veins. Secondary malachite and azurite also occur in this area. The second prospect is a sheeted quartz vein system located in the Koutalas area, within the outer part of the granodiorite. The sheeted veins trend E-W and represent a possible pathway (e.g. feeder zones) for the magmatic aqueous fluids migrating laterally and upwards within the marbles of the CBU. The third prospect in the Sotiras area within the aplogranite, is characterized by a disseminated pyrite mineralization where pyrite occurs inside miarolitic cavities. Large quartz veins without ore minerals also occur in this area. The fourth prospect is located in the Kefala area and is characterized by pyrite dissemination within the aplogranite. Finally, the fifth prospect in the Heliport area in the inner part of the granodiorite, is a sulfide stockwork-type mineralization consisting mainly of quartz pyrite, chalcopyrite and Ti-oxides (anatase/rutile). In one sample, native bismuth and bismuth sulfosalt have been found. In the Koutalas prospect, an extended sodic alteration affects the granodiorite, while in the Heliport area a less intense sericitic alteration occurs. No such alterations have been found in the Sotiras area where the aplogranite is the dominant body. Moreover, we provide new microthermometric data from the quartz sheeted veins in the Koutalas area and from the quartz veins in the Sotiras area. The measured inclusions present a range of homogenization temperatures from 200° to 550°C with a mean temperature of 350°C, while the measured salinity ranges from 5 to 45 wt% NaCl equiv. The major goal of this study is to understand how the relationship between all these prospects and their possible genetic relation with the skarn mineralization in the southwestern part of Serifos.

Acknowledgments

For the preparation of this study I would like to thank first of all my parents for all the psychological and financial support, the professors Panagiotis Voudouris and Andreas Magganas for supervising this study at the University of Athens and Dr. Kalin Kouzmanov for all the assistance, support and supervising this study at the University of Geneva. Special thanks to all the academic and technical staff from both universities, mainly for the use of the analytical facilities required for this study.

I. Introduction and aim of the thesis

The Serifos ore district is part of the Attic-Cycladic-Pelagonian ore belt, which includes significant base- and precious-metal mineralization among other in Lavrion, south Evia, Sifnos, Tinos and Milos islands (Marinos and Petrascheck 1956; Skarpelis 2002; Neubauer, 2005; Tombros et al., 2007; Voudouris et al. 2008a,b, 2011, 2019; Bonsall et al. 2011; Alfieris et al. 2013; Scheffer et al. 2017; Fitros et al. 2018; Menant et al. 2018). These ore deposits are genetically related to magmatic rocks of Miocene to Pleistocene age.

The island of Serifos, is widely known for the existence of mining activity through the ancient times and during the second half of the 19th century since the first half of the 20th century (~1880- 1950). It was later described by Salemink (1985) and Ducoux et al. (2017), that a Fe-skarn deposit was responsible for the existence of mining activity on the island. Both studies were focused on the genetic link between the skarn deposit and the adjacent Serifos granodiorite. At the same time, the large igneous body located in the central part of the island was studied from petrological, tectonic, mineralogical, and geochemical perspectives. The purpose of those studies was mainly the correlation between the Serifos granodiorite and other igneous bodies located in the Attico-Cycladic Massif, like the Lavrion granodiorite and the integration of these bodies into a unique geotectonic model of magma emplacement in the Hellenides belt.

Porphyry deposits are considered to be the most significant source of Cu and Mo and a very important source of Au, Ag, W, Sn as by-products. Although porphyry deposits were in the previous decades described as disseminated, sulfide mineralization can mostly be found in stockwork veins, sheeted veins, hydrothermal breccia etc. Furthermore, recent studies have shown that the magmatic source of the hydrothermal fluids responsible for the formation of the porphyry deposits, also play a crucial role for the formation of proximal or distal skarn deposits, carbonate-replacement bodies and of course epithermal deposits located in shallower depths (Seedorf et al., 2005, 2008; Sillitoe, 2010) (Fig. 1). Sillitoe (2010) proposed a unified model, where hydrothermal activity was the main ore-generating process and in which porphyry, epithermal, proximal skarn, carbonate-replacement and distal Carlin-style deposits along with other granite-related systems were all connected. Such a system is proposed for Serifos island, where the skarn as the main ore deposit, is being fed by a magmatic source, in our case the Serifos granodiorite. The granodiorite itself, is the main part of this unified system, where the sheeted veins along with the extended sodic alteration in the southwestern part of the island may correspond to a deeper exposed level, and the sulfide stockwork mineralization in the central part of the island might belong to a shallower exposed level of the system (Fig. 2).

Even though a lot of studies considering the Serifos fresh granodiorite petrography and geochemistry have been conducted during the last decades (Salemink, 1985; Ducoux et al., 2017; Stouraiti et al., 2017) our knowledge about the ore mineralogy of the quartz veins and breccias hosted in the granodiorite remains incomplete. Since a sheeted vein system and a sulfide stockwork-type mineralization were found within the granodiorite, this study examines new ore mineral occurrences, including those within the sheeted veins and those of disseminated and sulfide stockwork types, in five different areas inside the granodiorite. Major aim of the study is to correlate these new ore mineral occurrences with the skarn-hosted mineralization located in the southwestern part of Serifos and to provide some information about the whole hydrothermal system creating these deposits.

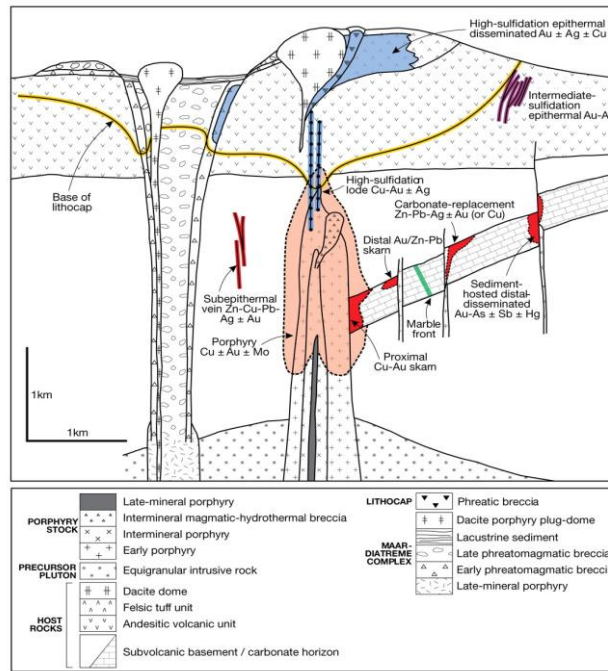


Fig. 1: Scheme modified from Sillitoe (2010), showing the connection between a magmatic source, in our case the granodiorite, the skarn deposits along the granodiorite-host rock contact and the manto-type massive mineralization in the carbonate-replacement deposits.

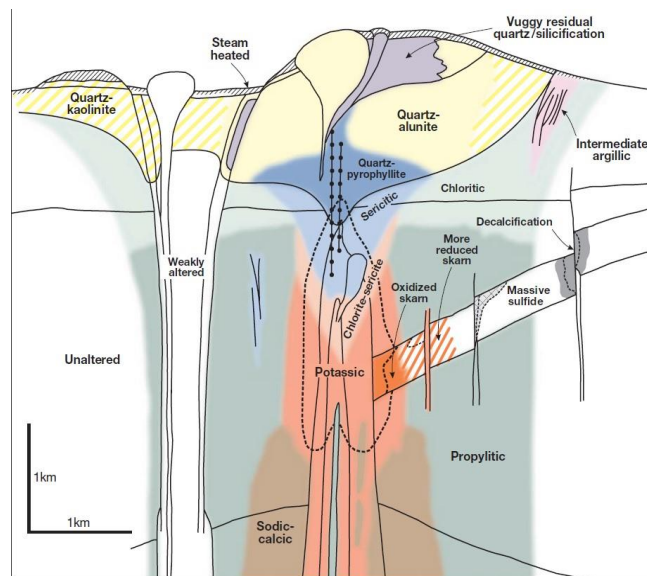


Fig. 2: Scheme from Sillitoe (2010), showing the alteration zones in a porphyry-centered system. Note that the sodic-calcic alteration zone belongs to the deeper part of the system, where the potassic zone along with the quartz stockwork veins belongs to the shallower part.

Moreover, we provide new geochemical, mineralogical and microthermometric data from a molybdenite-bearing igneous body in the southeastern part of the island, here called aplogranite, first described by Voudouris et al. (2010) as ‘leucogranite’. The main question concerning the aplogranite is how it is related to the granodiorite and consequently the skarn mineralization. Is it part of the system described above, or it is

a different system? Due to the geochemical signature and petrographic characteristics of the aplogranite, along with the results coming from microthermometry of fluid inclusions, the second scenario is proposed suggesting a different system than the granodiorite-related skarn. In fact, the aplogranite shares some features with other S-type, ilmenite-series igneous rocks around the world, which in some cases relate to the so-called intrusion-related systems (Lang et al 2000, Baker et al 2005). Further analysis would be necessary for our better understanding of such systems, which play a critical role in generating Mo, W and Sn deposits (Fig. 3).

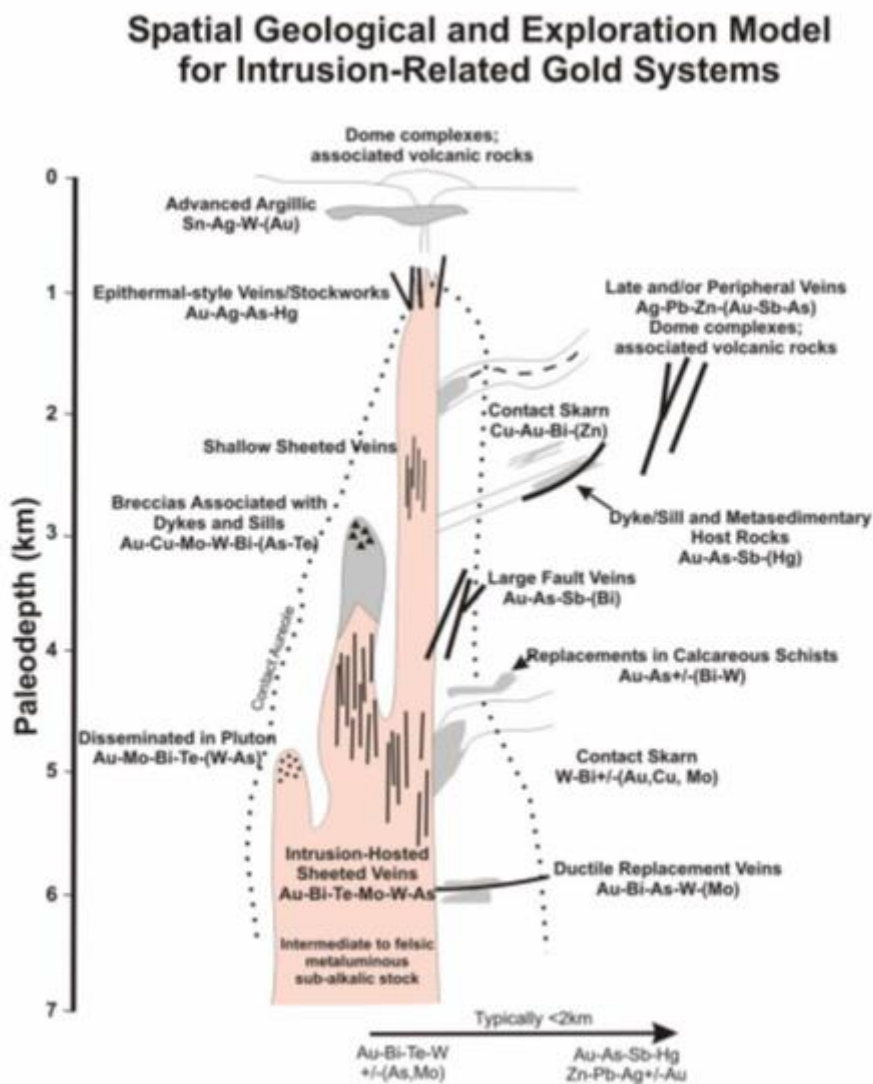


Fig. 3: Scheme showing an exploration model for intrusion-related gold systems (after Lang and Baker 2001)

II. Analytical methods

For the needs of this study, 36 thin polished sections and 27 polished blocks, for the study of the metallic minerals, were prepared and studied with an optical microscope in both transmitted and reflected light at the University of Athens, Greece. These thin sections were studied by a JEOL JSM 5600 scanning electron microscope, equipped with back-scattered imaging capabilities, at the Department of Mineralogy and Petrology, University of Athens.

Raman Spectroscopy analysis was conducted for the identification of some undefined minerals in both thin sections and polished blocks. It is a quick and easy method, appropriate for the qualitative identification of minerals which cannot be identified via the usual optical petrography. Furthermore, it is a non-destructive analysis widely used for the determination of the vapor or solid phases trapped inside fluid inclusions and for this reason it is preferred from the destructive LA-ICP-MS method. The analysis was conducted at the University of Geneva with the use of a green laser (532nm). The analyzed minerals come from the sheeted veins in Koutalas, from the aplogranite in the Sotiras and the Kefala areas and from the sulfide stockwork mineralization in the Heliport area.

Silicate minerals from both the outer part of the granodiorite and the aplogranite were analyzed with a JEOL 8200 superprobe Electron Probe Micro-Analyzer (EPMA) equipped with secondary electron and back-scattered electron detectors at the University of Geneva, Switzerland.

CL images were taken via optical cathodoluminescence technique (CITL CL 8200-MK 5-1) at the University of Geneva, Switzerland.

Finally, 6 double polished sections were prepared for fluid inclusion microthermometry at the University of Geneva. For this technique, a Linkam THMSG 600 stage mounted on a Leica DMLB microscope with 100x objective was used.

III. Geological setting

Serifos is located about 100 km SSE of Athens in the Aegean Sea, Greece. It belongs to the Attic-Cycladic Unit, which is part of the Hellenides-Taurides belt (Figs 4 and 5). This belt, along with the Alps, Dinarides, Apennines, Carpathians and Betic, has formed during the Late Cretaceous- Eocene period, as a result from the African-Eurasia convergence. By the end of Eocene (~35 Ma), slab retreat has caused the formation of several back-arc basins including the Alboran Sea, the Ligurian-Provencal Basin, the Tyrrhenian Sea, the Pannonian Basin and the Aegean Sea. The Aegean Sea belongs to the central part of the Hellenides-Taurides belt and has formed in a back-arc basin environment (Stampfli, 2000).

The Hellenides are subdivided into two regions. The External Hellenides appear in the western part only deformed and metamorphosed during the Oligocene-Early Miocene with the subduction of the Apulia microcontinent beneath the Eurasian plate with the disappearance of the Pindos Ocean (Jolivet and Brun 2010, Jolivet et al 2013). The Internal Hellenides appear in the eastern part and present a much more complex history. The Internal Hellenides, have been deformed and metamorphosed once in the Late Jurassic-Early Cretaceous with the subduction of the Pelagonian microcontinent beneath the Eurasian plate with the disappearance of the Vardar Ocean. The second deformation and metamorphic event occurred in the Oligocene-Early Miocene which was the main orogenic episode in the External Hellenides (Papanikolaou, 1986).

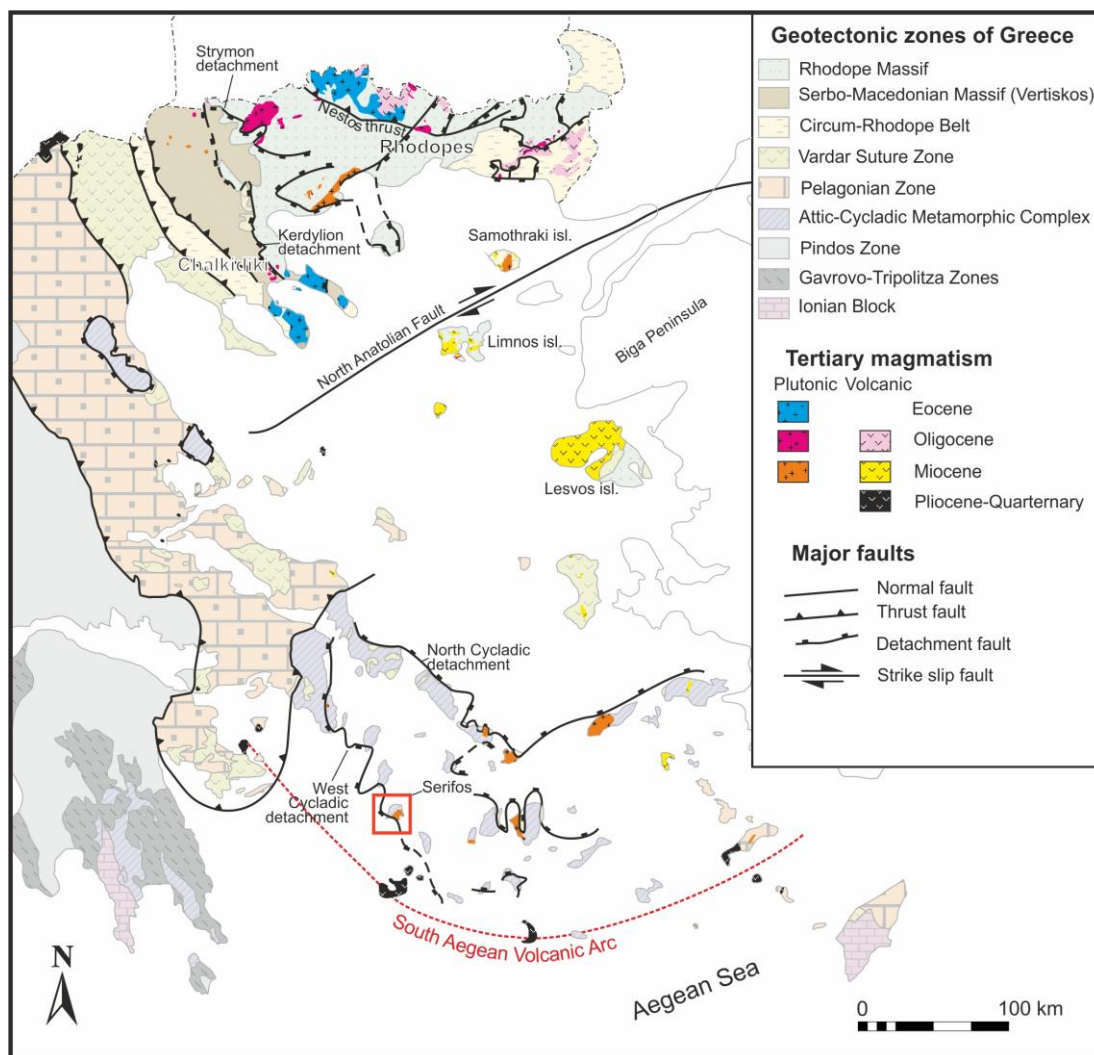


Fig. 4: Map showing the geotectonic zones of Greece (modified from Melfos and Voudouris, 2017 and Voudouris et al., 2019). Serifos island belongs to the Attico-Cycladic Massif (area inside the red square)

The island of Serifos is actually part of the Attico-Cycladic massif. Herein, the rocks have been affected by the subduction of the Pindos Ocean beneath the Eurasian plate,

as it is previously mentioned (Bonneau and Kienast, 1982; Bonneau et al., 1984). Specifically, a pre-Alpine continental basement, mainly consisting of paragneiss and orthogneiss is underlain by a thick pelagic limestone unit with metapelites and metabasites intercalations which is metamorphosed under HP/MT blueschist phase conditions ($P=8-14$ kbar; $T=350-550^{\circ}\text{C}$) during the Eocene. Those blueschists typically appear in the islands of Syros, Tinos and Andros. On Serifos (Fig. 5), those blueschists have been affected by the later LP/MT greenschist phase ($P=3-11$ kbar, $T=300-520^{\circ}\text{C}$) during the Late Oligocene-Early Miocene (Salemink, 1985; Stouraiti et al., 2017).

Three tectono-metamorphic units have been recognized on the Cycladic islands within the Aegean domain (Bonneau, 1984): i) the Cycladic Continental Basement (CCB); ii) the Cycladic Blueschist Unit (CBU), and iii) the Upper Cycladic Unit (UCU; Bonneau et al., 1984; Grasemann et al., 2012; Ducoux et al., 2017).

The CCB crops out in the central and southern Cyclades and especially on Ios, Paros, Naxos, along with Serifos and Sikinos. This unit comprises granite, paragneiss and orthogneiss showing a complex pre-Alpine history. On Serifos, it appears in the southern part of the island usually as gneisses with metabasite intercalations and dolomite-calcite marble mylonites (Fig. 5). Metapelites and marbles of this units have been correlated with the Gavrovo-Tripolis paleogeographic domain, while some researchers believe that this unit extends to the Menderes Massif in Western Anatolia.

The CBU crops out on most of the Cyclades islands and is composed by a sequence of metapelites, metabasites and marbles. The rocks of this unit have reached upper metamorphic conditions up to temperature of 580°C and pressure of 20 kbar in some islands (Syros, Tinos, and Naxos), conditions responsible for the formation of blueschists and even eclogites in these parts of the Cyclades region. This episode is associated with the Eocene subduction of Pindos ocean below the southern margin of Eurasia between 70 and 35 Ma. On Serifos however, these HP/HT signatures have been overprinted by LP/HT greenschist metamorphism, related to post-thickening crustal thinning during the Oligo-Miocene slab retreat episode between 30 and 18 Ma. This episode was followed by a partial melting phase, dated between 21 and 17 Ma, causing migmatite formation on Naxos and Ikaria. The CBU occupies the whole northern and a small portion of the southwestern part of the island and it consists of the following formations (bottom to top) : a) amphibolites with gneiss intercalations; b) switched greenschist and marble layers, and c) ultramylonitic marbles.

The UCU consists of an ophiolitic material partly metamorphosed during the Late Cretaceous. On Serifos, it occurs only in the southwestern part of the island, in the Kavos Kyklopas area and it consists of ankeritized schists and metaophiolites (Fig. 5).

The CCB and the overlaying CBU have a contact along a low-angle detachment fault in the area of Meghalo Livadhi (MLD; Ducoux et al., 2017), while the contact between CBU and UPU crops out in the Kavos Kyklopas in the southwest and Platy Gialos peninsulas to the northeast (Fig. 5). These two detachment systems are believed to have played a crucial role to the circulation of the hydrothermal fluids responsible for the formation of the skarn deposits in the southwestern part of the island, showing a system similar to the carbonate-replacement deposit at Lavrion.

About the 1/3 part of the Serifos island is occupied by a granodioritic igneous body (Fig. 5). This intrusive body results from the southward arc migration during the end of the Miocene period (~10Ma), causing a syn-tectonic re-melting of the crust and consequently the formation of the I-type granites or granodiorites in Tinos, Delos, Mykonos, Ikaria, Naxos and Serifos (Papanikolaou et al 1985, Jolivet 2013).

The granodiorite of Serifos, was emplaced at 11,6 to 9,5 Ma, penetrating the rocks of the CCB and CBU, causing contact metamorphism in the host marbles and schists and consequently development of a calcic exo- and endo-skarns as long as carbonate-replacement ores and retrograde low-temperature veins (Marinos, 1951; Salemink, 1985; Iglseder et al., 2009; Stouraiti et al., 2017).

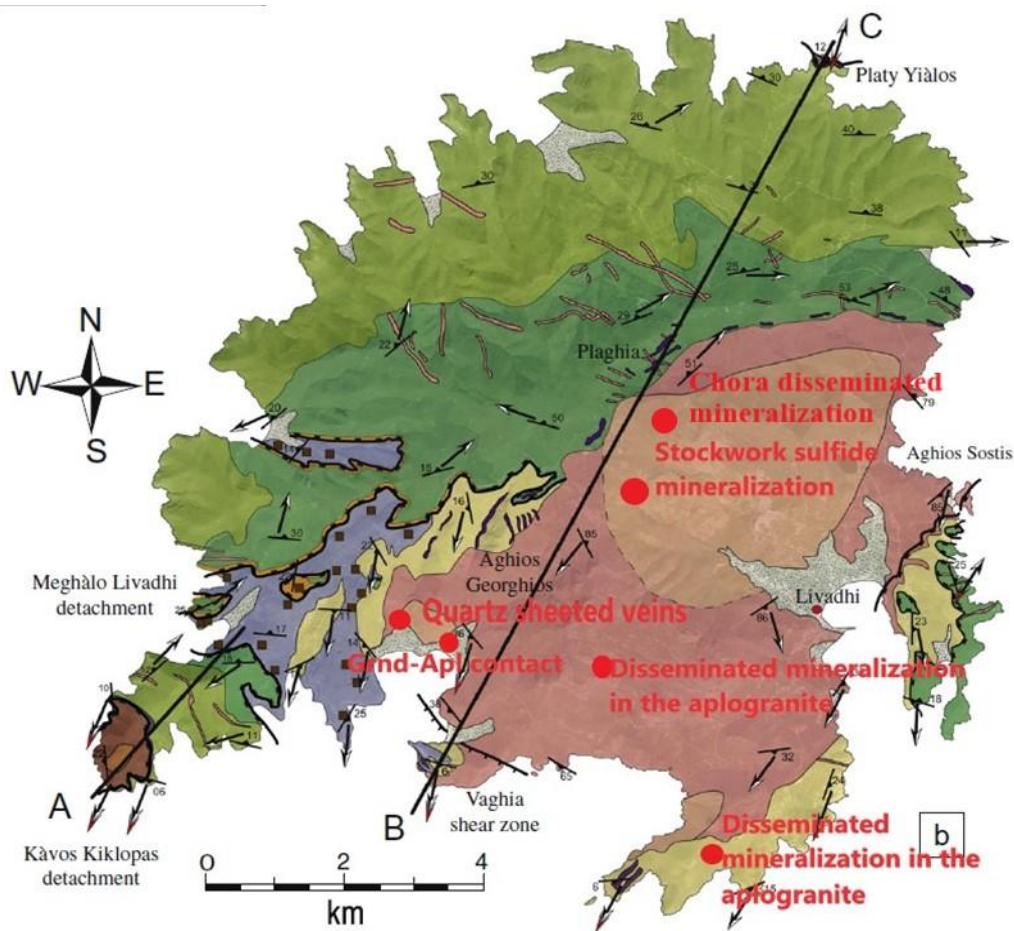
The pluton is an I-type hornblende-biotite granodiorite, showing different characteristics from core to margins. The core of the pluton shows a non-foliated, fine-grained, equigranular texture and a tonalitic composition, while the outer facies shows a more foliated texture and a hornblende-biotite-allanite mineral assemblage (Stouraiti and Mitropoulos 1999; Grasmann and Petrakakis 2007; Seymour et al., 2009). The crystallization temperature and emplacement pressure have been estimated to 700-750 °C and 1,5 to 3,5 kbar respectively (Seymour et al., 2009). A number of aplitic, pegmatitic and dacitic dikes intruded various lithologies of the CBU units. Their ages range from 8,2 to 8,7 Ma, while their P-T conditions are considered to be 1-2 kbar and <650°C respectively. The intrusion was emplaced at shallow depths, near the ductile-brittle transition boundary, while according to Salemink (1985) the lithostatic pressure at the time of the intrusion was estimated at 1-1,5 kbar. Salemink (1985) estimated crystallization pressure of amphiboles: 2,5-3,7 kbar in the core of the crystals and 0,33-1,5 kbar in the margins, suggesting that the intrusion moved upwards from a 12km depth to a 3km depth during emplacement.

Iglseder et al. (2009) also reported on the occurrence of an older S-type granitic body cropping out along the margins of the larger granodiorite intrusion, and which was mylonitized by an earlier phase of deformation at temperature of approximately 450°C. Based on Rb-Sr dating of muscovite, whole rock ages for these orthogneiss mylonites are calculated between 15.0 ± 0.2 and 11.3 ± 0.1 Ma (Iglseder et al., 2009), which either indicate a lower intrusion age of the protolith, or a thermal resetting due to the emplacement of the granodiorite.

IV. Local geology and field work

This study focuses on the description of five mineralized areas within the Serifos pluton. In this chapter, the local geology and the petrological characteristics of these areas are described and a detailed map showing these five areas, is given at the end of this chapter. The geologic map is from Ducoux et al. (2017) and is modified indicating the location of the sampling sites (Fig. 5). Four of them are located inside the granodiorite. The fifth one, bearing disseminated mineralization, is located in the Sotiras area in the southeastern part of the island, and is hosted within a different igneous body, hereafter referred to as aplogranite, and previously described as

leucogranite by Voudouris et al. (2010). The petrography, ore mineralogy along with the geochemistry of this body will be discussed in the following chapters.



Lithologies		
Ore deposits	Quaternary	Cycladic Continental Basement
<ul style="list-style-type: none"> Ca-Fe HT-skarns Ca-Fe-Mg MT-skarns Fe-Ba LT ore deposits 	<ul style="list-style-type: none"> Alluvial sediments 	<ul style="list-style-type: none"> Dolomite-calcite marble mylonites Gneisses with metabasite intercalations
Intrusive rocks	Upper Cycladic Unit	Main structures
<ul style="list-style-type: none"> Granodiorite (inner facies) Granodiorite (border facies) Dykes et sills 	<ul style="list-style-type: none"> Metaophiolites Ankeritized schists 	<ul style="list-style-type: none"> Detachment Extensional shear zone Field foliation Field lineation Field lineation with sense of shear
	Cycladic Blueschists Unit	
	<ul style="list-style-type: none"> Ultramylonitic marbles Greenschist, marble layers Amphibolites with gneiss intercalations 	

Fig. 5: Geologic map of Serifos, after Ducoux et al. (2017), demonstrating the four mineralized locations, the area dominated by the aplogranite, as well as the granodiorite-aplogranite contact in the Koutalas area, described in this thesis.

Chora prospect

In the Chora area, the texture appears to be non-foliated, equigranular and fine-grained. In this part of the granodiorite, the tectonic activity and contemporaneous fluid circulation have been responsible for the creation of a system of fissures and veinlets with random orientation. Since we are located in the inner facies of the pluton, no contacts between the granodiorite and the rocks of the CCB or the CBU were established. There are no quartz veins and veinlets, even though a great variety of veinlets comprised of actinolite, titanite, chlorite and calcite along with bleached zones (Fig. 6a,b) with chlorite-calcite alteration halo occur. These veinlets have a total thickness of 0,05-2,5 cm and an alteration halo thickness of 0,3-1 cm for the majority of the veinlets with a maximum thickness of 3 cm in a few bigger veins. A few disseminated ore minerals appear along the granodiorite mainly pyrite and more rarely chalcopyrite (Fig. 6c). Goethite pseudomorphs after magnetite and pyrite along with magnetite veins are present (Fig. 6d). Malachite and azurite have formed due to supergene oxidation of chalcopyrite.

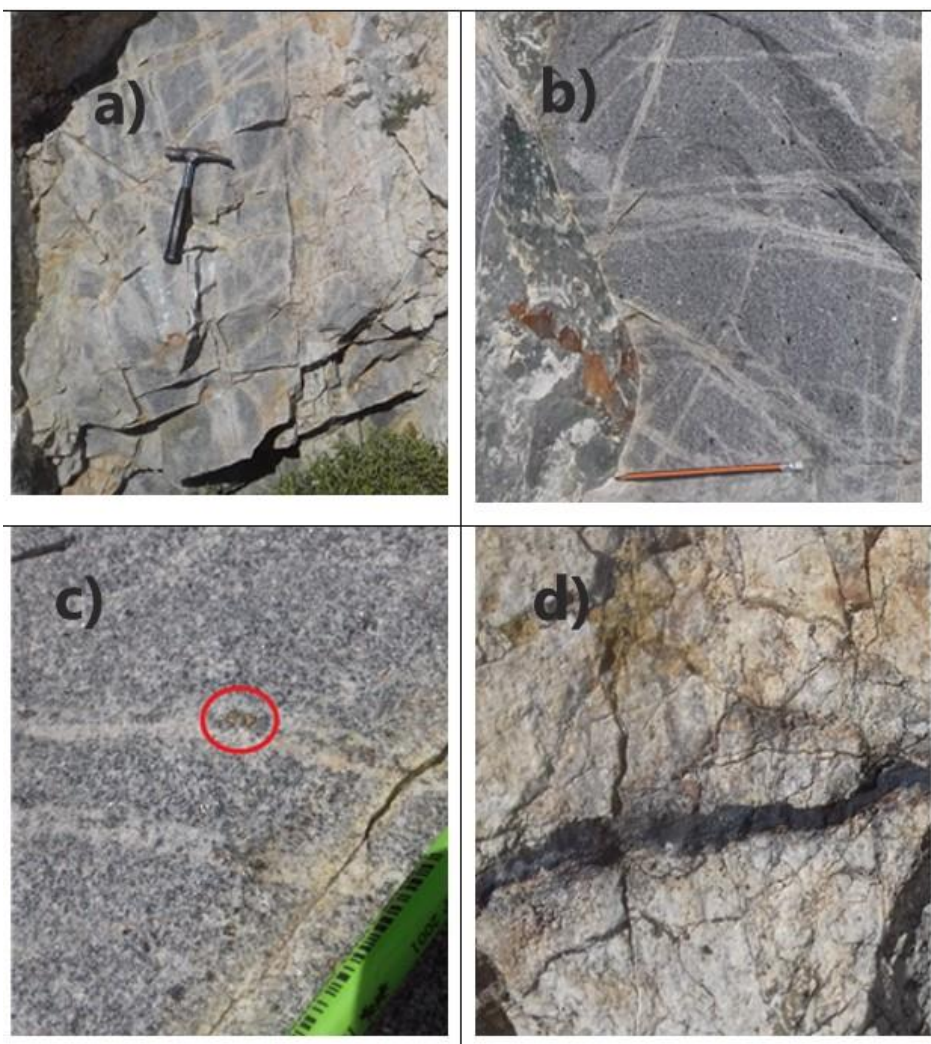


Fig. 6: Photographs of the inner part of the granodiorite located in Chora: (a,b) Bleached zones with chlorite-calcite alteration halo; (c) Disseminated chalcopyrite crystal within the granodiorite; (d) Goethite after magnetite and pyrite vein within the granodiorite

Koutalas- Ganema prospect

In the area of the Koutalas Bay, the granodiorite is in contact with the gneisses of the CCB unit. The granodiorite presents a more foliated and porphyroblastic texture with large biotite phenocrysts while locally mafic xenoliths inside the pluton show a complex magmatic history, probably including crustal contamination and host rocks assimilation. In contrast to the Chora location, the Koutalas area is characterized by the presence of hydrothermal quartz veins containing quartz, orthoclase, albite, titanite and adularia along with veinlets with various amounts of actinolite, hornblende, titanite, chlorite and calcite (Fig. 7). The veins are 0,05-0,4 cm thick and they all display alteration halos their thickness range from 0,25 to 3,6 cm. A lot of bleached zones (Fig. 7a,b) have been formed from hydrothermal fluids circulation along the fissures and veinlets inside the granodiorite.

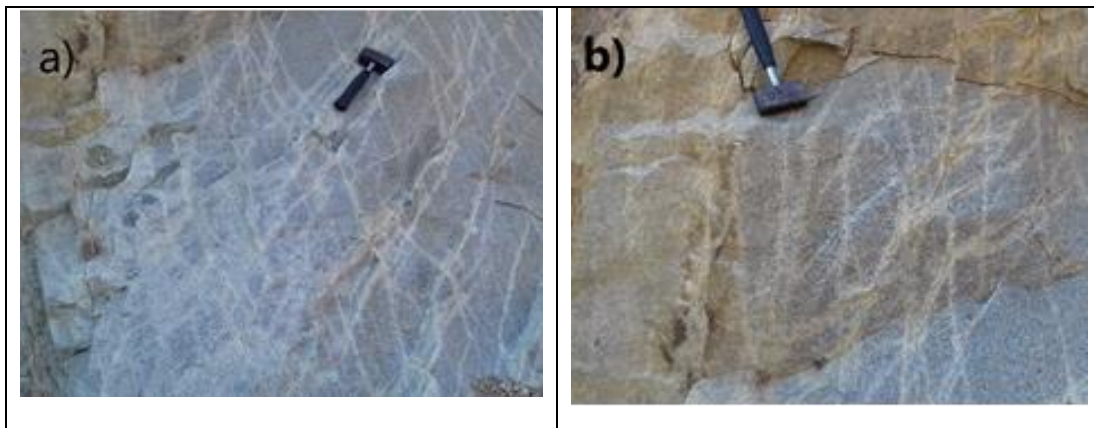


Fig.7: Photographs from the outer part of the granodiorite body in the Koutalas area: (a,b) Bleached zones with chlorite-calcite alteration halos similar to those from the inner part at Chora. The brown areas correspond to supergene alteration.

To sum up, three main generations of veins can be distinguished in both the Chora and the Koutalas areas (Fig. 8). The first generation corresponds to the early stage veins and consists of quartz, albite and orthoclase and is found only in the outer part of the granodiorite. The second generation, e.g. the intermediate stage veins, is composed mainly of actinolite, titanite and hornblende with minor amounts of quartz and chlorite. The third and final stage is subdivided into two substages with chlorite-calcite-adularia in the first substage (V3a), and calcite-adularia in the second substage (V3b).

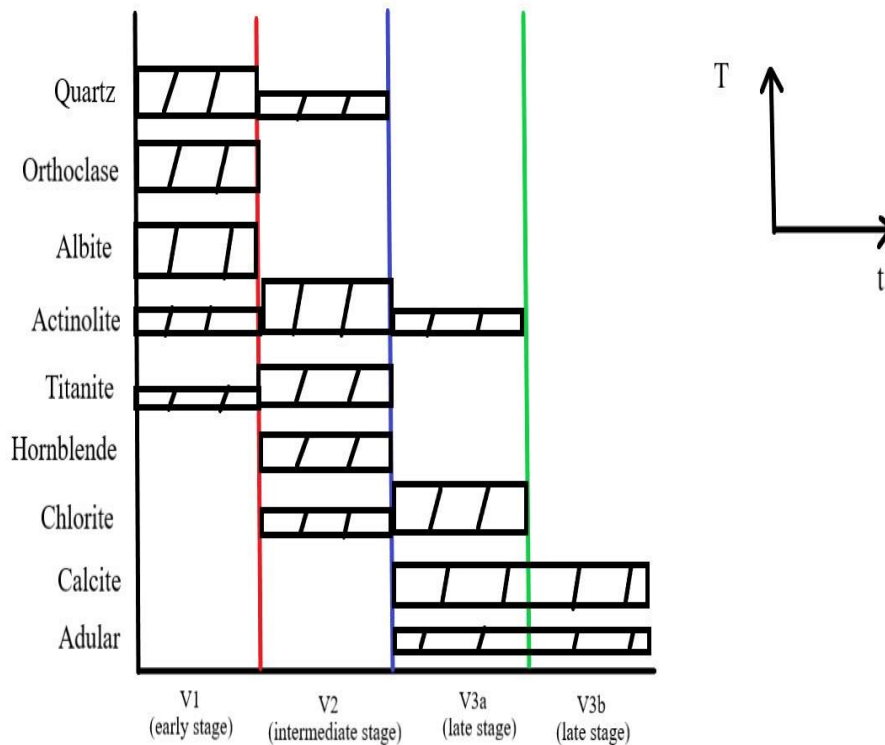


Fig.8: Diagram showing the mineral composition of the veins within the granodiorite in the Chora and Koutalas areas. Early stage veins including hydrothermal quartz were formed at higher temperature, while in the lower temperatures ones chlorite and calcite are present.

The second mineralized area is located in the Koutalas Bay along the road and about 200 m north of the Agia Theodora church. It comprises a system of at least 15 quartz sheeted veins, along a 8,5 m long profile striking N-S (Fig. 9). For simplicity, we have numbered the veins from the southern edge to the northern, as vein 1 to 15, respectively. Most of the veins have an almost E-W strike and a dip about 10°N. The only exceptions are vein number 7, having a dip of 70°N and vein number 9, having a dip of 10°N, while the strike remains stable. The veins thickness along with the distance between them range from 1 to 9 cm and 0,3-1,5 m, respectively. We have collected samples from veins Nr 2, 6, 7, 9, 10, 11, 12 and 15. From the collected samples, veins # 7, 9 and 15 contain ore minerals mainly pyrite (Fig. 10a), with smaller proportions of chalcopyrite. In vein #15, oxidation of chalcopyrite has caused the formation of supergene minerals like azurite and malachite, while in vein #11 the pyrite seems to be completely oxidized to Fe oxides. Chlorite appears in vein #6, mainly as a breccia cement. Lastly, in vein #10 a core-to-margins zonation has been observed: equigranular quartz towards an aplitic margin and finally, a granodiorite host. Hydrothermal quartz veins without ore minerals are also common in this area (Fig. 10b).



Fig. 9: Sheeted vein system in the Koutalas Bay



Fig. 10: Textural aspects of the vein system in the Koutalas Bay area: a) Vein #9 consists mainly of quartz and pyrite, while chalcopyrite occurs in smaller proportions. Granodiorite is the host rock; b) Barren hydrothermal quartz vein.

At about 150 m higher and 250 m to the north from the sheeted quartz vein system, the contact between granodiorite and marbles is exposed. The marbles are characterized by skarn- and carbonate-replacement style of mineralization. This suggests that the quartz vein system may represent the feeder zone to the overlying skarn mineralization, with a possible genetic relationship between them. In this topographically higher position, up to 1-2cm-thick quartz veins and veinlets, bearing mostly oxidized ore minerals are hosted within the granodiorite and showing potassic alteration halos.

In the Ganema area and about 1 km to the East from the previous location, a tight network of barite veins with a $N70^{\circ}W$ and a $40^{\circ}SW$ dip appears along a major fault structure cross-cutting the granodiorite. This network belongs probably to the low-

temperature hematite-limonite-barite-fluorite vein described by Salemnik (1985). Near the barite vein network, a randomly orientated network of quartz stockwork appears.

In the Ganema area, the aplogranite intrudes the granodiorite with intense presence of secondary hydrothermal actinolite (Fig. 11a,b) upon the contact between the two igneous bodies (Fig. 12). Barite and Fe-oxides are also present within N70°W-trending veins crosscutting the aplogranite. This vein system is parallel to the one located 400m to the north inside the granodiorite, as previously described. Barite is related to the latest stage of mineralization with the synchronous deposition of fluorite and carbonate minerals.

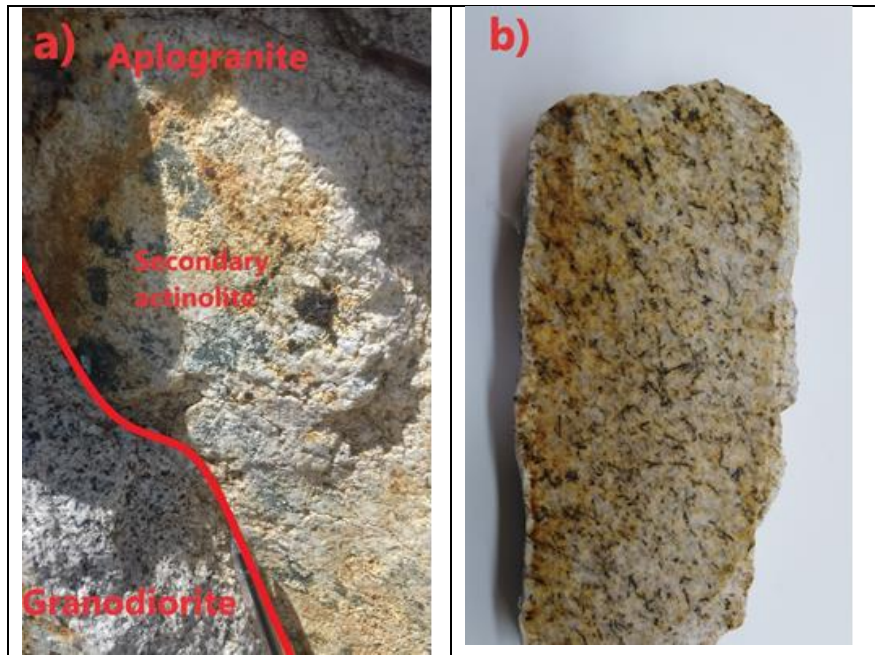


Fig.11: a) Assemblages of secondary amphibole in the contact between the aplogranite and the granodiorite in the Ganema area (pen used as scale); b) Hand specimen (10 cm wide) from the contact between these two rocks. Secondary long-shaped amphibole crystals can be seen.



Fig.12: White-colored veins of aplogranite intrude the grey-colored granodiorite in the Ganema area

Sotiras prospect

The third mineralized site is located in the area of Sotiras in the southeastern part of the island. The area is dominated by gneisses of the CCB unit (Fig. 13) and a white-colored igneous rock, previously named ‘leucogranite’ by Voudouris et al. (2010). For simplicity, this rock is called aplogranite in this study, based on the macroscopic similarity between it and the aplitic dykes found within the granodiorite. The aplogranite texture is more coarse-grained than the one of the granodiorite and it comprises mostly quartz and K-feldspar, with subordinate biotite. Furthermore, the aplogranite is crosscut by wide (>10 cm) hydrothermal coarse-grained quartz veins (Fig. 14a, b). The area is also characterized by pyrite dissemination, while molybdenite is also present as submicroscopic crystals along with pyrite (Voudouris et al., 2010).



Fig.13: Intrusive contact between aplogranite and gneisses from the CCB in the Sotiras area (hammer as a scale).

Two different scenarios are proposed in this study to explain the appearance of this igneous body in the island of Serifos. The first scenario implies the existence of one magmatic source, of granodioritic composition. Further fractionation of the granodioritic magma could be a possible explanation for the crystallization of the white-colored aplogranite. The second scenario implies the presence of two different magmatic sources, for the formation of each igneous body, with successive intrusion of the aplogranitic melt into the solidified granodiorite. Mineralogical evidence (see below), rather supports the second scenario.

The quartz veins crosscutting the aplogranite are related to a sericitic alteration (sericitization of K-feldspar), while locally secondary coarse-grained muscovite (e.g. greisen alteration, see Seedorf et al. 2005) also appears. Mirolitic cavities are also present in the aplogranite of the Sotiras area and show a disseminated-style mineralization consisting mainly of pyrite (Fig. 15). The environment is similar to the

one of the reduced intrusion-related deposits, hosted in subalkalic, metaluminous intrusions of intermediate to felsic composition, hosting W and Sn deposits (Lang et al. 2000; Baker et al. 2005). These deposits are related to reduced magmas, belonging to ilmenite rather than magnetite series, with high Rb/Sr values (>1) and low $\text{Fe}_2\text{O}_3/\text{Feo}$ values (<1). Greisen-type alteration with the presence of hydrothermal muscovite along with tourmaline, fluorite and barite is usual in such systems. Although no fluorite, barite or tourmaline were found in the Sotiras area and the presence of secondary muscovite is quite restricted, the presence of disseminated-style mineralization associated with the miarolitic cavities is another feature which indicates for a until poorly described intrusion-related system in the island of Serifos. Miarolitic cavities are believed to have formed by the circulation of high temperature supercritical fluids (e.g. Lang et al. 2000; Baker et al. 2005).

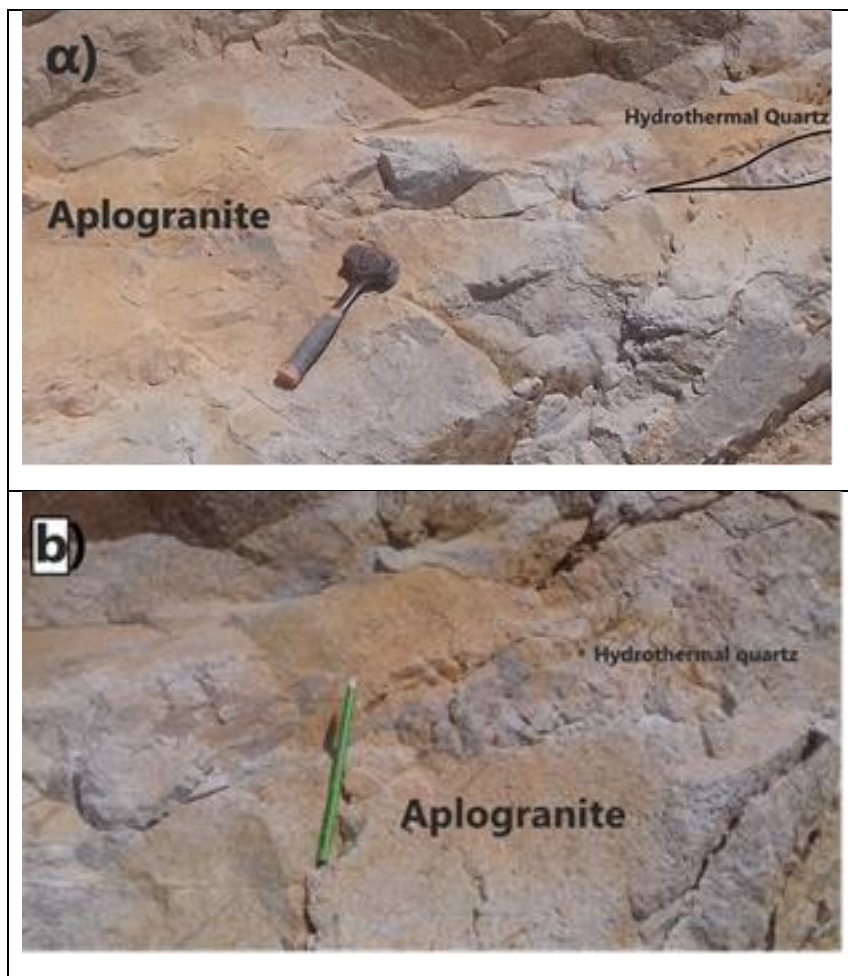


Fig.14: a,b: Large coarse-grained quartz veins, cross-cut the aplogranite in the Sotiras area.

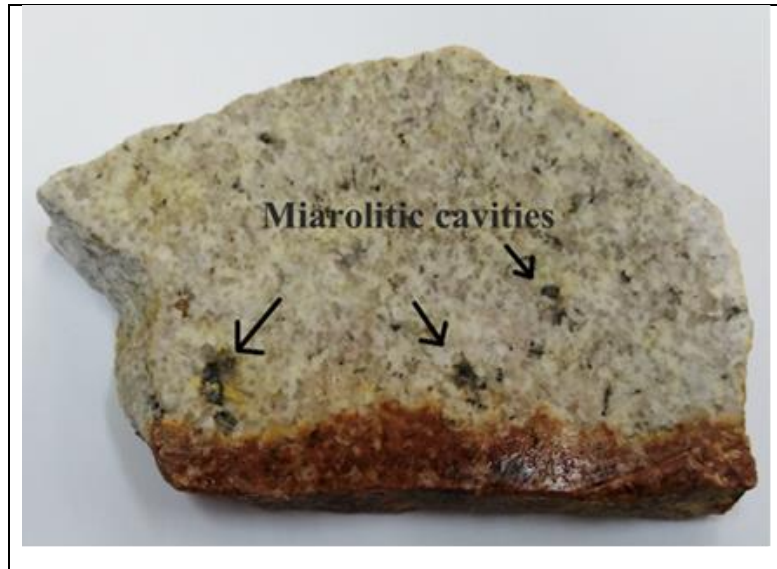


Fig. 15: Miarolitic cavities within the aplongranite from the Sotiras area. These cavities are related to a disseminated pyrite mineralization.

Kefala Hill prospect

The fourth mineralized site is located at an altitude of 422 m, on the top of the Kefala Hill in the central part of the island. Therein, another outcrop of aplongranite (similar to the previous one from the Sotiras area) has intruded in the rocks of the CCB unit. The Kefala Hill aplongranite is weakly potassically altered with secondary biotite and actinolite formation and partly sericitized. Disseminated pyrite mineralization, mostly oxidized is also observed in this prospect.

Nearby, the granodiorite appears strongly mylonitized, with a cataclastic to mylonitic texture related to the presence of a nearby N60°W trending fault. Both the granodiorite and the aplongranite contain disseminated pyrite mineralization.

Helipoint prospect

Lastly, the fifth site is located about 2km south of the heliport. This area is dominated by a brecciated granodiorite, where an impressive network of sulfide minerals, mainly pyrite chalcopyrite along with pyrrhotite occurs as breccia cement inside the granodiorite (Fig. 16a, b). The whole system gives the impression of a sulfide stockwork type mineralization, with the granodiorite clasts affected by sericitic alteration. Sulfide veinlets cross-cut quartz sheeted veins with strike N80°W.

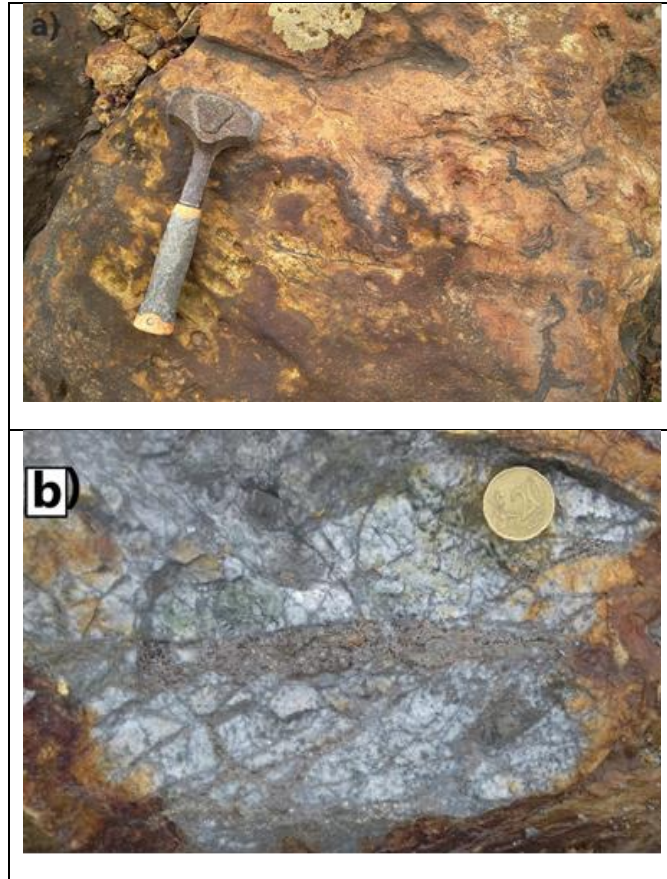


Fig.16: a,b) Sulfide stockwork and breccia style mineralization from the Heliport area.

V. Results

V.1.Petrography and hydrothermal alteration

It is described by previous studies (Salemnik 1985; Ducoux et al., 2017; Stouraiti et al., 2017) that the granodiorite is distinguished in the inner/central facies and in the outer/border facies of the intrusion. During the field campaign, samples were collected from both the two different facies, from the Chora and Koutalas areas, respectively. Moreover, samples were taken from the southeastern part of the island where the aplogranite is the dominant phase. A table of the mineralogical composition of these three different rock types plus the mafic enclaves (data from Stouraiti et al., 2017) which are dispersed along the granodiorite, is given below and the data are plotted in Figure 17.

Table 1: Mineral composition of igneous rocks from Serifos island. Zircon, rutile and pyrite occur as accessory minerals and therefore they are not shown in this table

	Quartz	K-feldspar	Plagioclase	Biotite	Hornblende	Titanite	Apatite
Inner granodiorite	12-19 %	10-15%	34-47%	15-16%	5-10%	2-5%	<5%
Outer granodiorite	20-26%	14-19%	37-43%	9-15%	3-6%	2-5%	5%
Mafic enclaves	6%	8%	44%	6,50%	35%	<5%	<2%
Aplogranite (this study)	25-30%	32-43%	15-27%	<5%	<2%	<2%	2-5%

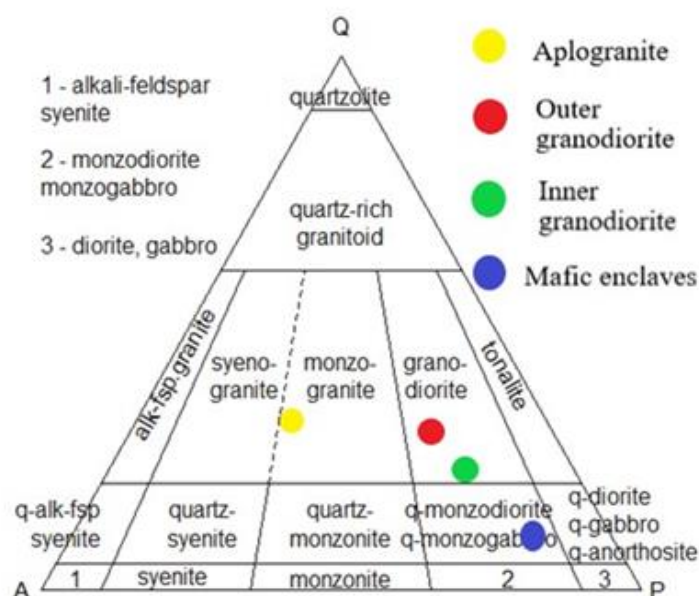


Fig.17: Composition of the four igneous rock types in Serifos island projected on a QAPF diagram (Streckeisen, 1974) . Within the granodiorite, a progressive fractionation may have been the cause for the formation of the outer granodiorite from a more mafic primitive magma (its composition corresponds to the mafic enclaves). Another scenario proposed is the crystallization of the external facies of the granodiorite, then followed by the crystallization of the internal facies by a different chamber recharge event from a more primitive, less evolved source feeding the central part of the magma chamber. The aplogranite presents a more felsic monzogranite-syenogranite composition either from a further fractionation of the granodiorite or corresponding to a completely different magma from a different source.

The inner facies is composed mainly of quartz (12-19 %), plagioclase (34-47 %), K-feldspar (10-15 %), biotite (15-16 %) and hornblende (5-10 %), while titanite, apatite, zircon, rutile, and pyrite occur as accessory minerals. The plagioclase crystals are zoned with a more calcium-rich (labradorite) core surrounded by a sodium-rich (oligoclase) rim (Fig. 18c) and are partly replaced by secondary sericite, chlorite and calcite (Fig. 18e). Most of the K-feldspar crystals remain fresh and appear subhedral and equigranular with characteristic perthitic texture in the K-feldspar.

Two different generations of biotite have been observed. The first generation contains large phenocrysts (0,5-1cm) of primary magmatic biotite (Fig. 18a), partly or in a few

cases completely replaced by secondary amphibole, biotite and chlorite, while in the least altered crystals, apatite inclusions along with needle-shaped rutile crystals can be observed. The primary biotite may present tectonic features like kink bands or kink lamellae (Fig. 18d). The second biotite generation contains aggregates of secondary hydrothermal biotite crystals 0,1-0,5 mm (Fig. 18f). Hornblende phenocrysts (Fig. 18b), 0,5-2,5 mm, appear mostly fresh, while in some cases they are partly replaced by secondary amphibole (actinolite), and biotite (Fig. 18f, g). Titanite crystals, 0,1-0,4 mm, occur mostly fresh, in a few cases along with smaller hornblende and biotite crystals in veinlets within the granodiorite (Fig. 18j).

Secondary chlorite and calcite (Fig. 18h) occur as veins cross-cutting the previously mentioned hornblende-biotite-titanite veins or replacing primary silicate minerals such as plagioclase and biotite. The chlorite±calcite veins are located along fractures within the granodiorite, are 0,2-0,3 mm wide and appear with three different types a) chlorite veins b) calcite veins and c) veins with calcite centerline and chlorite margin.

No significant amounts of ore minerals were found in the central part of the granodiorite, except from a few disseminated pyrite and chalcopyrite crystals in the Chora area. Due to oxidation of chalcopyrite, supergene malachite and azurite formed in near-surface conditions

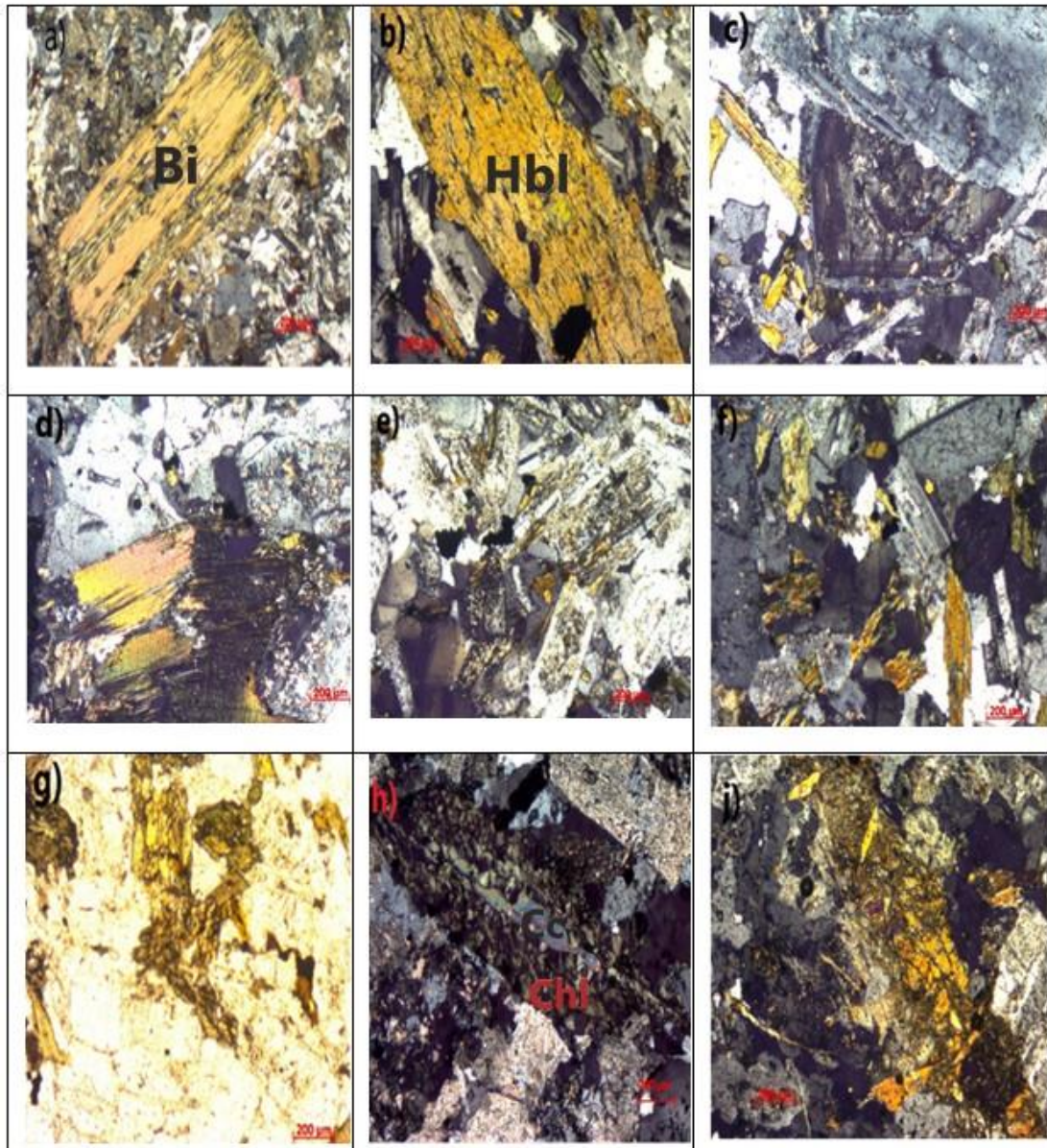


Fig. 18: Microphotographs of the inner (central) granodiorite in the Chora area: a) Primary biotite crystal partly replaced by chlorite; b) Primary hornblende crystal with biotite inclusion c) Primary plagioclase with characteristic oscillatory zoning; d) Kink banded biotite; e) Secondary amphibole and sericite partly replacing the plagioclase anorthite-rich core; f) Assemblage of secondary biotite crystals; g) Assemblage of secondary biotite and amphibole crystals; h) Calcite-chlorite veinlet with calcite centerline; j) Secondary veinlet consisting of amphibole and titanite within the inner part of the granodiorite. (Bi=biotite, Hbl= hornblende, Cc= calcite and Chl= chlorite)

During this study, both the outer facies of the granodiorite at Koutalas-Ganema and the aplogranite located in the southeastern part of the island were examined. As it is mentioned above, the granodiorite has a more felsic composition from the core to the margin and consists mainly of quartz (20-26 %), plagioclase (37-43 %), K-feldspar (14-

19 %), biotite (9-15 %), hornblende (3-6 %), while apatite, zircon, rutile, titanite as long as opaque minerals occur as accessory minerals (Table 1; Fig. 17).

The most interesting feature about this outer part of the granodiorite, is the intense sodic alteration that has taken place in the area. Specifically, most of the K-feldspar has been replaced by secondary albite, while the same process has taken place in the plagioclase, with secondary albite replacing the more An-rich core. This alteration is related to the veins of hydrothermal quartz, which occur all over the outer granodiorite area. Significant amount of hydrothermal shreddy biotite was found too. The secondary biotite (Fig. 19a, f, h) are 0,2-0,5 mm large, occur mostly as assemblages and they replace primary biotite or hornblende phenocrysts. The primary biotite (Fig. 19b) shows similar features with those found in the inner facies like kink bands and kink lamellae. Primary hornblende and titanite (Fig. 19c and d, respectively) preserve their original texture. Secondary actinolite has partly replaced plagioclase in some cases (Fig. 19g).

Summarizing, it is obvious, that there is a widely extended sodic-calcic alteration all over the outer part of the granodiorite. Chlorite and chlorite-calcite veins are rare in contrast with the inner part, while large quartz ore-bearing sheeted veins are common. The ore mineralogy and petrography of those veins will be discussed below.

The southeastern part of the island is dominated by gneisses with metabasite intercalations of the Continental Basement Unit (CBU). In this area, the aplogranitic intrusive body is composed mainly of quartz (25-30 %), K-feldspar (32-43 %), plagioclase (15-27 %) and biotite (<5 %), while monazite, allanite, zircon and pyrite occur as accessory minerals (Table 1; Fig. 17). In contrast with the outer granodiorite, both the K-feldspar and the plagioclase are almost unaltered with no traces of secondary albite replacement. The sericitization of K-feldspar is rare (Fig. 20a) but increases in intensity towards the veins of hydrothermal quartz which occur all over the aplogranite.

Small (0,2-0,4 mm) biotite crystals occur as crystals assemblages within the aplogranite. Furthermore, allanite and monazite crystals (Fig. 20b) are widespread along the pluton. Tiny zircon inclusions occur within K-feldspar crystals (Fig. 20c). Secondary amphibole has replaced primary biotite (Fig. 20d, e) while in some cases secondary chlorite replacing primary biotite is present (Fig. 20f). The K-feldspars seems quite fresh, although in some cases are partly sericitized (Fig. 20f). Disseminated pyrite mineralization is also present and will be discussed below.

On the contrary, the aplogranite, exposed in the central part of the island in Kefala Hill area, is altered, where primary K-feldspars have been partly replaced by sericite. Disseminated pyrite crystals also occur, surrounded by supergene jarosite halos and veins.

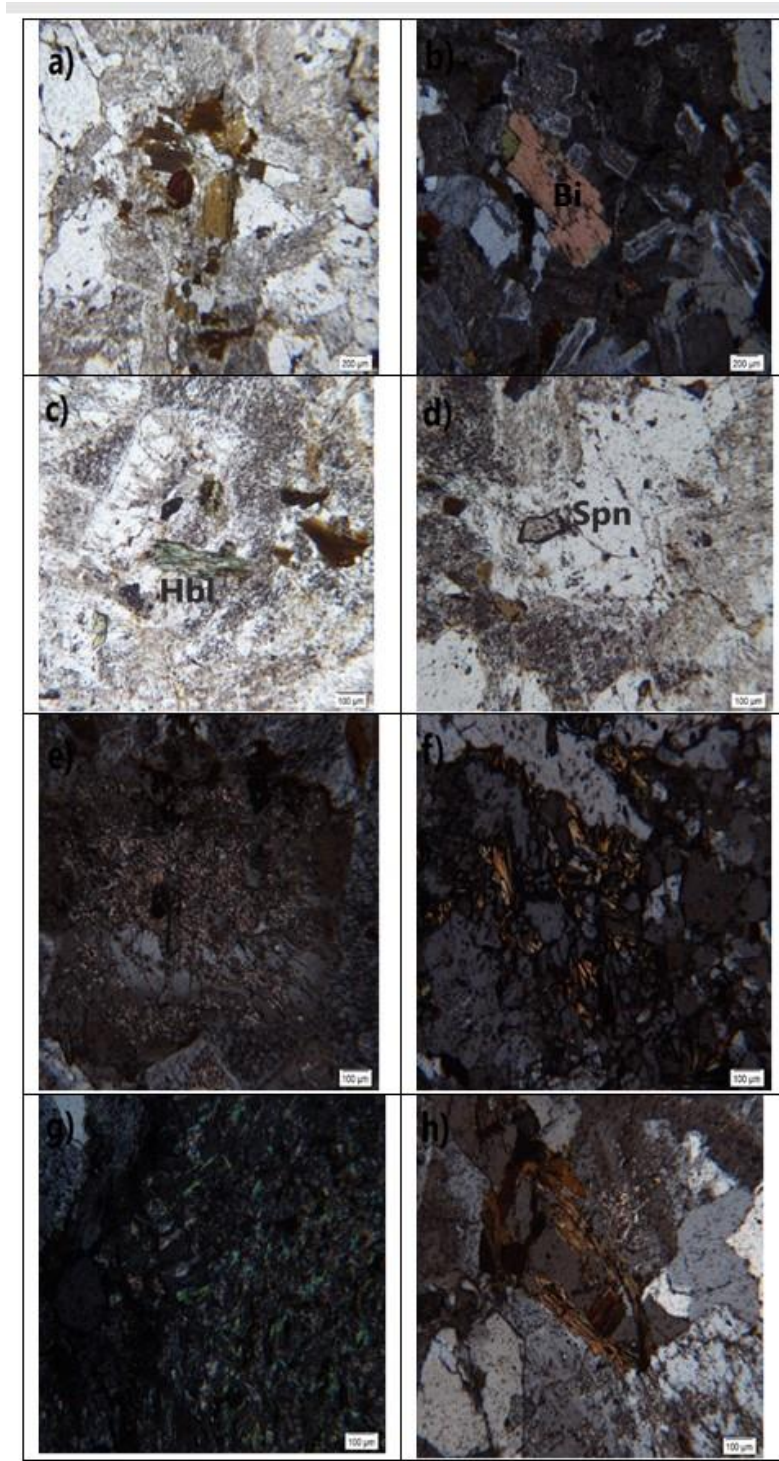


Fig. 19: Microphotographs of the outer (margin) part of the granodiorite: a) Secondary hydrothermal biotite assemblage; b) Primary magmatic biotite crystal and albitized plagioclase (the sodic-alteration is more intense to the core); c) Primary hornblende crystal; d) Primary titanite; e) Partly albitized and sericitized plagioclase; f) Secondary shreddy biotite with fresh K-feldspar and quartz; g) Secondary amphibole (actinolite) replacing plagioclase; h) Secondary shreddy biotite along with partly sericitized and albitized plagioclase and K-feldspar. (Bi= biotite, Hbl= hornblende. Spn= titanite)

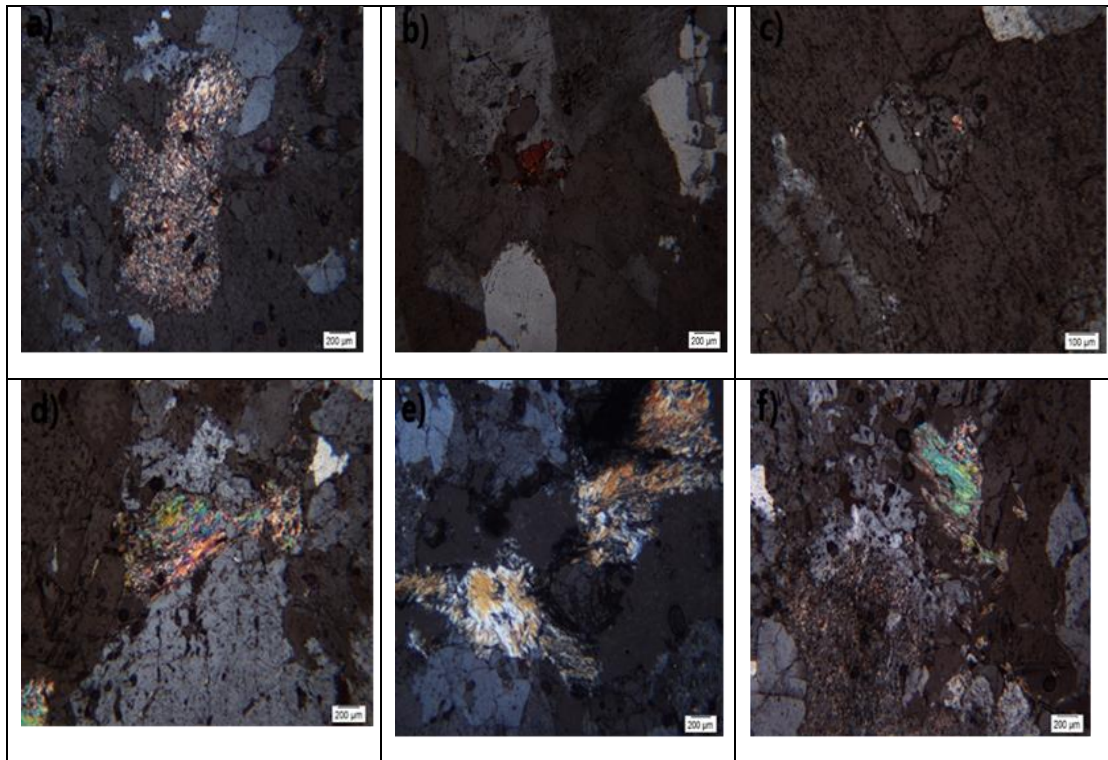


Fig. 20: Microphotographs of the aplogranite from the Sotiras area: a) Sericitized K-feldspar; b) Primary allanite crystal (red mineral) with fresh quartz and K-feldspar; c) Zircon inclusion inside K-feldspar; d) Altered primary biotite replaced by secondary amphibole; e) Secondary amphibole crystals; f) Chloritized biotite and sericitized K-feldspar from the aplogranite.

The contact between the granodiorite and the aplogranite at Ganema, is characterized by abundant primary biotite (Fig. 21 a,b), hornblende phenocrysts (Fig. 21 c, d,f) and primary titanite (Fig. 21 e). Primary hornblende crystals have been partly replaced by secondary hydrothermal biotite (Fig. 21g, h). The aplogranite intrudes the granodiorite indicating its younger age. The K-feldspar in the granodiorite is almost entirely replaced by secondary albite, while in the aplogranite the K-feldspar remains unaltered. Most of the plagioclase in the granodiorite maintains its original texture and is characterized by an anorthite-rich core and albite-rich margin. The biotite, hornblende and titanite are magmatic in origin and maintain their original phenocrystic texture. Apatite inclusions are preserved in the primary biotite crystals.

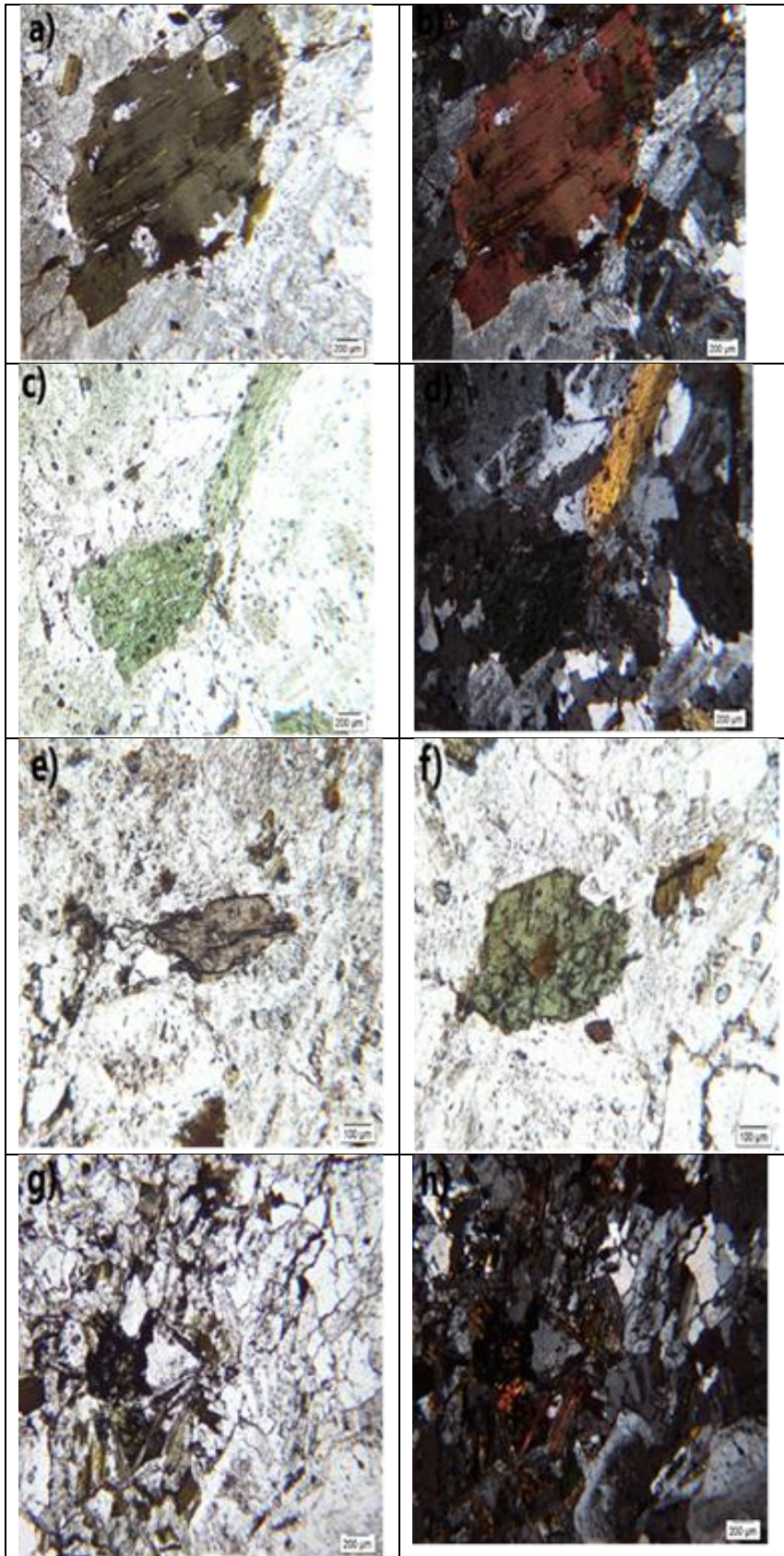


Fig. 21: Microphotographs from the contact between the granodiorite and the aplogranite at Ganema: a,b) Primary magmatic biotite; c,d) Primary magmatic hornblende; e) Primary magmatic titanite; f) Primary hornblende with biotite inclusion; g,h) Secondary hydrothermal biotite and amphibole crystals.

V.2. Ore mineralogy

As mentioned above, there are five different sulfide-bearing areas within both the Serifos granodiorite and the aplogranite.

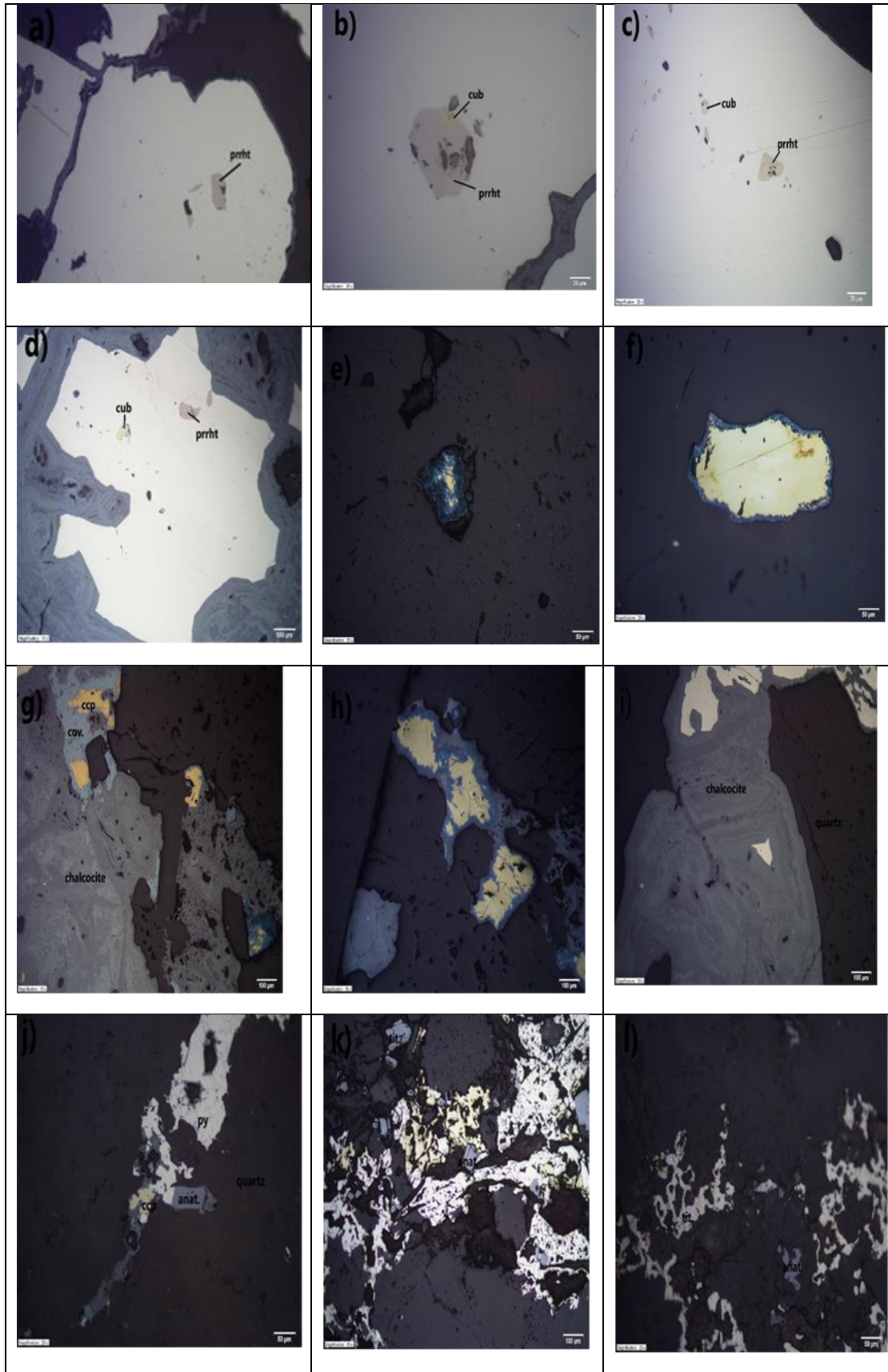
In the Chora area disseminated pyrite and chalcopyrite mineralization is present, and also secondary malachite and azurite were found.

In the Koutalas Bay area in the outer part of the granodiorite the sheeted quartz vein system consists of 15 sheeted veins. They are composed of quartz (20-70%) as a main gangue mineral, pyrite (5-60%) as a main ore mineral and chalcopyrite (2-5%) as a minor ore mineral. Pyrite crystals include pyrrhotite along with cubanite and chalcopyrite in grains of up to 50 μm (Fig. 22a-d). This paragenesis is a typical indicator of high-temperature hydrothermal deposits (Yang et al., 2009). Chalcocite surrounding pyrite, and needle-shaped covellite surrounding chalcopyrite are supergene minerals resulting from oxidation of chalcopyrite (Fig. 22e-i). The discovery of the granodiorite-hosted pyrite-chalcopyrite mineralization in the Koutalas area is of great importance, since both minerals are also present in the neighboring skarn bodies and have identical composition with the same sulfides inside the skarn deposit (see following chapters and discussion). Keeping that in mind, it is suggested that the granodiorite was the main source of metals that form the skarn deposit in the southwestern part of the island.

In the Sotiras Bay Area the disseminated mineralization inside the aplogranite consists almost entirely of pyrite. The pyrite crystals are $<50 \mu\text{m}$ comprising less than 10% of the aplogranite's volume. They are surrounded by chalcocite halos, suggesting the former presence of minor chalcopyrite in the mineralization. Voudouris et al. (2010) also reported on the presence of molybdenite accompanying pyrite from this area.

In the Kefala Hill area, in the central part of the island, the ore mineralization is associated with an aplogranite body intruding the border facies of the granodiorite. Similarly to the third mineralized site, disseminated-style pyrite mineralization is observed. Pyrite is surrounded by goethite.

In the Heliport area, a sulfide stockwork and breccia body crop out with quartz (15-70%) as gangue mineral, pyrite (20-65%) as the main ore phase and chalcopyrite (2-5%) as a minor ore phase. Inside the pyrite, only inclusions of chalcopyrite are observed, while pyrrhotite and cubanite inclusions are absent. Quartz includes small (20-100 μm) crystals of anatase, brookite, titanite and zircon, indicating the significant presence of Ti in this mineralization (Fig. 22j-l).



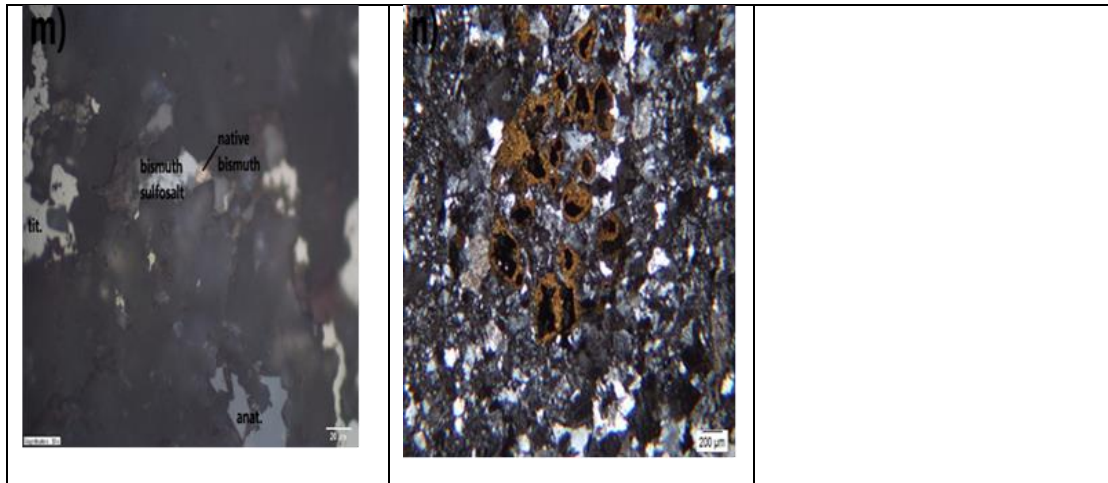


Fig. 22: Microphotographs of ore minerals in the various intrusion-hosted mineralization at Serifos (reflected light). (a to d) Pyrrhotite (Po) and cubanite (Cbn) inclusions in pyrite from the sheeted vein system in Koutalas Bay; e,f,g,h) Chalcopyrite crystals surrounded by bluish needle-shaped covellite and greyish chalcocite; i) Chalcocite surrounding pyrite crystals (j, k) Disseminated titanite (Spn) and anatase (Ant) crystals from the sulfide stockwork-style mineralization in Heliport area; (l, m) Bismuth sulfosalt and native bismuth from the Heliport area with Ti-oxides (anatase) and titanite; n) Disseminated pyrite from the Kefala area inside the aplogranite. The pyrite is surrounded by secondary jarosite.

V.3. Mineral identification (Raman Spectroscopy)

In the sheeted veins at Koutalas, the presence of chalcocite instead of goethite was testified. The chalcocite is supergene in origin and surrounds pyrite and sometimes chalcopyrite grains. Covellite is only found in vein number 15 which is characterized by larger chalcopyrite crystals than the other veins.

In the Sotiras area, where the aplogranite is the dominant rock type, large (>200 µm) allanite crystals occur. Those crystals are characterized by high relief and intense green and red color (Fig. 20b). All the three polymorphs of TiO₂ (rutile, anatase, brookite) were found in the area, along with edenite and grunerite which is a ferrous iron-rich amphibole with the formula type Fe₇Si₈O₂₂(OH)₂ (isomorph series with cummingtonite).

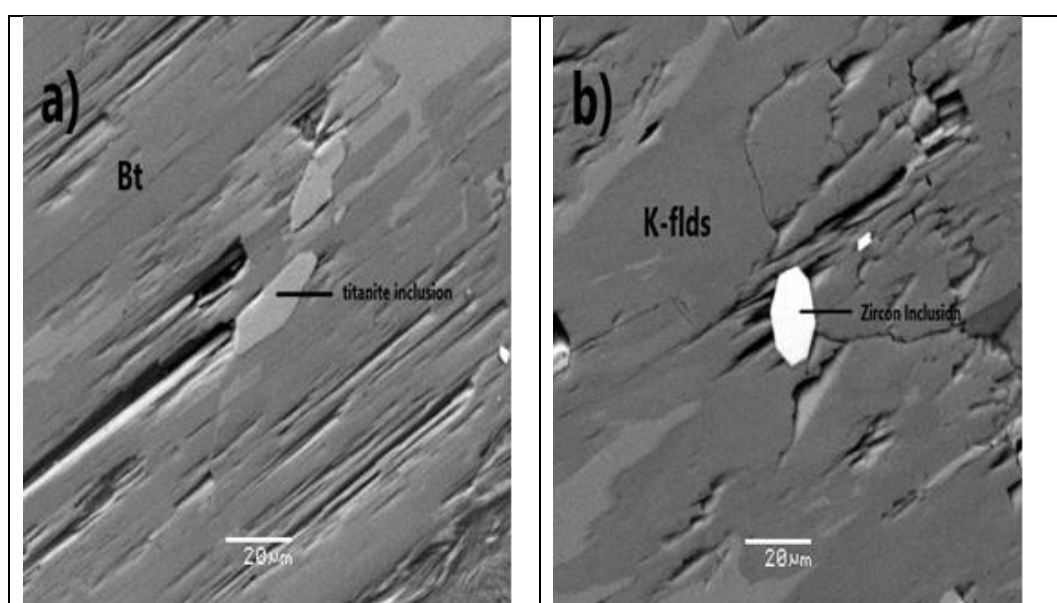
Finally, in the Heliport area, where the sulfide stockwork mineralization occurs, the presence of brookite and anatase was confirmed along with the presence of zircon and titanite.

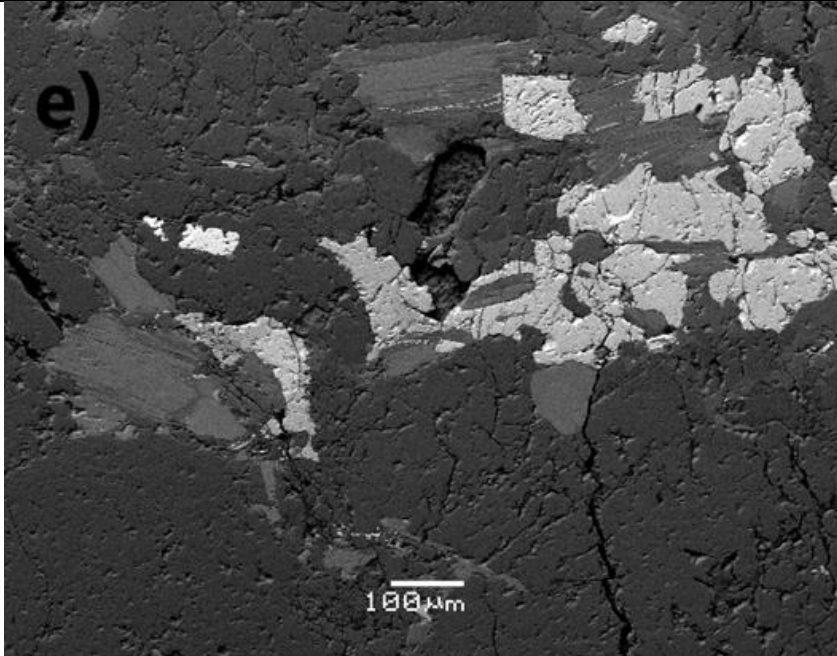
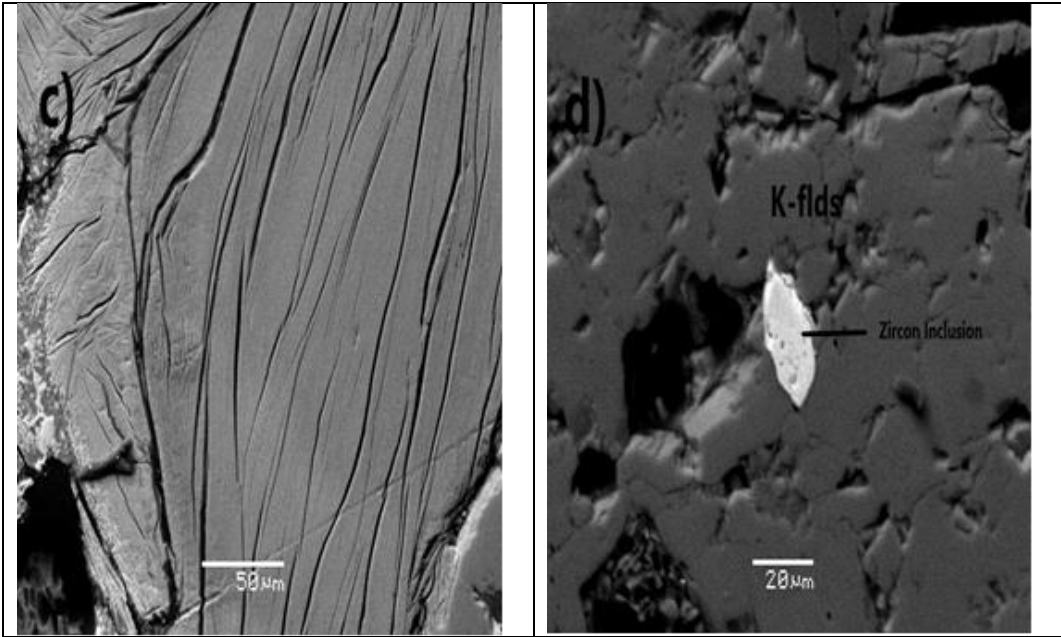
V.4. SEM-EDS determinations

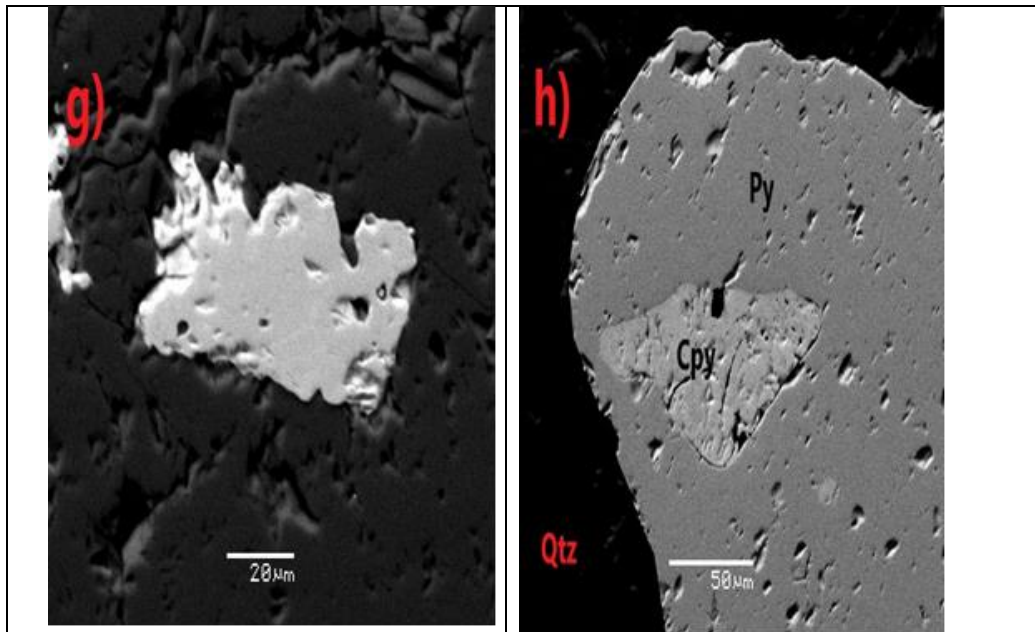
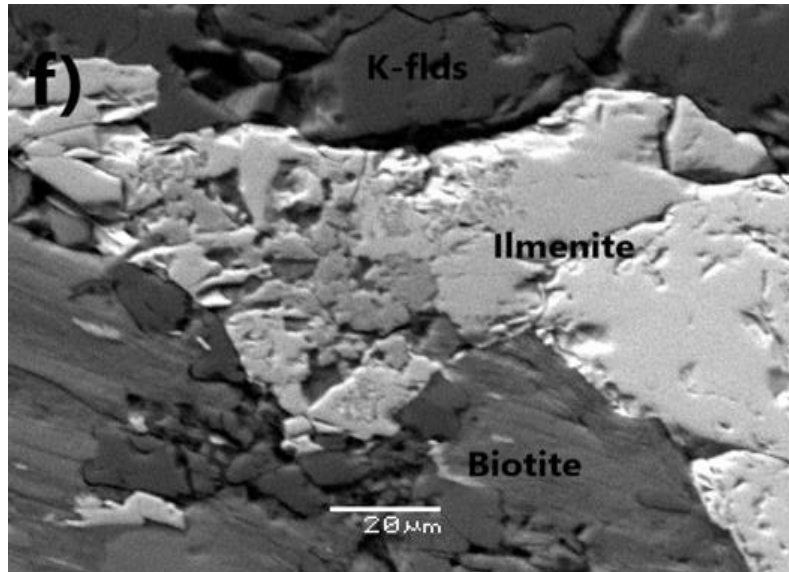
BSE images taken by SEM at the University of Athens are shown below. These include mostly silicates from the outer granodiorite at Koutalas, the aplogranite in the Sotiras and Kefala areas and the contact between them at Ganema.

Within a fresh biotite, small titanite inclusions occur (Fig. 23a). K-feldspar from both the granodiorite and the aplogranite, contains small (20-30 μm) zircon inclusions (Fig. 23b, d). Although no analysis has been done for the determination of the origin of these zircon crystals, they are believed to be primary and correspond to the last stages of the magma fractionation. Foliated biotite crystals are usual in the outer aplogranite (Fig. 23c). Within the aplogranite, ilmenite crystals occur instead of magnetite along with small zircon crystals (Fig. 23e, f, g). This body is characterized by disseminated pyrite mineralization, sometimes with chalcopyrite inclusions (Fig. 23h) as discussed above. Moreover, small (<100 μm) inclusions of monazite and tiny (<20 μm) inclusions of an unknown UO_2 mineral phase also occur (Fig. 23i). Finally, needle-shaped rutile crystals form a sagenite-type network within biotite crystals in the Sotiras area (Fig. 23k). The chemical composition of this undefined mineral has been testified via an EDS analysis.

Primary biotite, is characterized by the presence of small (20-30 μm) elongated titanite and apatite inclusions, especially within the granodiorite. Within the aplogranite, primary titanite and apatite are absent while ilmenite crystals surround primary biotites along with sagenite-type rutile crystals. This difference in the mineral composition between granodiorite and aplogranite may be another evidence for the existence of two different magmas, one more oxidized, magnetite-type for the formation of the main granodioritic body and another one more reduced, ilmenite-type for the formation of the aplogranite.







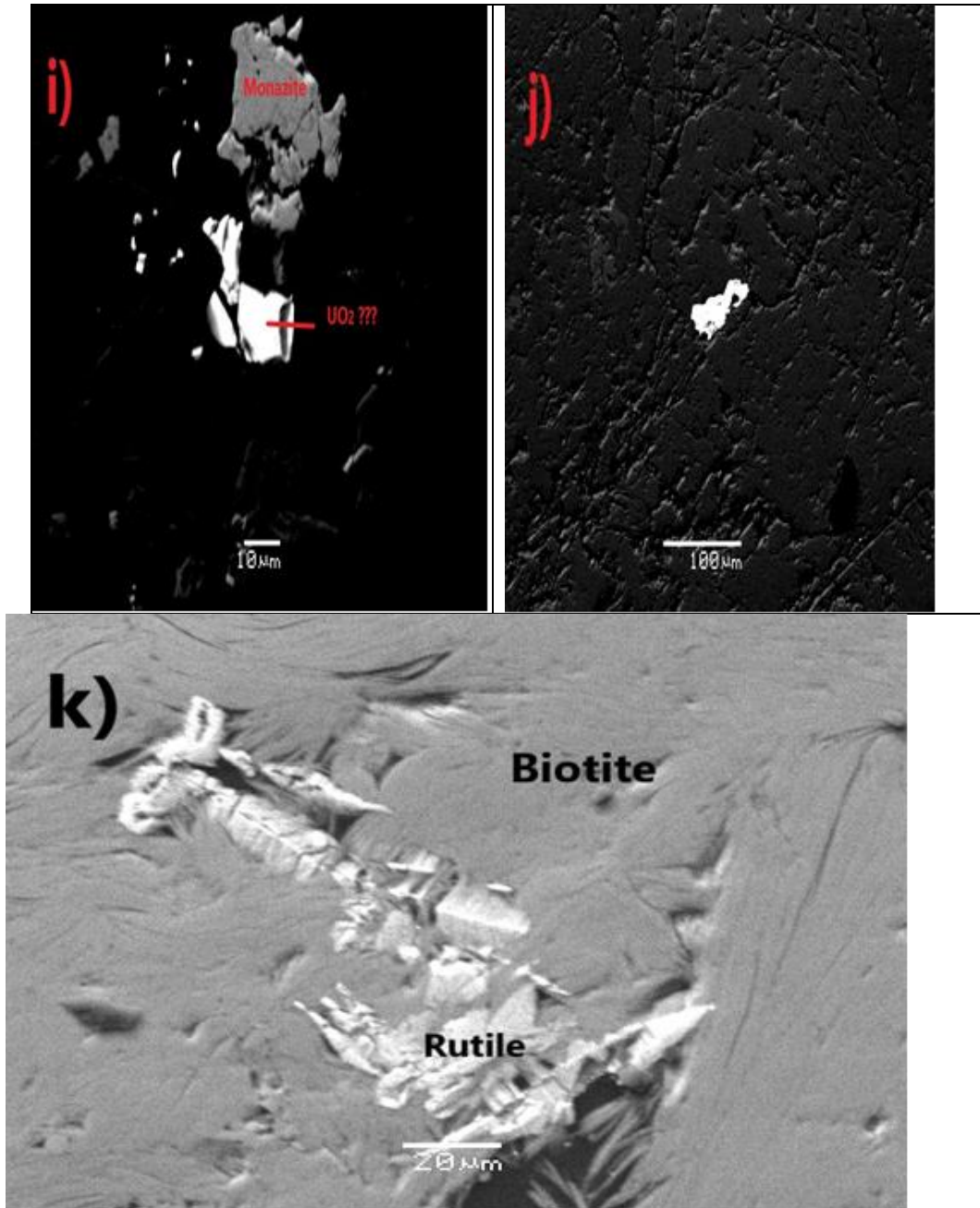


Fig. 23: Back-scattered electron (BSE) images of silicates from the granodiorite, the aplogranite and the contact between them: a) Titanite (Spn) inclusion in biotite (Bt) in the outer granodiorite; b) Primary zircon (Zrn) inclusion in K-feldspar (Kfs) in the outer granodiorite; c) Foliated biotite from the outer granodiorite; d) Rhombohedral zircon inclusion in K-feldspar from the aplogranite, Sotiras area; e) Biotite (Bt), ilmenite (Ilm) and zircon grains from the aplogranite, Sotiras area; f,g) Magnification from the previous image; h) Pyrite (Py) with a chalcopyrite (Ccp) inclusion from the aplogranite, Sotiras area; i) Monazite and an undefined U-rich mineral from the aplogranite, Sotiras area; j) Monazite (Mnz) from the aplogranite in contact with the granodiorite, Ganema area; k) Sagenite-type network with needle-shaped rutile inside biotite within the aplogranite, Sotiras area.

XY_22_39	XY_22_40	XY_22_41	XY_22_42	XY_22_43	XY_22_44	XY_22_45	XY_22_46	XY_22_47	XY_22_48	XY_22_49	XY_24_6	XY_24_7	XY_24_8	XY_24_9	XY_24_10	XY_24_11	XY_24_12	XY_24_13	XY_24_14	XY_24_15	XY_24_16	XY_24_17
62,78	64,5	64,21	55,96	60,92	55,53	56,96	53,77	55,4	60,4	60,39	63,86	63,83	64,16	64,15	63,28	64,78	64,47	62,21	62,56	63,92		
0	0,038	0,03	0	0	0	0	0,038	0,025	0	0,038	0,025	0	0	0,025	0	0,025	0	0,026	0	0,029		
22,47	17,99	17,58	27,19	23,47	27,04	26,24	28,89	27,25	24,42	24,43	18,75	18,32	18,34	18,29	18,26	18,38	18,38	18,07	18,09	18,11		
0,157	0,078	0,422	0,126	0,178	0,15	0,107	0,256	0,193	0,134	0,156	0,05	0,042	0,073	0,105	0,053	0,105	0,065	0,058	0,069	0,03		
0	0	0,287	0	0	0	0	0	0	0	0	0	0	0	0	0	0	0	0	0	0		
4,12	0,03	0,446	9,42	5,42	9,66	8,69	11,29	9,88	6,27	6,28	0,072	0,017	0,028	0,026	0,031	0,017	0	0,026	0,021	0,024		
8,95	0,952	0,379	6,07	8,28	5,92	6,46	5,04	5,88	7,89	8,07	1,058	0,673	0,747	0,662	0,777	1,129	0,597	0,571	0,555	0,843		
0,376	15,18	15,64	0,239	0,427	0,23	0,214	0,165	0,211	0,254	0,253	14,92	15,73	15,31	15,99	15,36	15,2	16,14	15,53	15,12	15,1		
0	0	0,154	0	0,026	0,057	0,044	0	0,032	0	0	1,02	0,542	0,331	0,336	0,479	0,298	0,175	0,208	0,21	0		
98,853	98,768	99,148	99,005	98,721	98,587	98,715	99,411	98,846	99,368	99,617	99,755	99,154	98,989	99,584	98,24	99,934	99,827	96,699	96,625	98,056		
8	8	8	8	8	8	8	8	8	8	8	8	8	8	8	8	8	8	8	8	8		
2,809728	3,007596	3,000325	2,540331	2,744112	2,534861	2,58717	2,445184	2,524285	2,705229	2,700882	2,970787	2,98619	2,993676	2,987858	2,983872	2,993784	2,991099	2,979704	2,988883	3,000922		
1,185343	0,988756	0,968239	1,454856	1,246101	1,454894	1,404808	1,548522	1,463502	1,289172	1,287841	1,028116	1,010221	1,008644	1,004096	1,014875	1,001205	1,005117	1,020162	1,018706	1,002154		
0	0,001333	0,001054	0	0	0	0	0	0	0	0,001278	0,000875	0	0	0,000876	0	0,000869	0	0,000937	0	0,001024		
0,005876	0,003042	0,016491	0,004784	0,006706	0,005727	0,004065	0,009736	0,007355	0,005019	0,005835	0,001945	0,001643	0,002849	0,00409	0,00209	0,004058	0,002522	0,002323	0,002757	0,001178		
0	0	0	0	0	0	0	0	0	0	0	0	0	0	0	0	0	0	0	0	0		
0	0	0,019991	0	0	0	0	0	0	0	0	0	0	0	0	0	0	0	0	0	0		
0	0	0	0	0	0	0	0	0	0	0	0	0	0	0	0	0	0	0	0	0		
0,197576	0,001499	0,02233	0,458203	0,261599	0,472496	0,42293	0,550123	0,482369	0,300905	0,30095	0,003589	0,000852	0,0014	0,001298	0,001566	0,000842	0	0,001334	0,001075	0,001207		
0,776688	0,086075	0,034339	0,534296	0,723191	0,523997	0,568942	0,444409	0,519501	0,685212	0,699834	0,095435	0,06105	0,067584	0,059786	0,071042	0,101171	0,053707	0,053031	0,051415	0,076741		
0,021464	0,902861	0,932162	0,013839	0,024533	0,013392	0,012398	0,009571	0,012263	0,014511	0,014433	0,88532	0,938665	0,911181	0,94995	0,923834	0,896009	0,955137	0,948797	0,92141	0,904241		
0	0	0,00282	0	0,000459	0,00102	0,000783	0	0,000571	0	0	0,018592	0,009935	0,006051	0,006132	0,00885	0,005396	0,003181	0,003904	0,003931	0		
4,996677	4,991161	4,997752	5,006308	5,0067	5,006386	5,001096	5,007545	5,009846	5,000047	5,011052	5,004659	5,008557	4,991385	5,014086	5,006129	5,003334	5,010764	5,010192	4,988177	4,987467		
2,155653	91,15802	94,26908	1,375168	2,430686	1,326086	1,234545	0,953162	1,209219	1,450166	1,421646	89,94009	93,81325	92,96205	93,95828	92,71325	89,77853	94,67642	94,5806	94,61037	92,06384		
78,00198	8,690637	3,472668	53,09312	71,65109	51,88682	56,65227	44,25932	51,22611	68,47823	68,93442	9,695309	6,101577	6,895132	5,913384	7,129566	10,13712	5,323584	5,286379	5,279241	7,813241		
19,84236	0,151339	2,258252	45,53171	25,91823	46,78709	42,11319	54,78752	47,56468	30,07161	29,64393	0,364605	0,085171	0,142822	0,128341	0,157187	0,08435	0	0,133018	0,110385	0,122922		

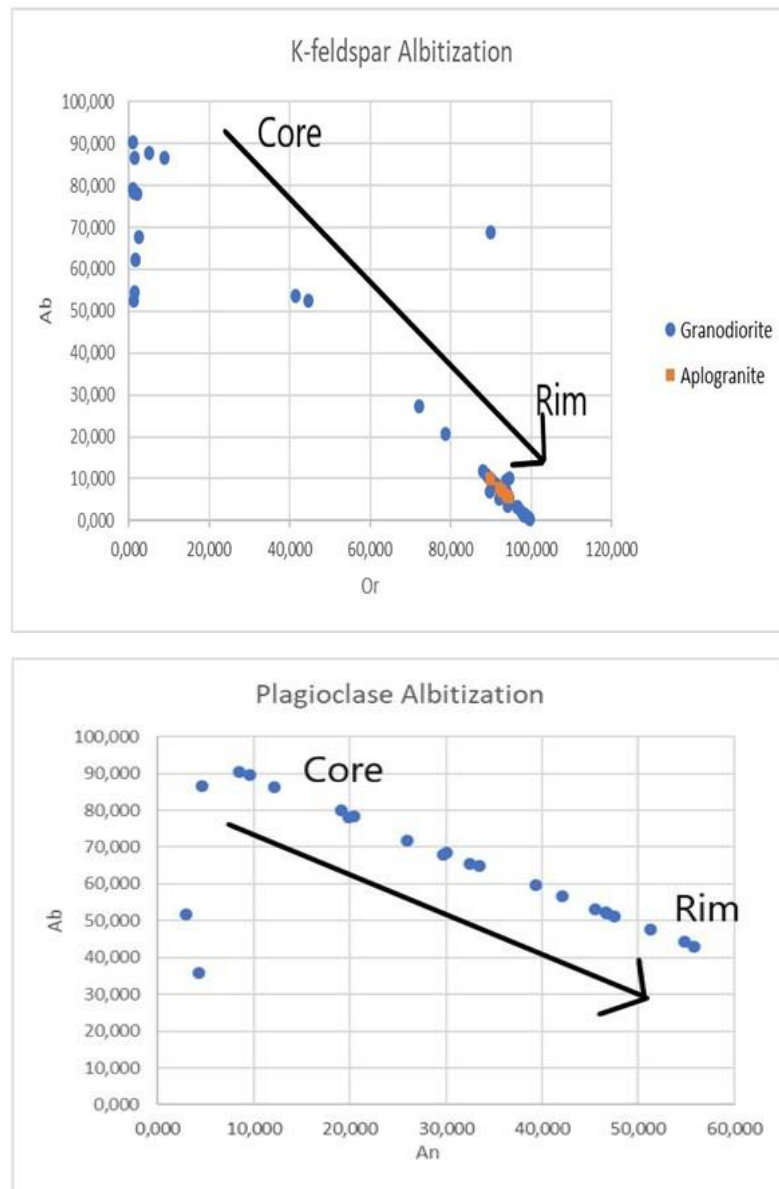


Fig.24: Diagrams describing the albitization for a) K-feldspars and b) from plagioclase. K-feldspars from the aplogranite are unaltered and therefore they preserve their primary composition

Biotite

Primary biotite phenocrysts along with hydrothermal shreddy biotite grains from the granodiorite were analyzed from two different sites. The first one is Koutalas area very close to the sheeted veins, while the second one is located in the Ganema beach, where the granodiorite is intruded by the biotite-poor aplogranite body. In every grain analyzed, two micro-analyses were conducted, the first one in the center of the crystal and the second one in the rim, although no important differences in the chemical composition were observed. The criteria used for the discrimination between primary

and hydrothermal biotite are based mostly on textural features. Primary, magmatic biotite is well-shaped, forming phenocrysts $>500\ \mu\text{m}$ and appears individually within the granodiorite. Hydrothermal, shreddy biotite forms smaller, subhedral, often aggregated crystals.

The chemical composition of Serifos biotites is presented in Table 3, and plotted in the Al_{total} vs $\text{Fe}/(\text{Mg}+\text{Fe})$ binary diagram (Fig. 25) and in the correlation diagrams of $\text{MgO}/\text{FeO}_{\text{Total}}$, MgO/TiO_2 , F/Cl vs F , F/Cl , $\text{X}_{\text{Mg}}/\text{Si}$ and Ti/Si (Fig. 26). The majority of the analyzed crystals are projected along the border between Annite and Phlogopite in the Al_{total} vs $\text{Fe}/(\text{Mg}+\text{Fe})$ binary diagram (Fig. 25). The hydrothermal biotites, seem to have lower $\text{Fe}/(\text{Mg}+\text{Fe})$ ratio than the primary biotites, while the Al remains stable.

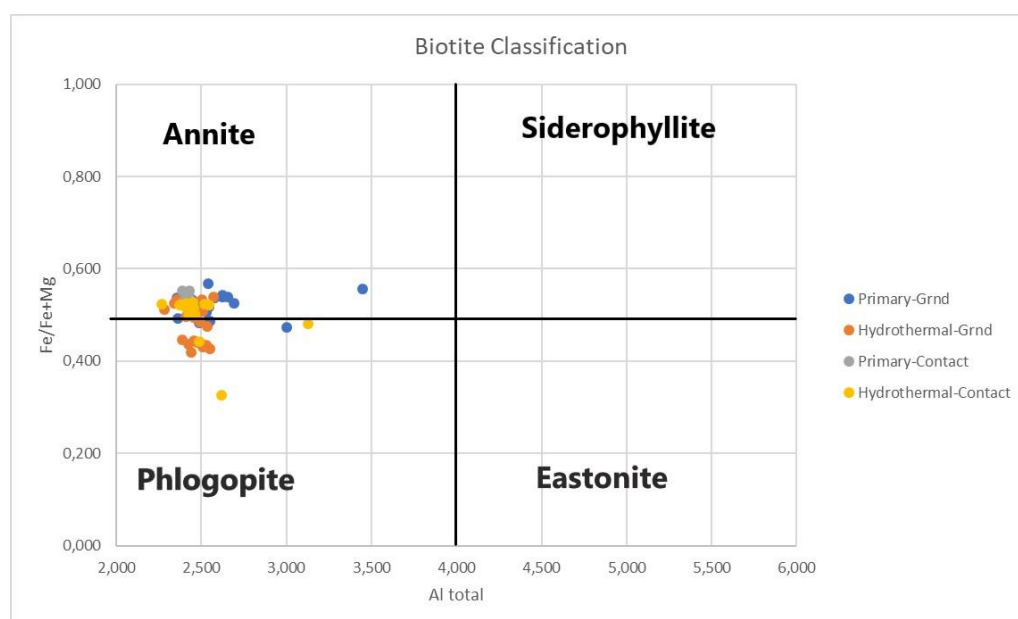


Fig. 25: Biotite classification using the Al_{total} vs $\text{Fe}/(\text{Mg}+\text{Fe})$ binary diagram. Note that all analyzed primary biotite crystals are projected in the field of annite, while the hydrothermal biotites are projected along the border between the annite and the phlogopite fields.

No significant differences on the major element mineral chemistry between the primary and the hydrothermal crystals were observed. The primary biotites from both sites seem to have higher $\text{FeO}_{\text{Total}}$ and lower MgO proportions (Fig. 26 a,b). All the other oxides, SiO_2 , TiO_2 , Al_2O_3 , CaO and MnO along with the alkalis Na_2O , K_2O are in the same concentration in the two types of biotite. The hydrothermal biotite from Ganema have the highest Cl content, $> 0,6\ \text{wt. \%}$, while the chlorine content from both primary and hydrothermal biotite remain constant. Generally, biotites from the Koutalas area have higher halogen content than those from the Ganema area. The hydrothermal biotite from Koutalas area, seem to have $\text{X}_{\text{Mg}} > 2,5$ but the same TiO_2 contents with primary biotite (Fig. 26b). As far as the halogen content is concerned, hydrothermal biotite from the Koutalas area has the highest F and F/Cl values (Figs. 26d and, e respectively), while no significant differences are shown on the $\text{X}_{\text{Mg}}/\text{Si}$ and Ti/Si diagrams.

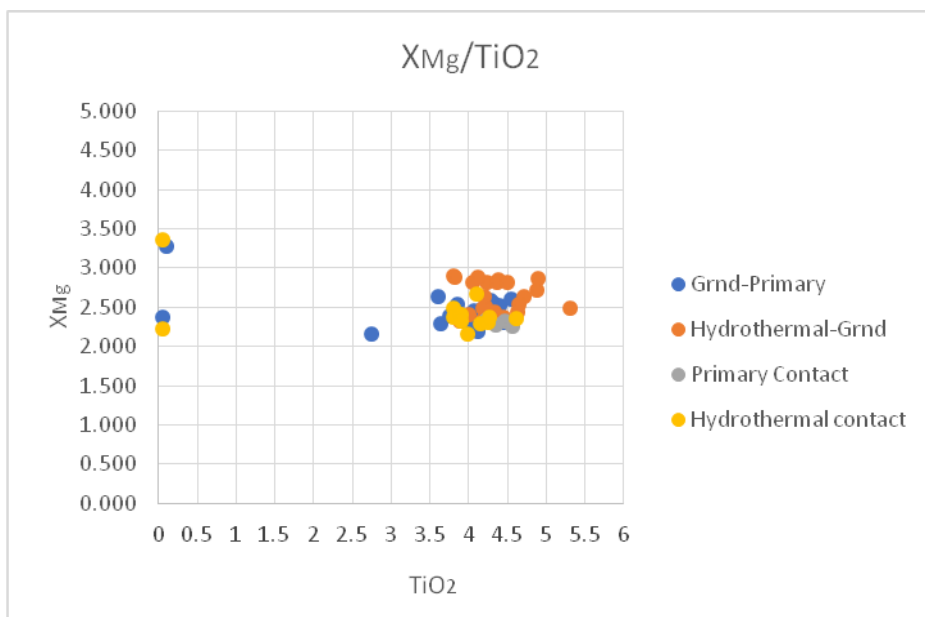
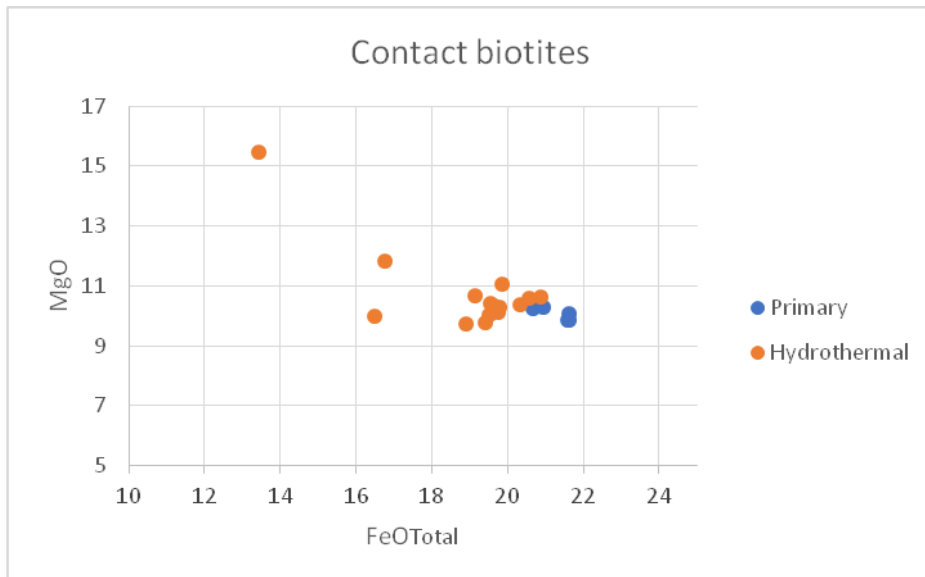
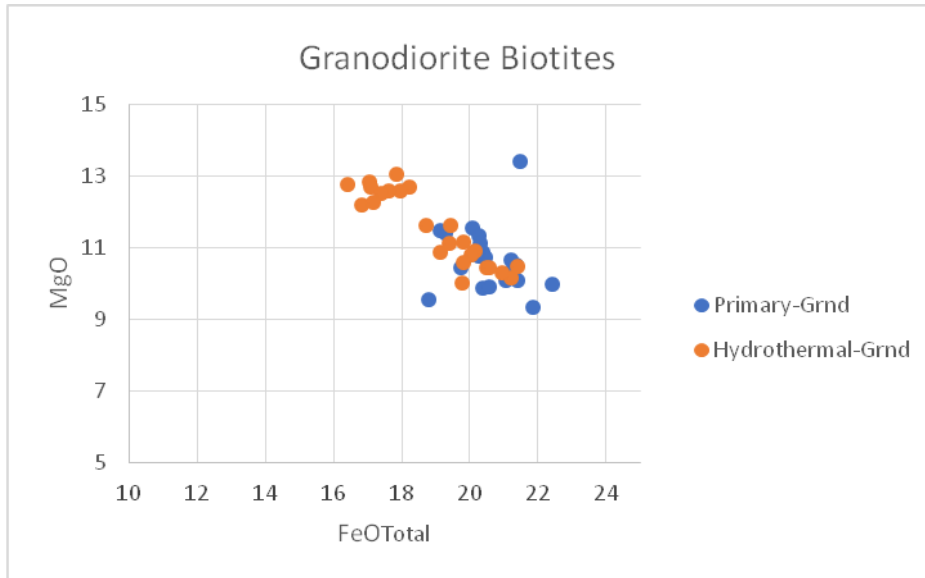
Table 3: Chemical composition of biotite from Serifos island

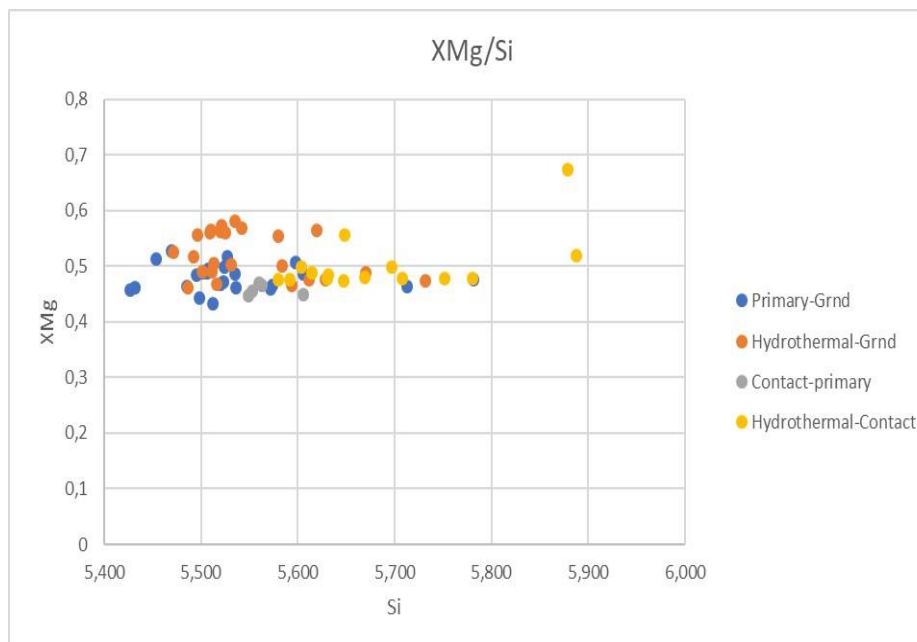
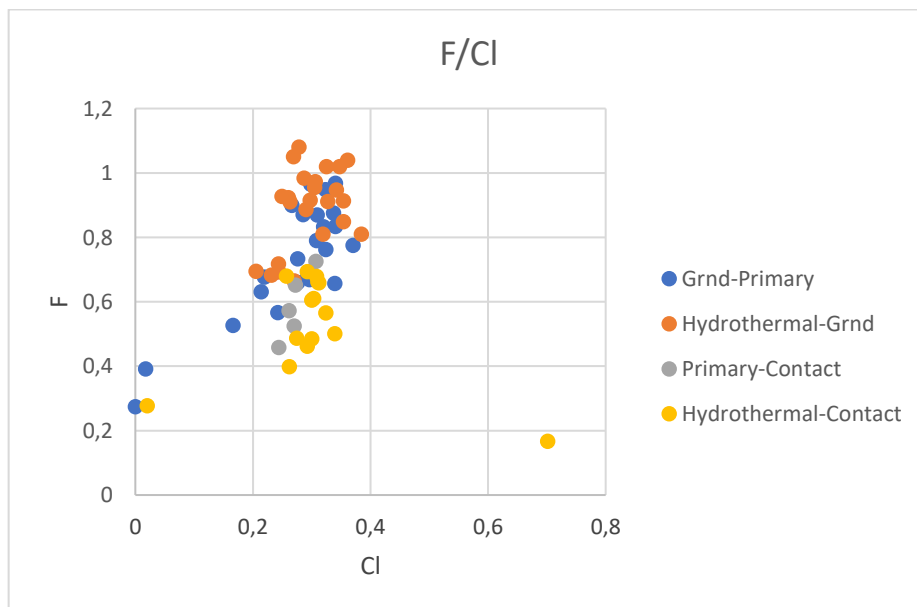
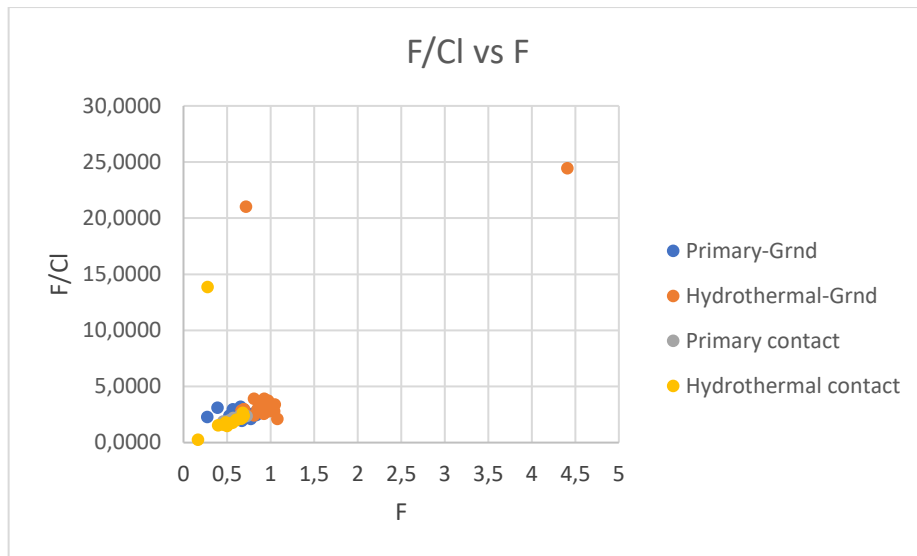
Sample	XY_9_7	XY_9_8	XY_9_3	XY_9_4	XY_9_5	XY_9_6	XY_9_9	XY_9_10	XY_9_11	XY_9_12	XY_9_13	XY_9_14	XY_9_15	XY_9_16	XY_9_19	XY_9_20
SiO2	36,16	36,61	35,83	34,94	34,97	35,78	36,13	36,51	36,1	37,58	35,75	37,44	35,53	37,43	35,76	36,04
TiO2	4,17	3,61	4,25	4,41	4,24	4,06	4,29	4,32	5,3	4,87	4,22	4,19	4,19	4,05	4,25	4,2
Al2O3	14	13,11	13,41	14,35	14,35	14,06	13,43	13,56	13,35	13,76	13,84	13,81	14,12	13,59	13,77	13,89
FeO	20,39	20,06	20,26	21,39	21,15	20,44	21,22	20,27	19,13	16,83	20,15	19,82	21,19	18,23	20,96	19,44
MnO	0,145	0,1	0,184	0,137	0,193	0,177	0,234	0,173	0,094	0,085	0,13	0,17	0,233	0,091	0	0,136
MgO	10,87	11,55	10,76	10,09	10,15	10,72	10,67	11,34	10,88	12,2	10,91	11,16	10,16	12,68	10,3	11,63
CaO	0,033	0,018	0,081	0,016	0,012	0,029	0	0,021	0	0,058	0,023	0,017	0	0,01	0,029	0,012
Na2O	0,122	0,089	0,148	0,121	0,144	0,122	0,166	0,085	0,13	0,099	0,173	0,157	0,124	0,062	0,09	0,093
F	0,833	0,968	0,775	0,677	0,762	0,876	0,871	0,948	0,913	0,91	0,886	0,923	0,81	1,08	0,81	0,849
Cl	0,32	0,34	0,37	0,293	0,324	0,337	0,285	0,323	0,354	0,263	0,29	0,26	0,319	0,278	0,384	0,354
Li2O*	0,83	0,96	0,73	0,48	0,48	0,72	0,82	0,93	0,81	1,23	0,71	1,19	0,65	1,19	0,71	0,79
H2O*	3,46	3,38	3,42	3,47	3,42	3,40	3,44	3,43	3,39	3,51	3,40	3,52	3,42	3,44	3,41	3,44
Subtotal	100,63	100,12	99,31	99,20	99,36	99,95	100,66	101,23	99,50	99,78	99,58	102,03	99,60	101,40	99,75	100,27
O=F,Cl	0,42	0,48	0,41	0,35	0,39	0,44	0,43	0,47	0,46	0,44	0,44	0,45	0,41	0,52	0,43	0,44
Total	100,21	99,63	98,90	98,84	98,96	99,51	100,23	100,76	99,04	99,34	99,14	101,58	99,19	100,88	99,32	99,83
F/Cl	2,6031	2,8471	2,0946	2,3106	2,3519	2,5994	3,0561	2,9350	2,5791	3,4601	3,0552	3,5500	2,5392	3,8849	2,1094	2,3983
Si	5,506	5,598	5,536	5,426	5,432	5,496	5,523	5,524	5,531	5,619	5,501	5,584	5,487	5,580	5,517	5,493
Al iv	2,494	2,363	2,442	2,574	2,568	2,504	2,420	2,418	2,411	2,381	2,499	2,416	2,513	2,388	2,483	2,495
Al vi	0,021	0,000	0,000	0,053	0,059	0,041	0,000	0,000	0,000	0,044	0,012	0,012	0,057	0,000	0,020	0,000
Ti	0,478	0,415	0,494	0,515	0,495	0,469	0,493	0,492	0,611	0,548	0,488	0,470	0,487	0,454	0,493	0,481
Cr	0,000	0,000	0,000	0,000	0,000	0,000	0,000	0,000	0,000	0,000	0,000	0,000	0,000	0,000	0,000	0,000
Fe	2,597	2,565	2,618	2,778	2,747	2,626	2,713	2,565	2,451	2,105	2,593	2,472	2,737	2,273	2,704	2,478
Mn	0,019	0,013	0,024	0,018	0,025	0,023	0,030	0,022	0,012	0,011	0,017	0,021	0,030	0,011	0,000	0,018
Mg	2,467	2,633	2,478	2,336	2,350	2,455	2,431	2,558	2,485	2,719	2,503	2,481	2,339	2,818	2,369	2,642
Li*	0,506	0,587	0,454	0,297	0,303	0,443	0,502	0,564	0,498	0,742	0,438	0,716	0,401	0,714	0,441	0,485
Ca	0,005	0,003	0,013	0,003	0,002	0,005	0,000	0,003	0,000	0,009	0,004	0,003	0,000	0,002	0,005	0,002
Na	0,036	0,026	0,044	0,036	0,043	0,036	0,049	0,025	0,039	0,029	0,052	0,045	0,037	0,018	0,027	0,027
K	1,804	1,820	1,791	1,749	1,815	1,808	1,776	1,799	1,769	1,598	1,786	1,783	1,745	1,763	1,826	1,825
OH*	3,516	3,444	3,524	3,590	3,540	3,487	3,505	3,464	3,466	3,503	3,493	3,499	3,521	3,421	3,504	3,499
F	0,401	0,468	0,379	0,333	0,374	0,426	0,421	0,454	0,442	0,430	0,431	0,435	0,396	0,509	0,395	0,409
Cl	0,083	0,088	0,097	0,077	0,085	0,088	0,074	0,083	0,092	0,067	0,076	0,066	0,084	0,070	0,100	0,091
TOTAL	19,932	20,023	19,895	19,786	19,840	19,906	19,938	19,969	19,806	19,805	19,893	20,004	19,833	20,019	19,885	19,947

XY_9_21	XY_9_22	XY_9_23	XY_9_25	XY_9_26	XY_9_27	XY_9_42	XY_9_43	XY_9_53	XY_9_54	XY_9_57	XY_9_58	XY_9_59	XY_9_60	XY_9_61	XY_9_62	XY11_1	XY11_2
36,51	36,77	36,46	36,19	36,57	37,07	35,44	36,62	36,04	35,76	36,45	35,66	35,54	35,98	35,92	36,81	34,49	33,4
3,81	4,24	3,82	4,38	4,37	4,11	4,39	4,29	4,71	4,09	4,63	4,5	4,54	3,85	4,64	4,9	0,058	0,107
14,31	13,98	13,99	13,72	14,01	14,45	13,37	13,99	14,16	14,27	14,01	13,7	14,12	14,01	13,57	13,76	18,36	15,56
17,06	17,62	17,11	17,98	17,4	17,85	20,24	19,14	18,72	21,15	20,02	17,17	19,3	20,29	19,41	16,43	22,41	21,46
0,064	0,068	0,061	0,089	0,08	0,098	0,248	0,147	0,06	0,106	0,114	0,092	0,079	0,163	0,093	0,059	0,092	0,145
12,84	12,59	12,7	12,59	12,51	13,03	10,87	11,49	11,61	10,25	10,81	12,26	11,39	11,11	11,11	12,76	9,99	13,41
0,012	0,03	0,048	0,012	0,021	0,017	0,018	0,023	0,02	0,016	0,047	0,114	0,037	0,029	0,043	0,031	0,463	1,1
0,113	0,147	0,097	0,145	0,049	0,084	0,144	0,177	0,125	0,145	0,181	0,158	0,094	0,175	0,089	0,117	0,147	0,146
1,02	0,955	0,984	0,947	1,02	1,04	0,899	0,965	0,911	0,79	0,915	0,973	0,87	0,834	0,927	1,05	0,274	0,391
0,347	0,305	0,287	0,342	0,325	0,361	0,266	0,298	0,327	0,308	0,297	0,306	0,309	0,34	0,249	0,269	0	0,017
0,93	1,00	0,91	0,83	0,94	1,09	0,62	0,96	0,79	0,71	0,91	0,68	0,65	0,77	0,76	1,01	0,35	0,03
3,39	3,46	3,41	3,41	3,41	3,45	3,37	3,44	3,43	3,46	3,46	3,34	3,42	3,44	3,40	3,42	3,63	3,47
99,77	100,60	99,35	99,90	100,13	101,13	99,04	100,85	100,24	100,27	101,04	97,95	99,56	100,05	99,59	100,03	92,51	89,90
0,51	0,47	0,48	0,48	0,50	0,52	0,44	0,47	0,46	0,40	0,45	0,48	0,44	0,43	0,45	0,50	0,12	0,17
99,26	100,13	98,88	99,43	99,63	100,61	98,60	100,37	99,78	99,87	100,59	97,47	99,13	99,62	99,15	99,53	92,40	89,73
2,9395	3,1311	3,4286	2,7690	3,1385	2,8809	3,3797	3,2383	2,7859	2,5649	3,0808	3,1797	2,8155	2,4529	3,7229	3,9033	#ΔIAP./01	23,0000
5,522	5,526	5,543	5,497	5,521	5,510	5,502	5,528	5,472	5,485	5,511	5,509	5,453	5,507	5,514	5,535	5,498	5,470
2,478	2,474	2,457	2,456	2,479	2,490	2,446	2,472	2,528	2,515	2,489	2,491	2,547	2,493	2,455	2,439	2,502	2,530
0,073	0,002	0,049	0,000	0,014	0,042	0,000	0,017	0,006	0,065	0,008	0,004	0,007	0,035	0,000	0,000	0,948	0,473
0,433	0,479	0,437	0,500	0,496	0,459	0,513	0,487	0,538	0,472	0,526	0,523	0,524	0,443	0,536	0,554	0,007	0,013
0,000	0,000	0,000	0,000	0,000	0,000	0,000	0,000	0,000	0,000	0,000	0,000	0,000	0,000	0,000	0,000	0,000	0,000
2,158	2,214	2,175	2,284	2,197	2,219	2,628	2,416	2,377	2,713	2,531	2,218	2,477	2,597	2,492	2,066	2,988	2,939
0,008	0,009	0,008	0,011	0,010	0,012	0,033	0,019	0,008	0,014	0,015	0,012	0,010	0,021	0,012	0,008	0,012	0,020
2,895	2,820	2,878	2,851	2,815	2,887	2,515	2,585	2,628	2,344	2,436	2,823	2,605	2,535	2,542	2,860	2,374	3,274
0,563	0,605	0,558	0,510	0,573	0,650	0,387	0,582	0,483	0,439	0,553	0,424	0,400	0,477	0,467	0,612	0,222	0,022
0,002	0,005	0,008	0,002	0,003	0,003	0,003	0,004	0,003	0,003	0,008	0,019	0,006	0,005	0,007	0,005	0,079	0,193
0,033	0,043	0,029	0,043	0,014	0,024	0,043	0,052	0,037	0,043	0,053	0,047	0,028	0,052	0,026	0,034	0,045	0,046
1,806	1,808	1,838	1,794	1,816	1,608	1,816	1,793	1,807	1,804	1,774	1,772	1,805	1,769	1,837	1,805	0,457	0,123
3,423	3,468	3,453	3,457	3,430	3,420	3,489	3,463	3,478	3,537	3,486	3,444	3,497	3,508	3,485	3,432	3,862	3,793
0,488	0,454	0,473	0,455	0,487	0,489	0,441	0,461	0,437	0,383	0,438	0,475	0,422	0,404	0,450	0,499	0,138	0,203
0,089	0,078	0,074	0,088	0,083	0,091	0,070	0,076	0,084	0,080	0,076	0,080	0,080	0,088	0,065	0,069	0,000	0,005
19,971	19,985	19,980	19,948	19,938	19,905	19,885	19,954	19,887	19,896	19,904	19,842	19,862	19,934	19,888	19,917	19,133	19,111
6,130	6,130	6,105	6,156	6,105	6,270	6,075	6,106	6,040	6,046	6,069	6,004	6,023	6,109	6,049	6,100	6,551	6,742
1,841	1,855	1,875	1,839	1,834	1,635	1,862	1,848	1,847	1,850	1,835	1,838	1,839	1,826	1,870	1,844	0,582	0,369

XY11_3	XY11_4	XY11_5	XY11_6	XY11_7	XY11_8	XY11_9	XY11_10	XY11_11	XY11_12	XY11_13	XY11_14	XY11_15	XY22_1	XY22_2	XY22_13	XY22_16	XY22_17
35,07	36,17	36,78	37	38,11	35,68	36,13	36,19	36,41	36,93	36,57	36,67	36,8	36,53	35,99	39,44	36,41	40,38
4,12	4,44	4,33	4,01	2,74	3,64	4,28	3,76	3,89	3,89	4	4,33	4,45	4,23	4,21	0,047	3,86	0,05
13,71	13,35	13,76	12,94	15,07	14,52	13,49	13,46	13,03	12,86	13,18	12,53	13,02	13,26	13,29	17,79	13,06	15,27
21,85	21,05	19,74	20,37	18,79	20,58	21,35	21,27	21,39	19,76	20,49	19,83	20,56	20,66	21,61	16,48	19,78	13,42
0,171	0,14	0,136	0,22	0,183	0,207	0,385	0,358	0,203	0,148	0,17	0,178	0,156	0,374	0,336	0,108	0,246	0,087
9,35	10,07	10,44	9,88	9,55	9,9	10,5	10,42	10,49	10,02	10,45	10,58	10,44	10,24	10,09	10	10,27	15,48
0,007	0,028	0,032	0,125	0,254	0,248	0,016	0,12	0,048	0,116	0,092	0,066	0,051	0,013	0	0,182	0,04	0,195
0,18	0,107	0,087	0,125	0,086	0,07	0,192	0,16	0,074	0,1	0,128	0,097	0,102	0,124	0,138	0,138	0,132	0,126
0,669	0,677	0,657	0,566	0,527	0,631	0,66	0,733	0,695	0,683	0,665	0,693	0,717	0,725	0,652	0,167	0,501	0,277
0,296	0,219	0,339	0,242	0,166	0,214	0,276	0,276	0,205	0,231	0,27	0,244	0,243	0,307	0,272	0,701	0,339	0,02
0,51	0,83	1,00	1,07	1,39	0,69	0,82	0,83	0,90	1,05	0,94	0,97	1,01	0,93	0,78	1,77	0,90	2,04
3,42	3,52	3,54	3,55	3,66	3,51	3,54	3,48	3,52	3,48	3,51	3,49	3,53	3,49	3,51	3,76	3,53	3,98
98,49	99,48	99,66	98,27	98,03	98,40	100,69	99,54	100,05	97,72	99,11	98,54	100,29	99,69	99,93	97,33	97,75	98,33
0,35	0,33	0,35	0,29	0,26	0,31	0,34	0,37	0,34	0,34	0,34	0,35	0,36	0,37	0,34	0,23	0,29	0,12
98,14	99,14	99,31	97,98	97,77	98,09	100,35	99,17	99,72	97,38	98,77	98,19	99,93	99,32	99,59	97,10	97,47	98,21
2,2601	3,0913	1,9381	2,3388	3,1747	2,9486	2,3913	2,6558	3,3902	2,9567	2,4630	2,8402	2,9506	2,3616	2,3971	0,2382	1,4779	13,8500
5,512	5,572	5,606	5,713	5,781	5,536	5,520	5,574	5,594	5,732	5,628	5,670	5,612	5,606	5,549	5,888	5,669	5,879
2,488	2,424	2,394	2,287	2,219	2,464	2,429	2,426	2,359	2,268	2,372	2,284	2,340	2,394	2,415	2,112	2,331	2,121
0,052	0,000	0,077	0,069	0,476	0,191	0,000	0,018	0,000	0,084	0,019	0,000	0,000	0,005	0,000	1,018	0,066	0,500
0,487	0,514	0,496	0,466	0,313	0,425	0,492	0,436	0,449	0,454	0,463	0,504	0,510	0,488	0,488	0,005	0,452	0,005
0,000	0,000	0,000	0,000	0,000	0,000	0,000	0,000	0,000	0,000	0,000	0,000	0,000	0,000	0,000	0,000	0,000	0,000
2,872	2,712	2,516	2,631	2,384	2,670	2,728	2,740	2,748	2,565	2,637	2,564	2,622	2,652	2,787	2,057	2,576	1,634
0,023	0,018	0,018	0,029	0,024	0,027	0,050	0,047	0,026	0,019	0,022	0,023	0,020	0,049	0,044	0,014	0,032	0,011
2,191	2,312	2,372	2,274	2,160	2,290	2,391	2,393	2,402	2,318	2,397	2,439	2,373	2,343	2,319	2,225	2,384	3,360
0,324	0,513	0,615	0,663	0,845	0,429	0,502	0,517	0,555	0,654	0,584	0,605	0,619	0,575	0,482	1,061	0,562	1,193
0,001	0,005	0,005	0,021	0,041	0,041	0,003	0,020	0,008	0,019	0,015	0,011	0,008	0,002	0,000	0,029	0,007	0,030
0,055	0,032	0,026	0,037	0,025	0,021	0,057	0,048	0,022	0,030	0,038	0,029	0,030	0,037	0,041	0,040	0,040	0,036
1,830	1,745	1,715	1,609	1,453	1,684	1,764	1,666	1,803	1,673	1,696	1,747	1,792	1,725	1,780	1,285	1,726	1,302
3,589	3,613	3,596	3,660	3,704	3,634	3,610	3,571	3,609	3,604	3,606	3,597	3,591	3,568	3,611	3,744	3,664	3,868
0,333	0,330	0,317	0,276	0,253	0,310	0,319	0,357	0,338	0,335	0,324	0,339	0,346	0,352	0,318	0,079	0,247	0,128
0,079	0,057	0,088	0,063	0,043	0,056	0,071	0,072	0,053	0,061	0,070	0,064	0,063	0,080	0,071	0,177	0,089	0,005
19,836	19,847	19,840	19,798	19,721	19,779	19,935	19,884	19,967	19,816	19,873	19,875	19,928	19,875	19,906	19,735	19,844	20,070

XY22_18	XY22_19	XY22_20	XY22_21	XY22_22	XY22_23	XY22_24	XY22_25	XY22_30	XY22_31	XY22_32	XY22_33	XY22_34	XY22_35	XY22_36
37,97	37,79	37,32	37,02	37,02	36,6	35,88	36,23	37,21	36,42	36,67	36,79	35,72	36,7	38,71
4,15	3,85	4,1	3,9	4,62	4,46	4,35	4,57	3,81	3,8	3,88	3,91	4,25	4,26	3,98
12,65	13,65	13,94	13,32	13,63	13,6	13,31	13,2	13,87	13,95	13,4	12,98	13,16	13,57	14,55
19,75	19,14	16,76	20,57	19,55	20,93	21,58	21,64	19,84	20,33	20,87	19,51	19,41	19,66	18,9
0,288	0,238	0,124	0,236	0,232	0,252	0,285	0,236	0,112	0,152	0,143	0,164	0,16	0,148	0,135
10,11	10,67	11,82	10,58	10,42	10,27	9,84	9,84	11,06	10,38	10,61	10,05	9,78	10,35	9,74
0,093	0,08	0,058	0,028	0,049	0,02	0	0,01	0,054	0,04	0,032	0,084	0,063	0,054	0,052
0,12	0,076	0,1	0,111	0,116	0,181	0,102	0,166	0,12	0,092	0,072	0,078	0,109	0,057	0,074
0,398	0,485	0,565	0,487	0,462	0,572	0,525	0,458	0,68	0,659	0,662	0,605	0,61	0,679	0,694
0,262	0,3	0,324	0,274	0,292	0,261	0,27	0,244	0,257	0,312	0,31	0,3	0,303	0,308	0,292
1,35	1,29	1,16	1,07	1,07	0,95	0,75	0,85	1,13	0,90	0,97	1,01	0,70	0,98	1,56
3,68	3,67	3,61	3,64	3,66	3,61	3,56	3,63	3,59	3,52	3,54	3,50	3,43	3,51	3,63
99,00	99,95	98,76	100,23	99,86	100,71	99,46	100,13	100,81	99,71	100,49	98,01	96,36	98,87	100,53
0,23	0,27	0,31	0,27	0,26	0,30	0,28	0,25	0,34	0,35	0,35	0,32	0,33	0,36	0,36
98,77	99,68	98,45	99,96	99,60	100,41	99,18	99,88	100,47	99,36	100,14	97,69	96,04	98,52	100,17
1,5191	1,6167	1,7438	1,7774	1,5822	2,1916	1,9444	1,8770	2,6459	2,1122	2,1355	2,0167	2,0132	2,2045	2,3767
5,780	5,697	5,649	5,630	5,614	5,560	5,553	5,563	5,604	5,580	5,592	5,708	5,647	5,632	5,752
2,220	2,303	2,351	2,370	2,386	2,435	2,428	2,389	2,396	2,420	2,408	2,292	2,353	2,368	2,248
0,050	0,122	0,136	0,018	0,051	0,000	0,000	0,000	0,066	0,099	0,000	0,082	0,099	0,086	0,300
0,475	0,436	0,467	0,446	0,527	0,510	0,506	0,528	0,432	0,438	0,445	0,456	0,505	0,492	0,445
0,000	0,000	0,000	0,000	0,000	0,000	0,000	0,000	0,000	0,000	0,000	0,000	0,000	0,000	0,000
2,514	2,413	2,122	2,616	2,480	2,659	2,793	2,779	2,499	2,605	2,662	2,532	2,566	2,523	2,349
0,037	0,030	0,016	0,030	0,030	0,032	0,037	0,031	0,014	0,020	0,018	0,022	0,021	0,019	0,017
2,294	2,398	2,667	2,399	2,356	2,325	2,270	2,252	2,483	2,371	2,412	2,324	2,305	2,368	2,157
0,824	0,784	0,705	0,656	0,654	0,582	0,464	0,522	0,683	0,555	0,596	0,628	0,445	0,605	0,931
0,015	0,013	0,009	0,005	0,008	0,003	0,000	0,002	0,009	0,007	0,005	0,014	0,011	0,009	0,008
0,035	0,022	0,029	0,033	0,034	0,053	0,031	0,049	0,035	0,027	0,021	0,023	0,033	0,017	0,021
1,588	1,675	1,714	1,744	1,691	1,744	1,781	1,774	1,744	1,788	1,815	1,787	1,748	1,683	1,556
3,741	3,692	3,646	3,695	3,703	3,658	3,672	3,714	3,611	3,600	3,601	3,624	3,614	3,590	3,600
0,192	0,231	0,270	0,234	0,222	0,275	0,257	0,222	0,324	0,319	0,319	0,297	0,305	0,330	0,326
0,068	0,077	0,083	0,071	0,075	0,067	0,071	0,064	0,066	0,081	0,080	0,079	0,081	0,080	0,074
19,834	19,895	19,866	19,946	19,830	19,903	19,864	19,888	19,965	19,908	19,975	19,868	19,735	19,802	19,784





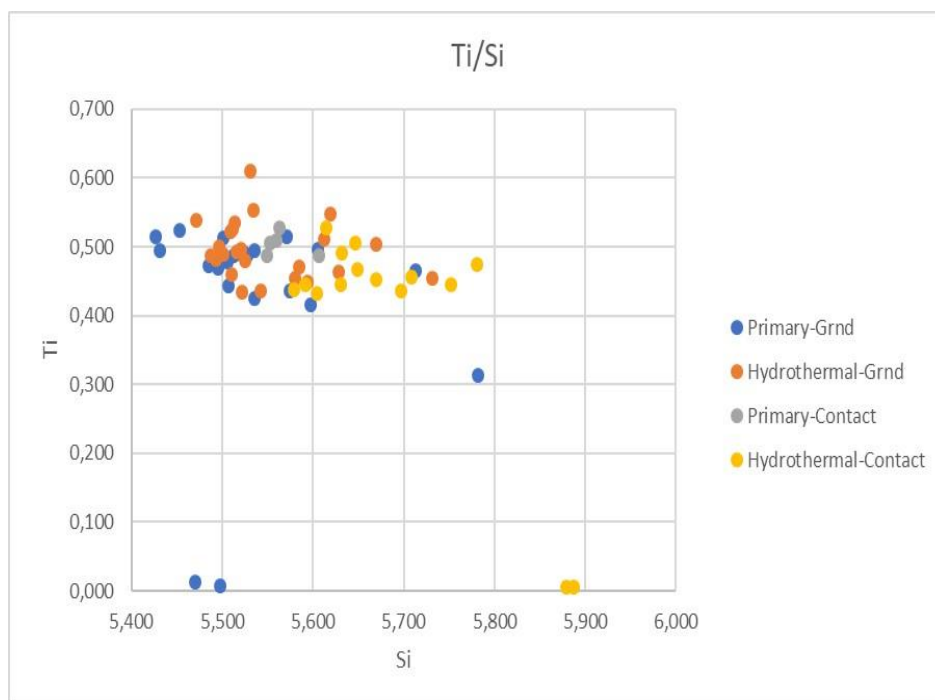


Fig. 26: Correlation diagrams of (a) MgO/FeO_t (b) XMg vs TiO₂ (d) F/Cl vs F (e) F vs Cl (f) XMg/Si and (g) Ti/Si of primary and hydrothermal biotite from Koutalas (Granodiorite) and Ganema area (contact).

Amphibole

Primary amphibole crystals from the outer part of the granodiorite in the Koutalas area, as well as crystals from the contact between the granodiorite and the aplogranite in the Ganema area, were analyzed. The primary amphibole crystals are euhedral, >500 μm large. Like the previous analyses conducted on feldspar and biotite, two points per crystal, one in the core and another in rim were made.

The chemical composition of the analyzed amphibole crystals is reported in Table 4 and the data are plotted in Figures 27 and 28.

All analyzed amphiboles are classified as calcic amphiboles, which means that they present high, >1,5 (Ca,Na) and low, <0,5 Na and (Mg,Fe,Mn,Li) contents. Specifically, the amphiboles from the outer part of the granodiorite (Koutalas) are classified as actinolite because they present the following features: a) Na+K < 0,5; b) Si > 7,5; c) 0,5 < Mg/(Mg+Fe) < 0,9. In this area, all analyzed amphiboles have a core rich in Mg and Ca and poor in Al, Na and K, while Ti and Mn contents remain constant from core

to rim. The opposite trend is observed from rim to core, where the rim seems more enriched in Na, K and Al and poor in Mg and Ca. One specific crystal is classified as actinolite in the core and as anthophyllite, from the Mg-Fe-Mn-Li group, in the rim, due to the decrease of Ca and the increase of Fe.

On the other hand, the amphiboles from the contact between the granodiorite and the aplogranite (Ganema) are classified as magnesio-hornblende because they present the following features: a) $Na+K > 0,5$; b) $6,5 < Si < 7$; and c) $Mg/(Mg/Fe) = 0,491-0,556$. Consequently, these amphiboles have more alkalis (Na+K) and less Si than those from the outer granodiorite. They also have a more Mg-rich core and a Fe and Al-rich rim, while the alkalis as well as Ca, Mn and Ti remain constant from along the core-rim direction (Fig. 27).

It is obvious that there are two different varieties of amphiboles in Serifos, each one related to a different type of rock in a different location. The intrusion of the aplogranite within the granodiorite, as it is revealed in the Ganema area, may have caused the formation of an alkali-rich amphibole along the contact. This event may be connected with the formation of secondary albite, replacing K-feldspar in Koutalas area, so a possible model indicating an alkali-rich hydrothermal fluid moving from the aplogranite in the southeastern part to the granodiorite to the western part should be discussed (Fig. 28).

Table 4: Chemical composition of amphibole from Koutalas and Ganema areas.

Sample	XY9_1	XY9_2	XY9_17	XY9_18	XY22_3	XY22_4	XY22_6	XY22_7	XY22_8	XY22_9	XY22_10
SiO2	54,990	58,450	55,510	51,760	46,740	45,000	44,920	45,460	45,450	45,240	45,330
TiO2	0,000	0,040	0,025	0,356	1,055	1,309	1,479	1,152	1,372	1,174	1,000
Al2O3	1,271	7,500	1,181	3,090	5,820	8,020	8,740	7,450	8,070	8,090	8,110
Fe2O3											
FeO	8,060	4,120	7,170	12,680	18,580	18,680	16,200	16,910	16,580	16,880	17,030
MnO	0,124	0,087	0,148	0,298	0,835	0,672	0,423	0,525	0,426	0,463	0,427
MgO	18,400	12,220	19,070	14,080	10,940	10,120	11,360	11,250	11,480	11,210	11,300
CaO	12,700	8,860	12,810	12,040	10,290	10,690	11,130	10,590	10,820	11,050	11,100
Na2O	0,120	0,309	0,136	0,477	1,390	1,710	1,860	1,570	1,760	1,710	1,630
K2O	0,073	4,040	0,080	0,183	0,572	0,674	0,670	0,543	0,622	0,614	0,606
H2O											
Na2O+K2O	0,193	4,349	0,216	0,660	1,962	2,384	2,530	2,113	2,382	2,324	2,236
Totals	95,738	95,626	96,130	94,964	96,222	96,875	96,782	95,450	96,580	96,431	96,533
Si	7,891	8,181	7,900	7,688	7,136	6,856	6,774	6,952	6,865	6,861	6,868
Ti	0,000	0,004	0,003	0,040	0,121	0,150	0,168	0,133	0,156	0,134	0,114
Al	0,215	1,237	0,198	0,541	1,047	1,440	1,553	1,343	1,437	1,446	1,448
Fe+3	0,000	0,000	0,000	0,000	0,000	0,000	0,000	0,000	0,000	0,000	0,000
Fe+2	0,967	0,482	0,853	1,575	2,372	2,380	2,043	2,163	2,094	2,141	2,158
Mn	0,015	0,010	0,018	0,037	0,108	0,087	0,054	0,068	0,055	0,059	0,055
Mg	3,936	2,550	4,046	3,118	2,490	2,298	2,554	2,565	2,585	2,534	2,552
Ca	1,953	1,329	1,953	1,916	1,683	1,745	1,798	1,735	1,751	1,796	1,802
Na	0,033	0,084	0,038	0,137	0,411	0,505	0,544	0,466	0,515	0,503	0,479
K	0,013	0,721	0,015	0,035	0,111	0,131	0,129	0,106	0,120	0,119	0,117
H	2,000	2,000	2,000	2,000	2,000	2,000	2,000	2,000	2,000	2,000	2,000
Mg/(Mg+Fe)	0,803	0,841	0,826	0,664	0,512	0,491	0,556	0,543	0,552	0,542	0,542
Group	Calcic	Magnesium	Calcic								

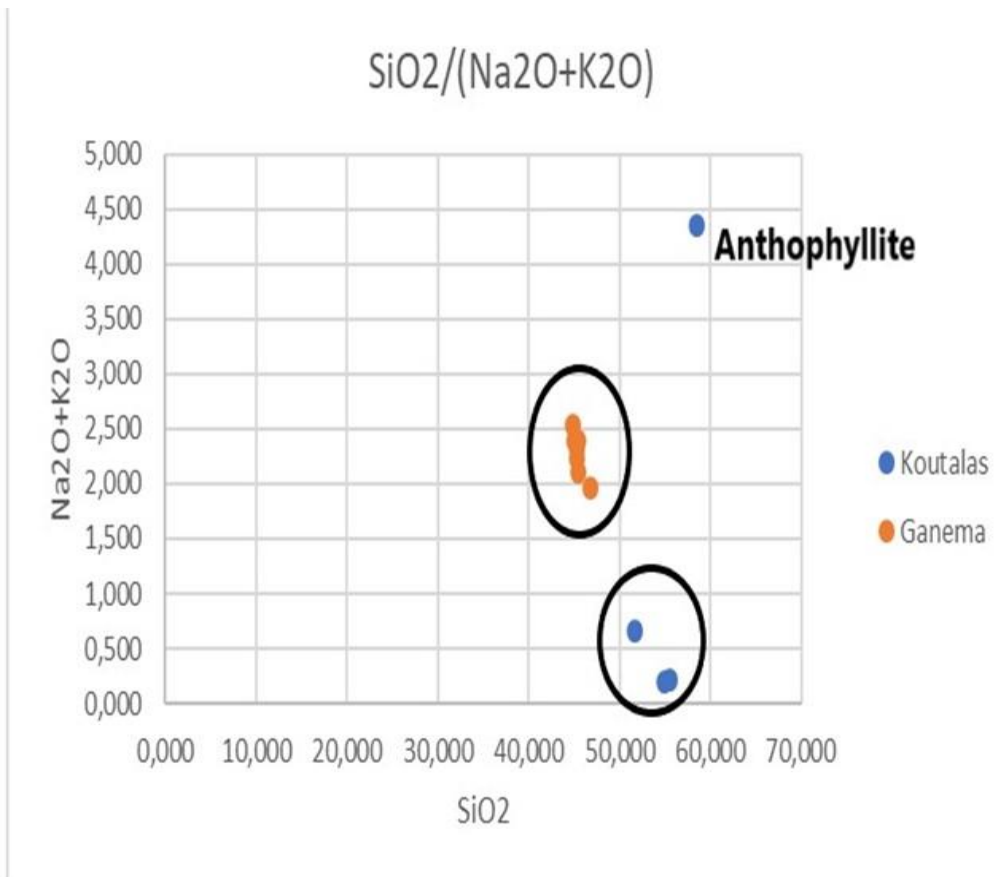


Fig.27: Diagram of SiO₂ vs (Na₂O+K₂O) from the Koutalas and Ganema amphiboles. The one analysis with high concentration of alkalis, corresponds to anthophyllite, forming in the rim of actinolite.

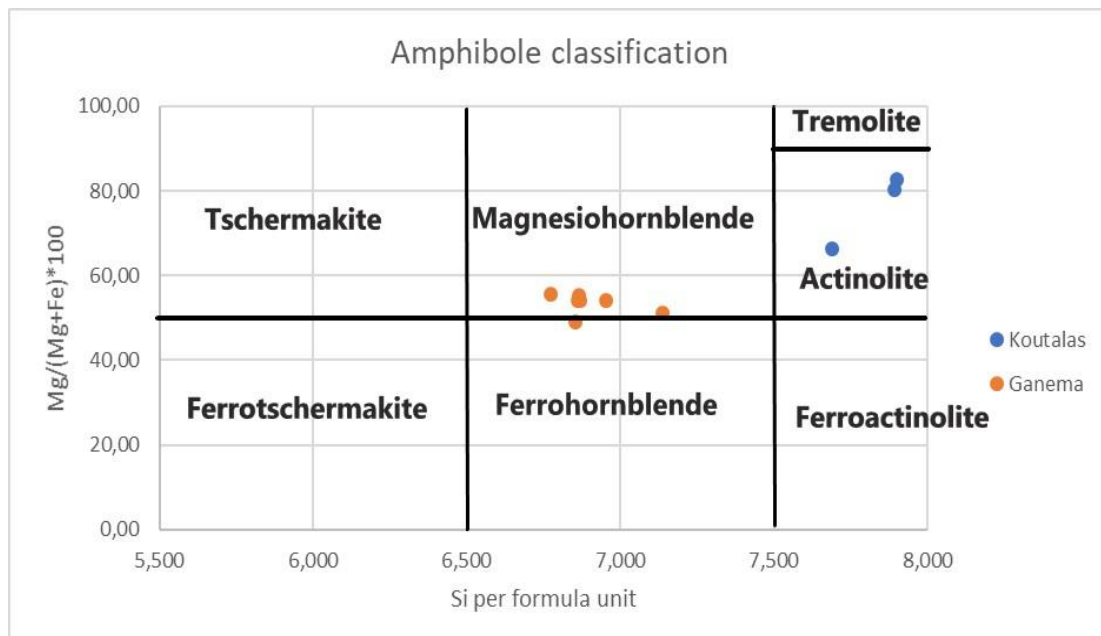


Fig. 28: Amphibole classification diagram. Note the two different types of amphibole detected: actinolite from the outer part of the granodiorite in Koutalas and magnesianhornblende from the contact between the granodiorite and the aplogranite in Ganema

Titanite

Titanite was found in the outer granodiorite in Koutalas and in the granodiorite-aplogranite contact in Ganema and its chemical composition is reported in Table 5.

TiO₂ varies between 31,25 and 35,86 wt %, SiO₂ varies between 29,5 and 30,66 wt %, while CaO content ranges from 26,9 to 28,53 wt %. Al₂O₃ is less than 3,77 wt %, while FeO is between 0,73 and 1,81 wt%. Small amounts (0,02-0,11 wt. %) of alkalis (K₂O > Na₂O), have been also detected. To sum up, MnO and MgO are less than 0,05 wt. %. The F content ranges from 0,98 to 1,80 wt%. No significant differences are observed in the chemical composition of titanite from those two areas

Table 5: Chemical composition of Titanite from Koutalas and Ganema areas

Area	Koutalas	Koutalas	Koutalas	Koutalas	Koutalas	Ganema	Ganema	Ganema	Ganema
Sample	XY_9_24	XY_9_44	XY_9_45	XY_9_46	XY_9_47	XY22_11	XY22_12	XY22_14	XY22_15
SiO ₂	30,420	30,380	30,390	29,500	30,550	30,510	30,450	30,630	30,660
TiO ₂	34,780	34,110	33,810	31,250	33,290	35,860	34,240	33,350	34,180
Al ₂ O ₃	2,680	3,760	3,770	2,480	3,240	1,863	2,960	3,640	3,580
FeO	1,265	0,730	0,832	1,620	1,810	1,160	1,278	1,252	0,889
MnO	0,000	0,000	0,000	0,017	0,030	0,000	0,000	0,000	0,000
MgO	0,000	0,000	0,000	0,000	0,047	0,000	0,000	0,000	0,037
CaO	28,020	28,530	27,370	25,520	26,900	28,140	27,990	28,280	28,260
Na ₂ O	0,000	0,028	0,000	0,000	0,000	0,025	0,044	0,000	0,019
K ₂ O	0,000	0,035	0,077	0,025	0,106	0,026	0,075	0,019	0,000
F	1,480	1,610	1,800	1,240	1,720	0,978	1,510	1,480	1,290
Cl	0,000	0,040	0,000	0,043	0,055	0,026	0,042	0,028	0,000
Li ₂ O*	0,000	0,000	0,000	0,000	0,000	0,000	0,000	0,000	0,000
H ₂ O*	3,359	3,313	3,191	3,193	3,188	3,602	3,329	3,358	3,481
Subtotal	102,004	102,536	101,240	94,888	100,936	102,190	101,918	102,037	102,396
O=F,Cl	0,623	0,687	0,758	0,532	0,737	0,418	0,645	0,629	0,543
Total	101,381	101,849	100,482	94,356	100,200	101,773	101,272	101,408	101,853
F/Cl		40,250		28,837	31,273	37,615	35,952	52,857	
Si	4,492	4,457	4,506	4,665	4,560	4,492	4,502	4,516	4,492
Al iv	0,466	0,650	0,659	0,462	0,570	0,323	0,516	0,633	0,618
Al vi	0,000	0,000	0,000	0,000	0,000	0,000	0,000	0,000	0,000
Ti	3,863	3,764	3,770	3,717	3,737	3,971	3,808	3,698	3,766
Cr	0,000	0,000	0,000	0,000	0,000	0,000	0,000	0,000	0,000
Fe	0,156	0,090	0,103	0,214	0,226	0,143	0,158	0,154	0,109
Mn	0,000	0,000	0,000	0,002	0,004	0,000	0,000	0,000	0,000
Mg	0,000	0,000	0,000	0,000	0,010	0,000	0,000	0,000	0,008
Ca	4,434	4,485	4,348	4,324	4,302	4,440	4,435	4,468	4,436
Na	0,000	0,008	0,000	0,000	0,000	0,007	0,013	0,000	0,005
K	0,000	0,007	0,015	0,005	0,020	0,005	0,014	0,004	0,000
OH*	3,309	3,243	3,156	3,368	3,174	3,538	3,283	3,303	3,402
F	0,691	0,747	0,844	0,620	0,812	0,455	0,706	0,690	0,598
Cl	0,000	0,010	0,000	0,012	0,014	0,006	0,011	0,007	0,000
TOTAL	17,412	17,461	17,401	17,390	17,429	17,381	17,445	17,472	17,435
Y total	4,019	3,853	3,873	3,933	3,977	4,114	3,966	3,852	3,883
X total	4,434	4,500	4,363	4,329	4,322	4,452	4,461	4,471	4,442
Al total	0,466	0,650	0,659	0,462	0,570	0,323	0,516	0,633	0,618
Mn/Mn+Fe	0,000	0,000	0,000	0,011	0,017	0,000	0,000	0,000	0,000
Mg-Li	0,000	0,000	0,000	0,000	0,010	0,000	0,000	0,000	0,008
Ti/Fe									
Luhr et al.	-35,373	-20,447	-23,600	-51,370	-54,045	-31,309	-36,342	-36,562	-24,985

V.6. Cold Cathodoluminescence (CL)

Cold cathodoluminescence petrography was used for characterization and discrimination of the main alteration styles, affecting the granodiorite and the aplite. The results have shown the following:

In the Koutalas area, where only the granodiorite is present, there is a widely extended sodic alteration, where most of the K-feldspar and some calcic plagioclase crystals have been replaced by secondary albite. In the CL images, the K-feldspar has a light blue color, the primary basic plagioclase has a light green color and the secondary albite has a brownish-yellow color. Very few K-feldspar crystals remain unaltered in this area, while the albitization occurs mainly from the center to the rim as previously mentioned (Fig. 29). The hydrothermal quartz presents a deep blue-violet color compared to the light blue primary quartz.

In the Sotiras area, where only the aplite is present, the rock-forming minerals look fresh (Fig. 30). Clearly, the proportion of K-feldspar in this area is higher than the one in Koutalas, which is an indicator of the different composition of the aplite generally. The fresh K-feldspar and plagioclase have oscillatory zoning of primary origin, which is shown very clearly in the CL images (Fig. 31). Specifically, light blue K-feldspar occurs in the center of each crystal with dark blue-purple K-feldspar in the margins. For the K-feldspar, the center of the analyzed crystals corresponds to a more albite-rich composition named as Zone 1 ($Ab > 10\%$), going to an albite-poor Zone 2 ($Ab < 10\%$) and returns to the first albite-rich composition in the rim named as Zone 3. For the plagioclase, the center is dominated by a light green colour, while the margin is dominated by dark green colour (Fig. 32). The origin of these zonation is not studied here. In the Sotiras area, similarly to Koutalas (see above) primary quartz crystals have a lighter blue color compared to the hydrothermal vein-type quartz, whose color is darker blue.

In the Ganema area the aplite intrudes the granodiorite. The CL image of a sample taken from this area, shows the aplite in the center showing no sodic alteration and unaltered K-feldspars and plagioclase crystals, surrounded by the altered granodiorite in which most of K-feldspar and plagioclase have been replaced or partly replaced by secondary albite (Fig. 33). This image helps us understand that the emplacement of the aplite into the granodiorite must have succeeded the sodic alteration in the granodiorite, otherwise the aplite must have been affected too.

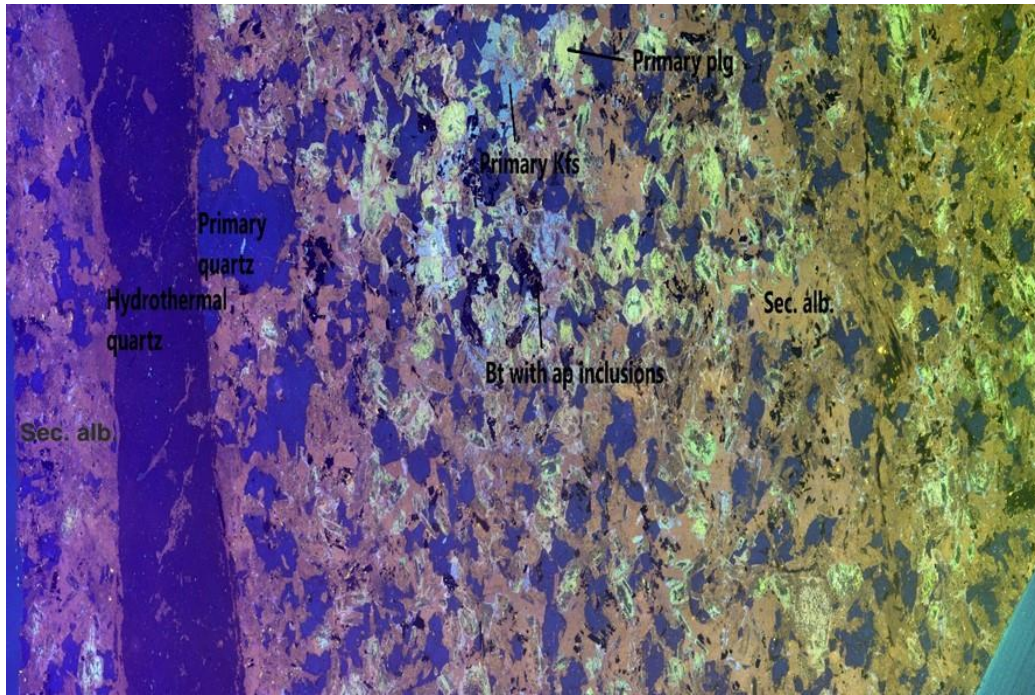


Fig.29: CL image of the sodic-altered granodiorite. Brownish secondary albite is widely extended in the whole image, having replaced primary plagioclase and primary K-feldspars with light green and light blue colour respectively. The hydrothermal quartz vein in the left side of the image has a darker blue colour than the primary quartz.



Fig.30: CL image of the unaltered aplogranite from Sotiras area. Both the plagioclase and the K-feldspar are fresh showing oscillatory zoning (see following figure).

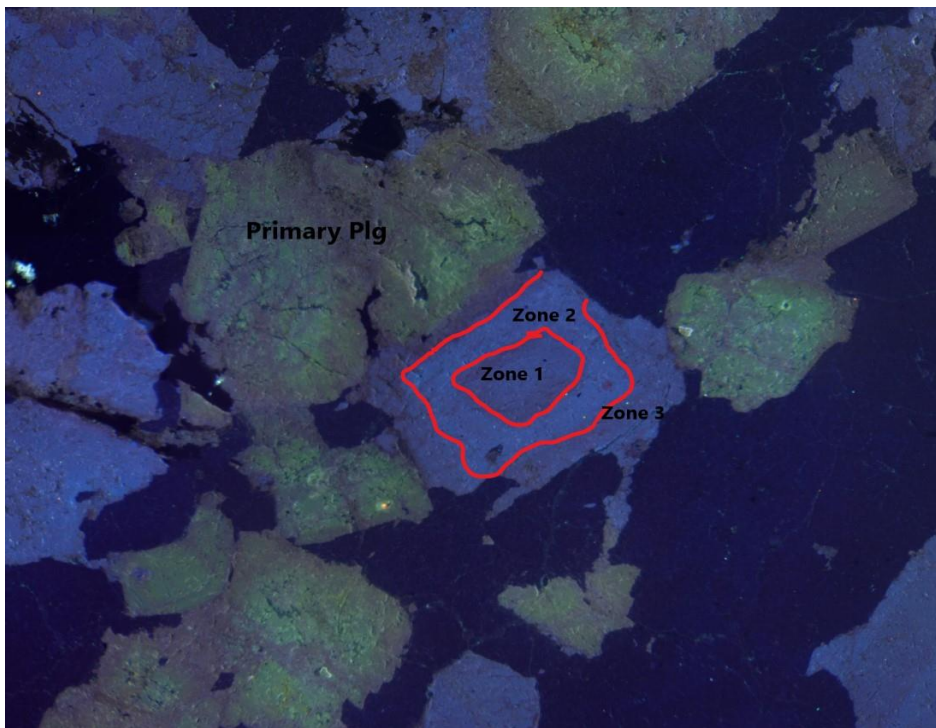
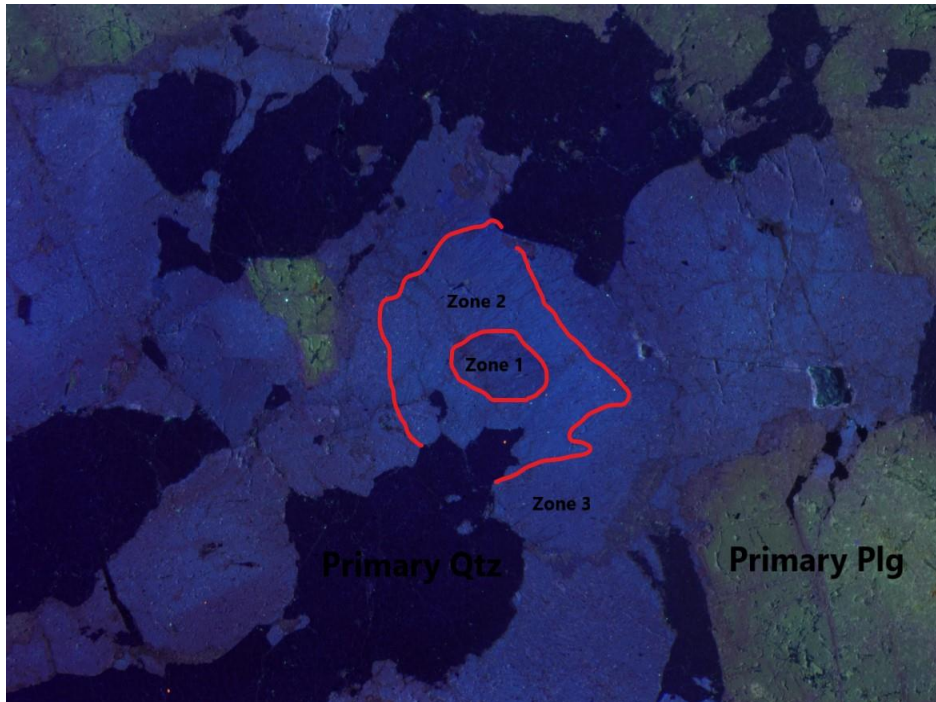


Fig.31: Magnification of the previous CL image (aplogranite sample, red squares). Three distinctive zones within one K-feldspar crystal, with different CL colours. Zone 1 and zone 2 have the same dark blue colour, while zone 2 has a lighter blue, maybe due to the differentiation of the chemical composition during the crystal growth.

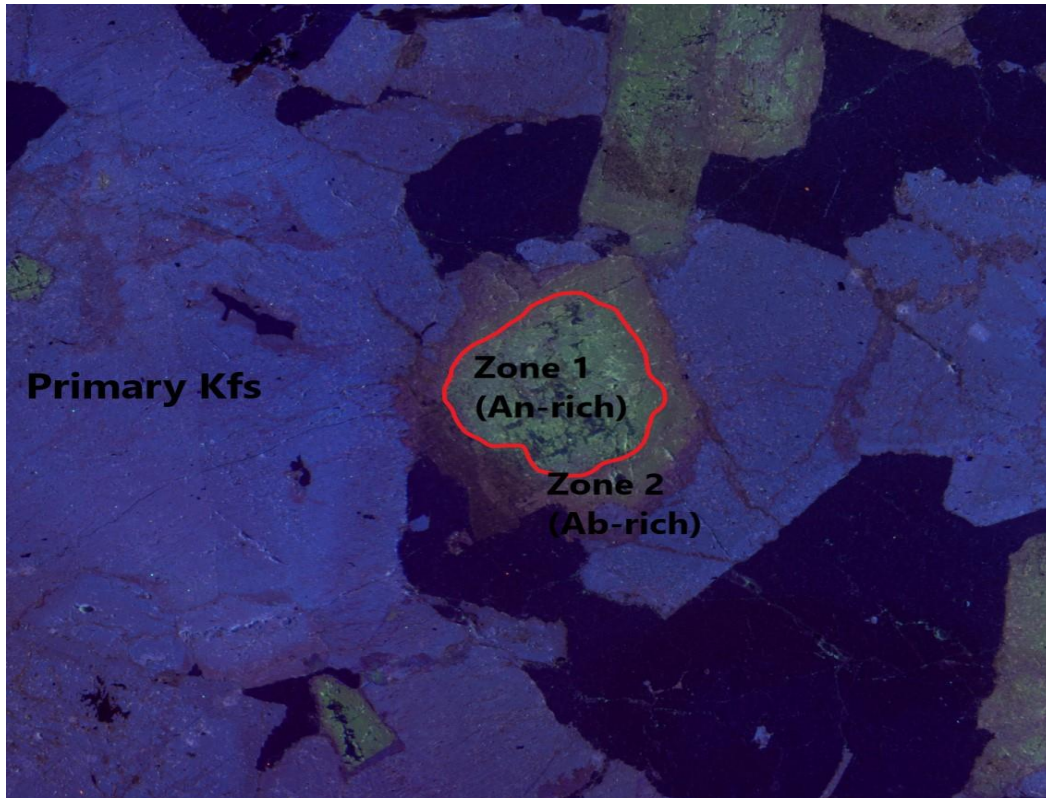


Fig.32: Magnification of the previous CL image (aplogranite sample, black square). A fresh plagioclase crystal with an anorthite-rich core (light green colour), going to a more albite-rich margin (brown-colour). No albitization is observed here, like in Koutalas area where the alteration was more intense in the center of the crystals.

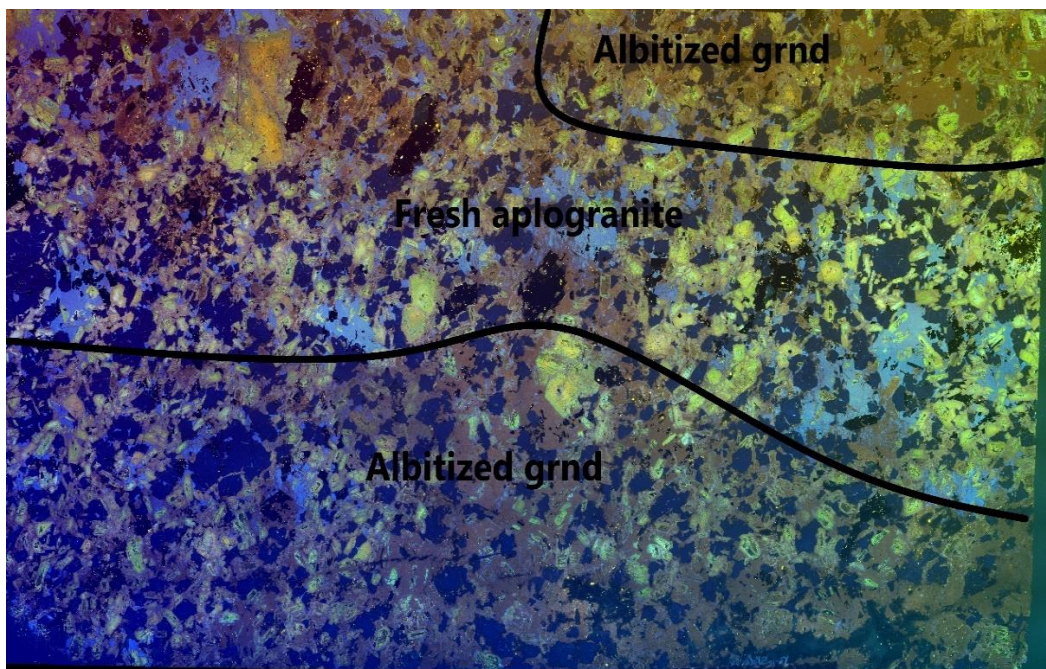
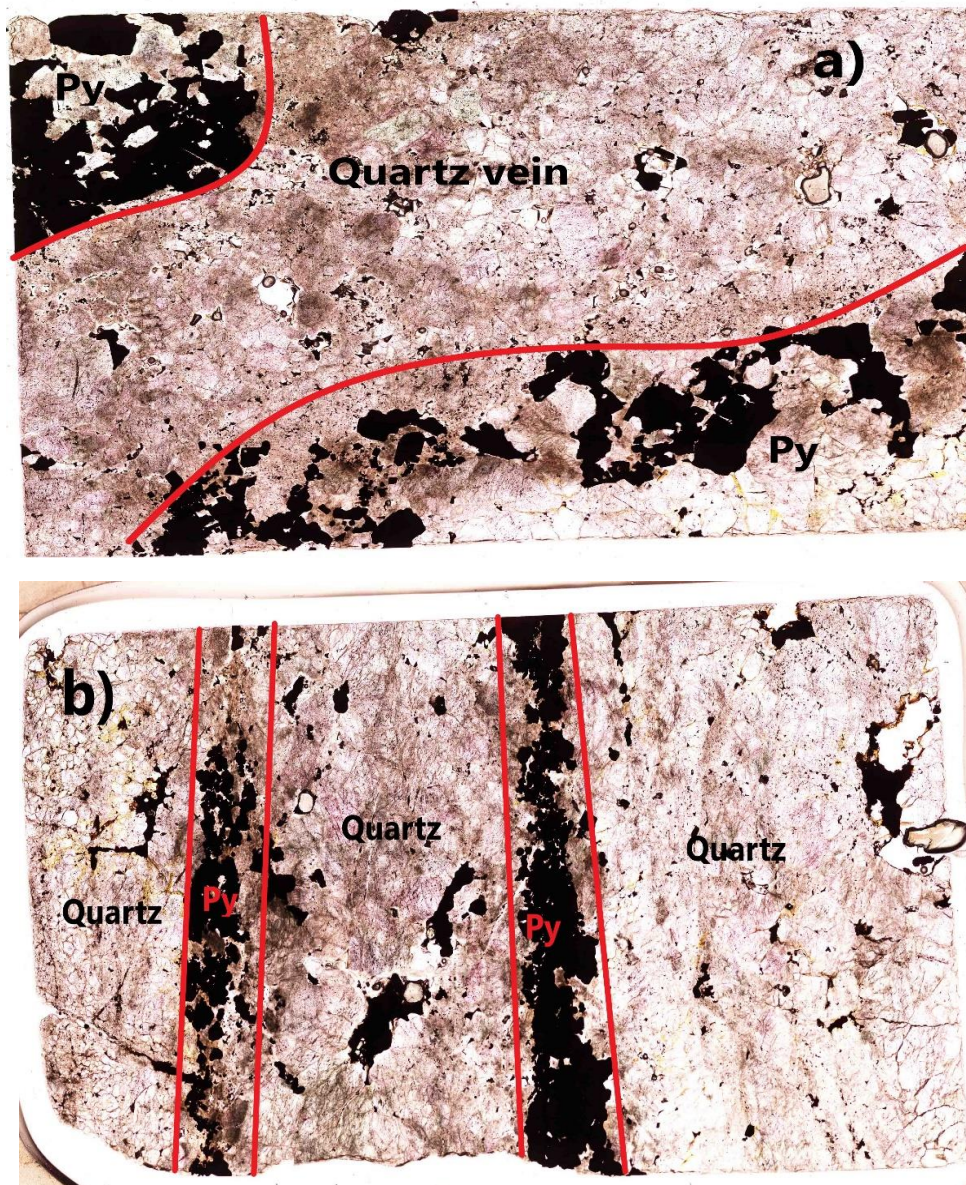


Fig.33: CL image from the intrusion of the aplogranite into the granodiorite in Ganema area. The aplogranite seems unaltered, while the granodiorite is widely altered. As a result, the alteration of the granodiorite must have been succeeded by the intrusion of the aplogranite.

V.7. Fluid inclusion analysis

Fluid inclusion petrography

Fluid inclusion analysis was conducted on quartz from both the sheeted veins within the granodiorite in the Koutalas area and the aplogranite-hosted quartz veins in the Sotiras area. Scans in transmitted light of double polished sections used for the microthermometric measurements are presented in Figure 34.



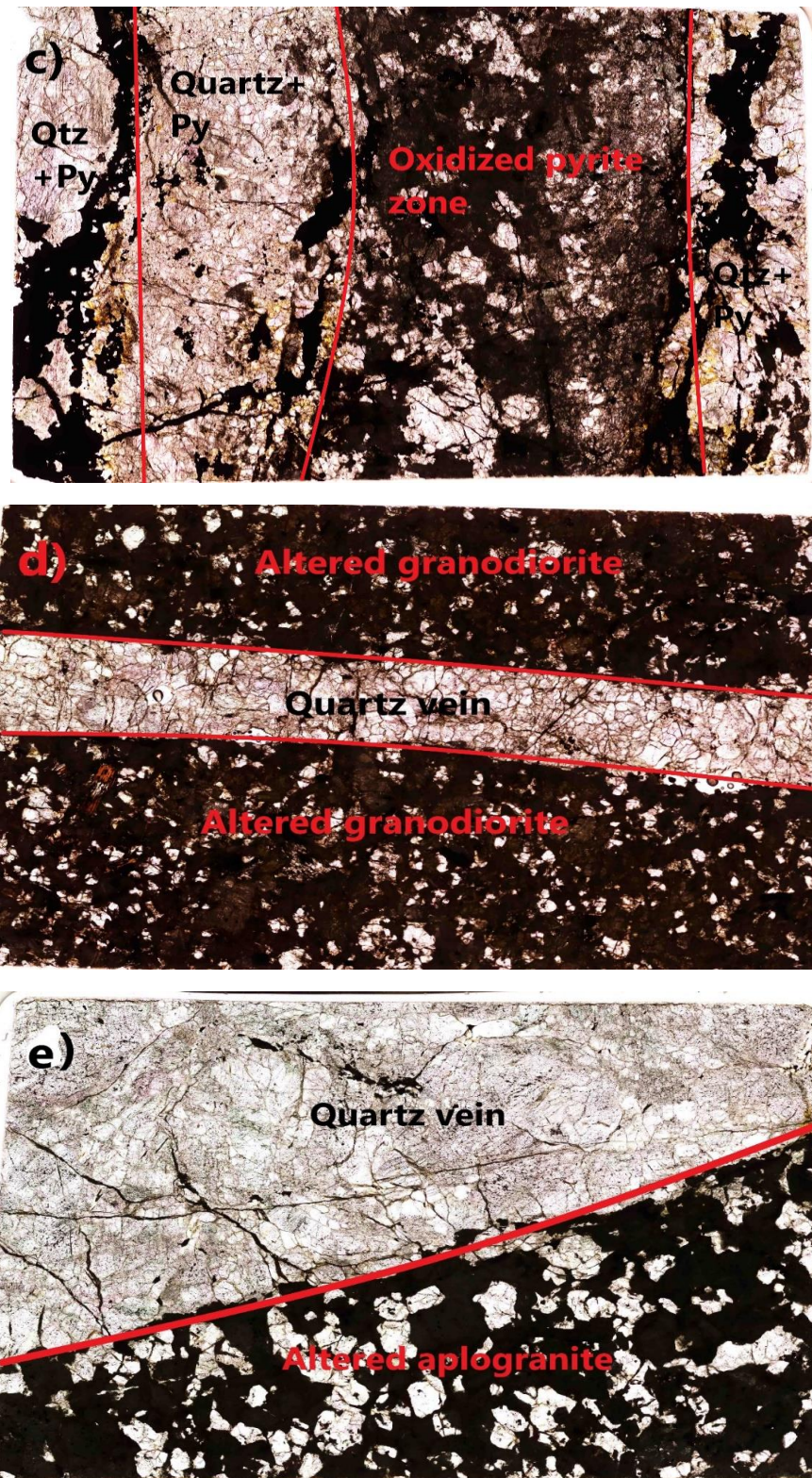
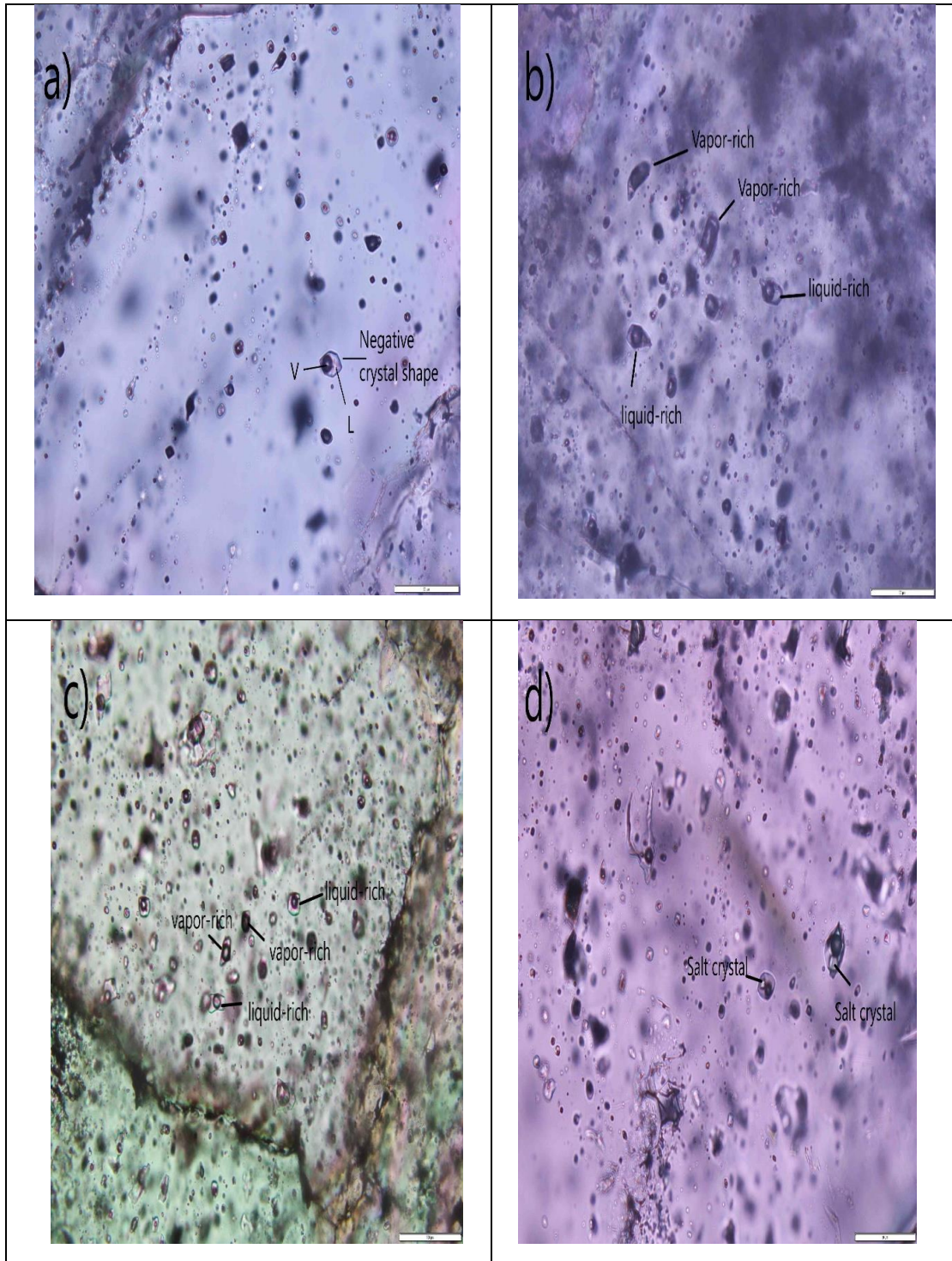


Fig. 34: Transmitted light scans of doubled polished sections used for fluid inclusion study: a-c) Samples from sheeted veins at Koutalas. Pyrite occurs mainly as distinct zones within the quartz vein either fresh (a, b) or oxidized (c); d) Quartz vein with no sulfides present from the granodiorite in the Koutalas area (not analyzed in this study). The granodiorite is intensely albitized; e) Quartz vein crosscutting the aplogranite from the Sotiras area. The aplogranite is partly altered, with secondary sericite partly replacing K-feldspar.

The main goal of the fluid inclusion analysis during this study is to find out under which P-T-X conditions the ore minerals inside the granodiorite and aplogranite have precipitated. Such information would be useful to establish the potential genetic relationship between granitoid-hosted mineralization and the main skarn deposit in the western part of the island. On the other hand, fluid inclusion analysis from the aplogranite might be a useful tool to compare all mineralization styles hosted in the igneous rocks.

As it is previously mentioned, a quartz ore-bearing sheeted-vein system occurs in the Koutalas area. In order to figure out the temperature and the pressure under which the ore minerals have been precipitated, as well as the composition of the hydrothermal fluid responsible for this mineralization, a fluid inclusion analysis of the quartz from the veins was conducted. Following the criteria of Roedder (1984), most of the inclusions analyzed are primary, as they occur in distinct growth zones within the crystal, while some of them occur isolated (Fig. 35). Furthermore, some assemblages comprise pseudosecondary inclusions, as they have been formed between two distinct growth zones within the crystal. Fluid inclusions are irregularly shaped, negative crystal shaped (Fig. 35a) or elongated (Fig. 35g,h). Their size varies between 7 and 55 μm . Two main groups can be distinguished. The first group consist of liquid-rich fluid inclusions with L/V ratio 5/2 or 4/1. Some of these fluid inclusions contain one salt crystal with the same 5/2 or 4/1, L/V ratio (Fig. 35d,e). The second and less frequent group consists of vapor-rich inclusions with L/V ratio 2/4 or even 1/4. Usually, group 1 and group 2 inclusions are found in the same assemblage, which is an indication for phase separation (Fig. 35b, c, e).



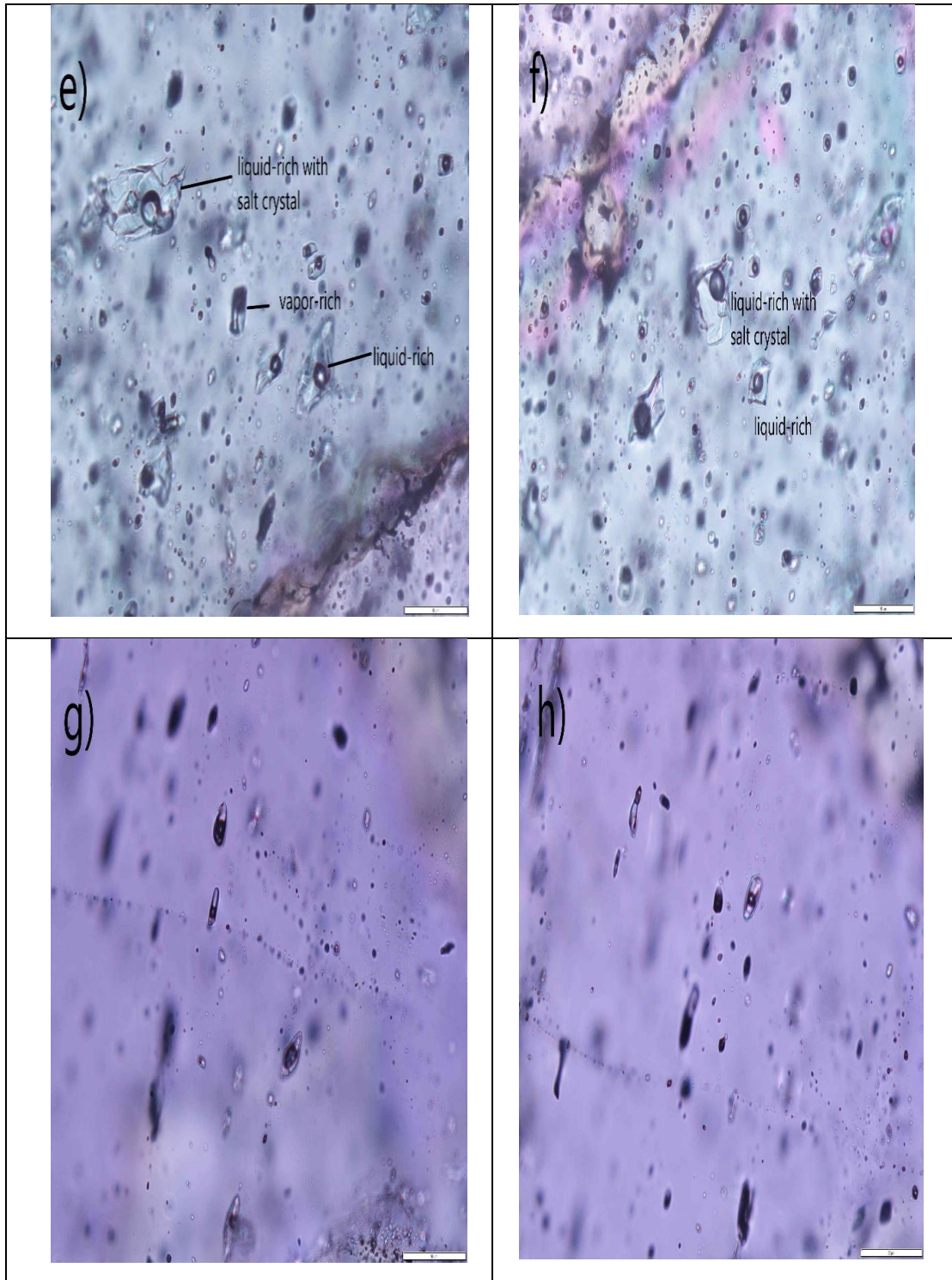
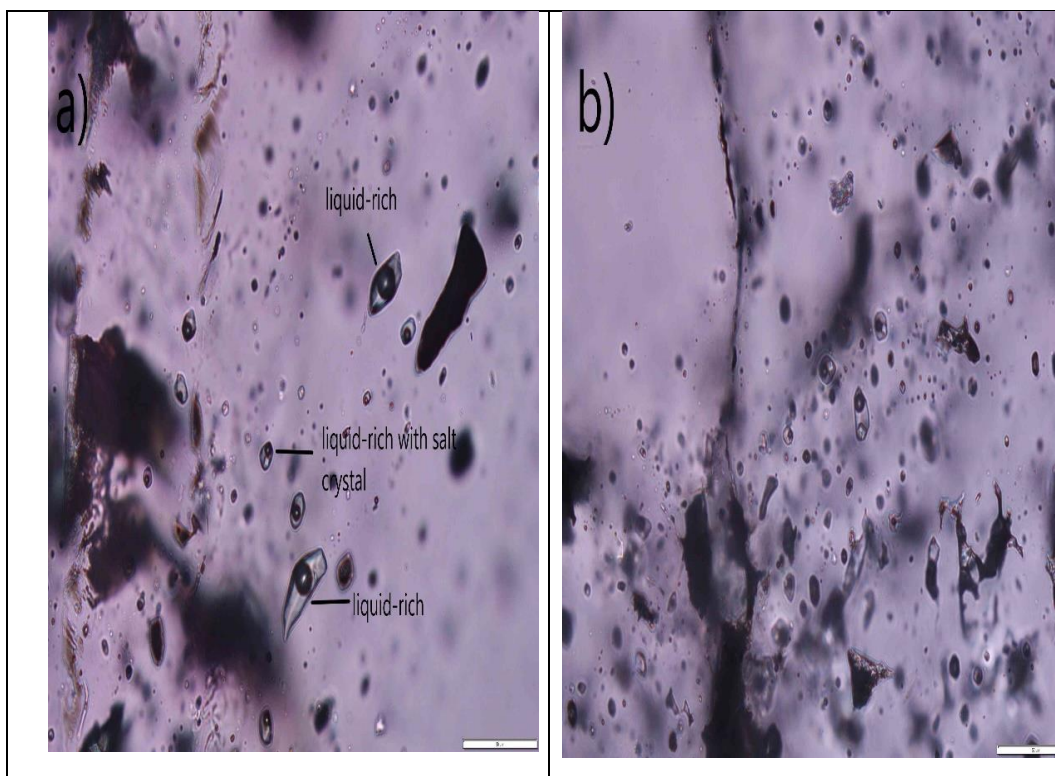
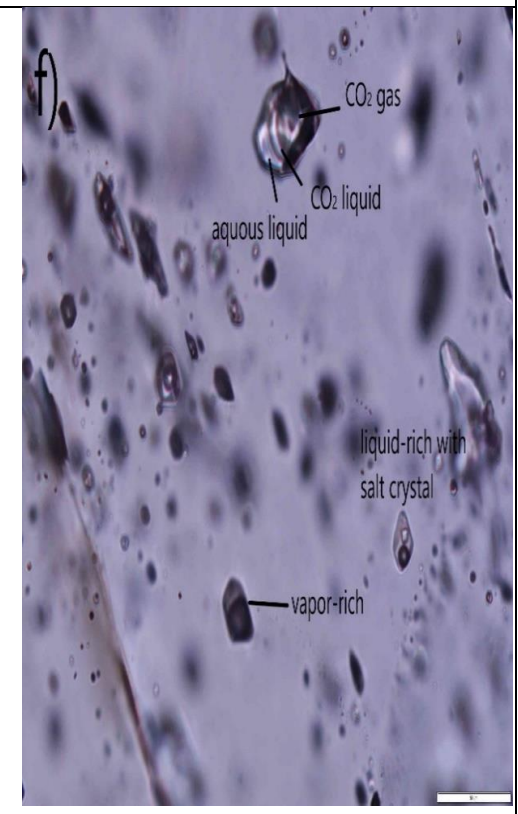
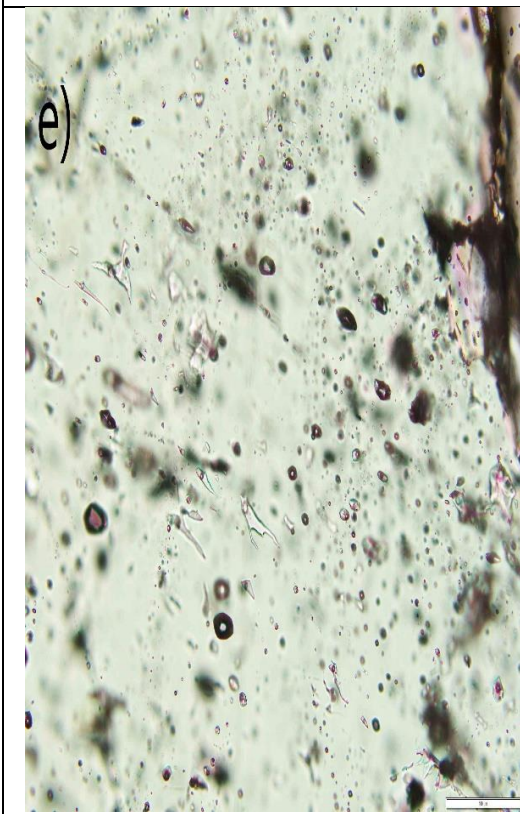
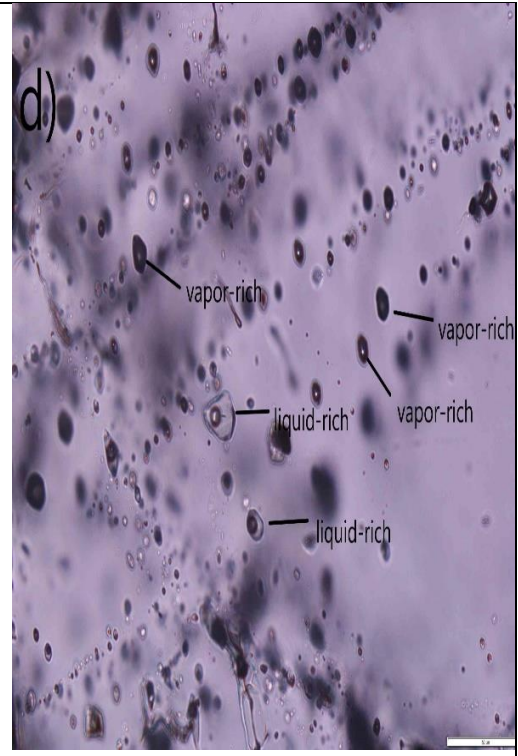
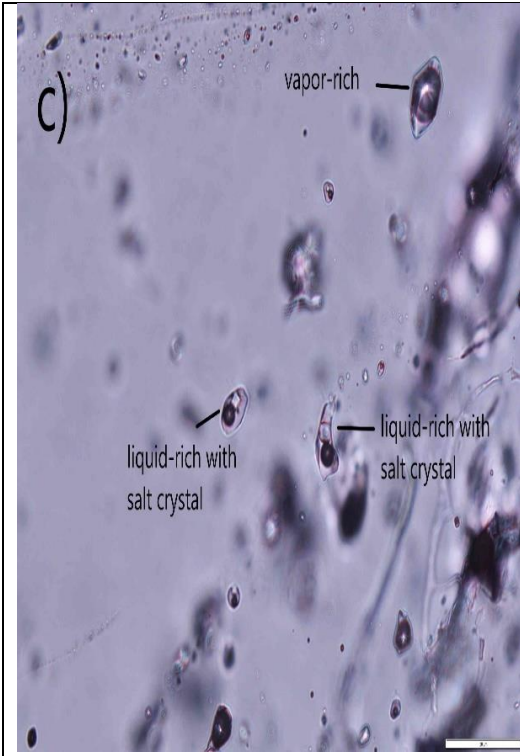


Fig. 35: Microphotographs of fluid inclusions from the sheeted veins system in Koutalas. a) Negative crystal shaped liquid-rich inclusions; b,c) Liquid-rich and vapor-rich inclusions as an indicator of boiling; d,f) Liquid-rich and liquid-rich with salt crystal inclusions; e) Coexistence of the two groups, indicating boiling process; g,h) Droplet-shaped pseudo-secondary fluid inclusions.

At Sotiras, large quartz veins occur, in addition to the disseminated-type mineralization hosted within the aplongranite (and the miarolitic cavities). The fluid inclusion petrography from these veins gave similar results as in the granodiorite (Fig. 36a, c). The fluid inclusion shape varies from elongated (Fig. 36e), droplet-like to rounded, irregular and negative crystal shape. Moreover, their size varies from <10 to $40\text{--}45\ \mu\text{m}$. The three groups, described in the granodiorite occur in the aplongranite too with very similar L/V ratios, except from the vapor-rich group where the L/V ratio is less than 0.25 (Fig. 36). In one sample, a double-bubble CO_2 rich inclusion consisting of water liquid, liquid CO_2 and gas CO_2 (Fig. 36f), occurs into the same assemblage with a liquid-rich, vapor-rich and hypersaline FI (Fig. 36f). In the same sample but in another assemblage, two liquid-rich inclusions with two daughter minerals (with greenish and blueish colors) occur along with liquid-rich and vapor-rich inclusions (Fig. 36g, h). As these two types of inclusions were found only in the aplongranite, this could be an indication of a different composition of the hydrothermal fluid and/or of different precipitating conditions for the quartz veins between the granodiorite and the aplongranite.





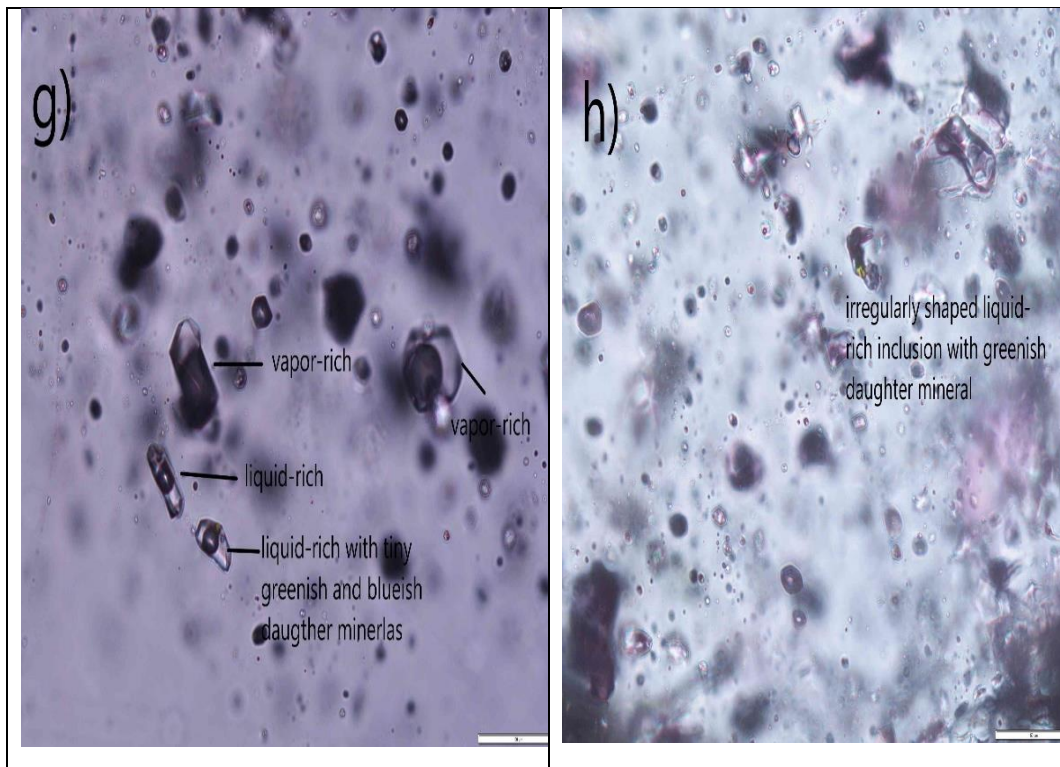


Fig. 36: Microphotographs of fluid inclusions from aplogranite-hosted quartz veins in the Sotiras area: a) Coexistence of liquid-rich inclusions along with liquid-rich with a salt crystal; b) Liquid-rich with a salt crystal inclusions; c) Coexistence of liquid-rich with a salt crystal with vapor-rich inclusions; d) Liquid-rich along with vapor-rich inclusions, indicating boiling processes; e) Elongated pseudosecondary vapor-rich inclusions; f) Double-bubbled CO₂ inclusion in coexistence with liquid-rich with salt crystal and vapor-rich inclusions; g,h) Liquid-rich with undefined greenish and blueish daughter minerals (maybe FeCl₂ crystals) in coexistence with boiling assemblage liquid-rich and vapor-rich inclusions.

Fluid inclusion microthermometry

Microthermometric analysis was conducted to fluid inclusion assemblages from both the quartz sheeted veins in the granodiorite and the aplogranite-hosted quartz veins. The assemblages analyzed here consists of 3-7 fluid inclusions. The fluid inclusions are primary located either as individual assemblages or as concentrations in distinct growth zones within the crystal. The analyzed inclusions belong to both groups described above, including group 1 for liquid-rich inclusions and group 2 for vapor-rich fluid inclusions. The vast majority of them, homogenized into a liquid phase. Since the main goal of this study is to determine the conditions under which the ore minerals have been precipitated and, if possible, the chemical composition of the hydrothermal fluid responsible for the precipitation, the homogenization temperature (T_h) along with the temperature of the final melting of ice ($T_{m,ice}$) were measured. For the inclusions containing one salt crystal, the temperature of the final melting of the salt crystal ($T_{diss.}$)

instead of $T_{m,ice}$ was measured in order to estimate the fluid salinity. Microthermometric results are reported in Table 6 and data are plotted in Figures 36-39.

Microthermometric data from the sheeted quartz veins at Koutalas, reveal a wide range of the homogenization temperatures, in the range from 168° to 550 °C. Most of the inclusions homogenized between 300° and 450 °C, where the highest frequency corresponds to a 350 °C temperature. The inclusions present a wide range $T_{m,ice}$ between -3,7° to -19,1 °C. T_{diss} of salt-saturated at room temperature inclusions (brines) varies between 114° and 397°C. Estimated salinities range between 6,0 and 47,1 wt% NaCl equiv.

The fluid inclusion measurements from the aplogranite-hosted quartz veins, present similar results. The range of homogenization temperatures is from 255° to 483°C. In this range of temperature, two subgroups can be distinguished. The first one corresponds to low to intermediate salinity (7,17-10,49 wt% NaCl equiv.) vapor-rich inclusions showing $T_{m,ice}$ between -4,5 to -7 °C. The second one corresponds to high salinity (18,96-41,49 wt% NaCl equiv.) inclusions showing $T_{m,ice}$ from -15,4 to -20 °C (for salinity < 22,38 wt% NaCl equiv.) and T_{diss} . from 217,5 to 340,2°C for higher salinity values. Inclusions with double-bubble CO₂ along with undefined greenish and blueish daughter minerals are found in coexistence with both liquid-rich and vapor-rich inclusions in a typical boiling assemblage. Since those two types of inclusions have not found in the granodiorite-hosted sheeted vein system, it may be a significant difference in the hydrothermal fluid composition between these two areas. It is also clear, that the inclusions from the aplogranite indicate lower temperature for the formation of the hydrothermal quartz, less than 550°C.

Table 6: Homogenization, melting of ice and halite dissolution temperatures along with estimated salinities of quartz from both granodiorite-hosted sheeted quartz veins (samples XY1, XY2 and XY4) and aplogranite-hosted quartz veins (XY16, XY19).

Sample	Chip	Assemblage	Fluid inclusion	Tmice (°C)	Th (°C)	Tdiss. (°C)	Salinity (%)
XY1	1	1	1	-7,6	550		11,22
			2	-7,2	200		10,73
			3	-5,5	550		8,55
			4		480,1	232,2	33,6
	2	1	1		378	200	31,87
			2		336,2	243	34,25
		2	1		536,2	397,1	47,12
			2		310,2	301,4	38,24
		3		537	345	41,94	
		4		313,6	309,1	38,87	
XY2	1	1	1	-14,5	407,5		18,22
			2	-17,6	379,1		20,67
			3	-15,1	390		18,72
			4	-7,9	440,2	305	38,55
	4	1	1	-19,1	410,2		21,75
			2	-18,6	398,1		21,4
			3	-16,5	426,2		19,84
	5	1	1		550	199,5	31,82
			2		383,7	242,7	34,19
			3		326,8	206,7	32,18
XY4	1	3				173,5	30,61
		4				183,6	31,06
	2	1	1		335,3		31,06
			2		317,5	289	37,33
	2	1	1	-8,6	459,6		12,39
			2	-3,7	361,1		6,01
			3	-4,4	456,9		7,02
			4	-8,4	371,6		12,16
			5	-12,7	480,7		16,62
			6		168,4	114,2	28,4
			7		317,9	238,7	33,95
	2	1	1	-5,4			8,41
			2	-5,2	429,1		8,14
			3	-4,8	442,5		7,59
4				320,1	187,2	31,24	
5				328,5	138,6	29,21	
5	1	1		319,7	200,4	31,87	
		2		280,2	203,1	32,02	
		3		296,2	216,4	32,7	
		4		296,2	216,4	32,7	
XY16	3	1	1	-6,5	280		9,86
			2	-17,1	255		20,3
			3		329,6	340,2	41,49
			4		284,3	337,8	41,22
XY19	1	2	1	-20	318,5		22,38
			2	-7	372,1		10,49
			3		328,4	204,8	32,08
			4		348,2	207,3	32,23
			5		292	210,5	32,39
	3	3	1		331,1	236,9	33,88
			2		308,5	250,5	34,71
			3		323,1	263,3	35,52
	4	1	1	-17,4	313,4		20,52
			2	-4,5	482,5		7,17
3			-15,4	336,2		18,96	
4				465,4	217,5	32,78	
5	1	1		334,5	241,2	34,13	
		2		335,3	231,4	33,55	
		3		332,5	258,5	35,22	
		4		296	302,5	38,36	

The fluid inclusions measured, from both the granodiorite and the aplogranite, have given temperatures between 200° and 550 °C, and most of them homogenized with a T_h peak at 350 °C. Less than 10 inclusions, found only in the granodiorite gave temperatures below 250°C and they might relate with late meteoric or meteoric-magmatic mixed fluids. It is worth mentioning that in those low-temperature inclusions, the halite crystal, if present, does not appear again after passing the halite dissolution temperature. This phenomenon may be an indicator for metastable salt phases in the late stage of the hydrothermal system.

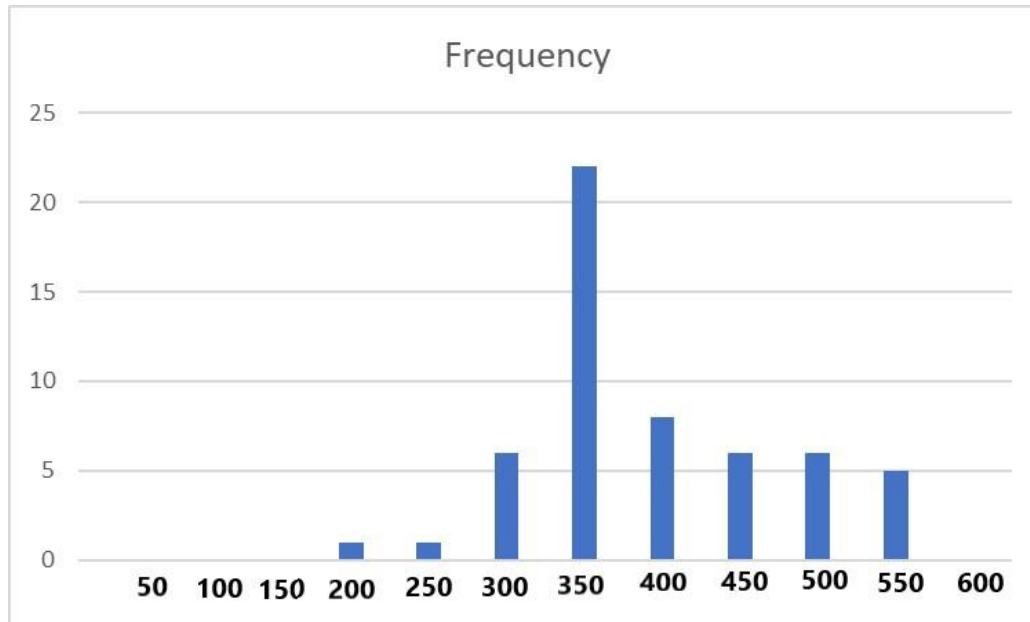


Fig.36: Frequency diagram of the homogenization temperatures measured. Note that most of fluid inclusions homogenized between 300° and 550 °C, with a T_h peak at 350°C.

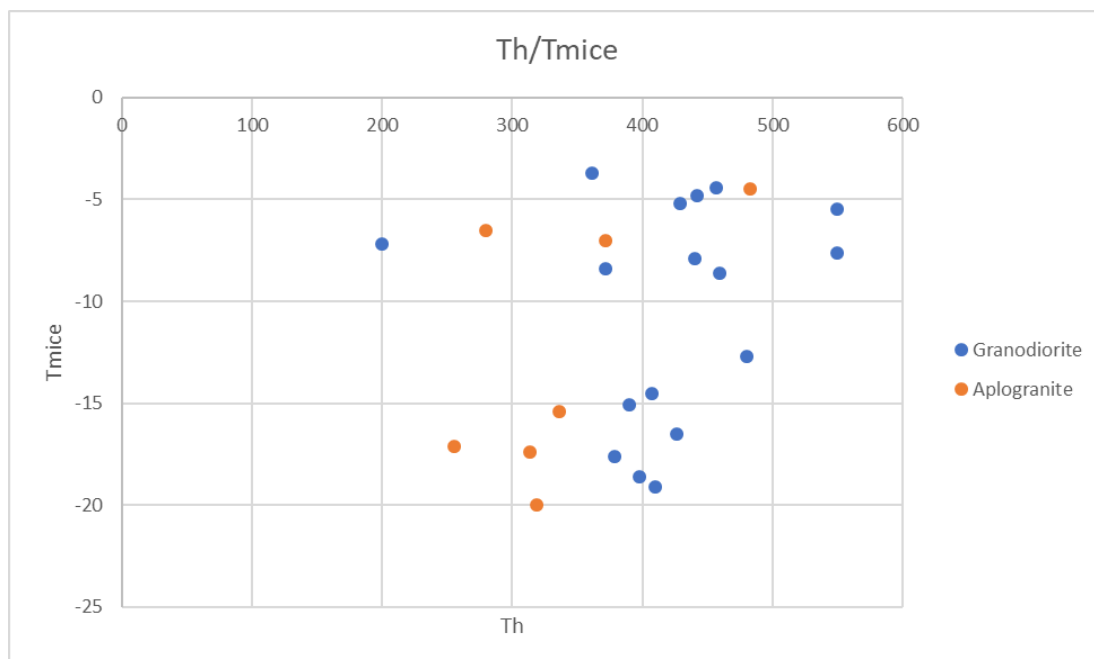


Fig.37: Diagram of measured T_h vs $T_{m,ice}$ for the vapor-rich inclusions and the liquid-rich

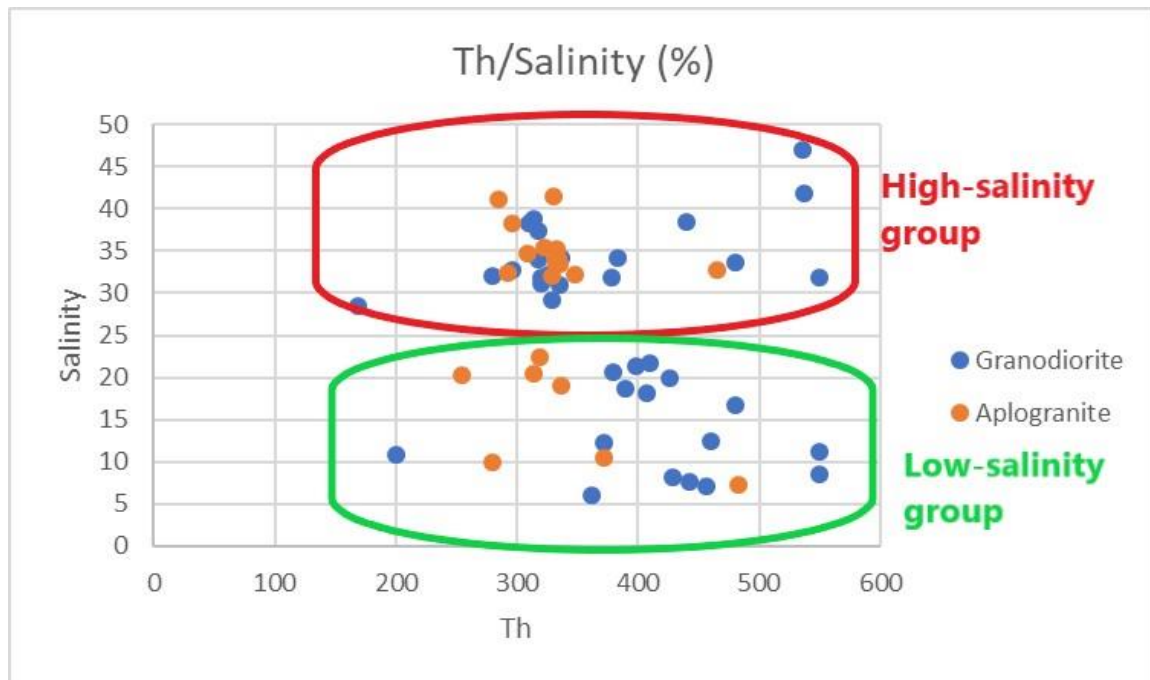


Fig. 39: T_h vs Salinity diagram of the mean values of each fluid inclusion assemblage measured. Two main groups can be distinguished

VI. Discussion

Several studies have testified the relationship between skarn deposits and granite-related porphyry-type deposits (e.g., Sillitoe 2010). This is the first study demonstrating abundant sulfide mineralization within the Serifos granitoids that share some similarities with both porphyry and reduced intrusion-related gold systems, as the later are characterized by aqueous-carbonic fluids as those found in the aplogranite.

In the Koutalas area, and above the system of granodiorite-hosted mineralized sheeted veins, the marbles contain skarn and carbonate-replacement mineralization, similar to that in the western part of the island (e.g., Megalo Livadi and Koundouro), which represent the major Fe ore deposits on Serifos. This suggest that sheeted veins may represent feeders to the skarn-forming fluids that might have migrated both upwards and westwards resulting in the formation of the skarn deposits. This scenario is also supported by microthermometric data from Salemink (1985), which indicate a 260-300 °C range of temperature and high-salinities (>35%) for the hydrothermal fluids responsible for the skarn ore deposition. These results overlap with those obtained from this study, especially the ones from the main ore-deposit stage (temperatures from 250-450°C).

The sheeted veins along with the extended sodic-calcic alteration in the area, although common in the so-called reduced intrusion related systems (Figs. 3 and 40), may characterize the deep part of a porphyry-type system at Serifos as mentioned by Seedorff et al. (2005, 2008). According to the model of Seedorf et al. (2005, 2008), higher levels of such systems are characterized by the presence of quartz stockwork-

type mineralization which was not found in the study area. One possible explanation of this absence is the erosion of the shallowest parts of the system including the quartz stockwork system. Alternatively, this system may be in a higher altitude and therefore has not been discovered yet. The third but less possible scenario is that the sulfide stockwork system in the central part of the granodiorite might be related with the shallower part of the whole porphyry system, although no quartz veins were found there.

It is previously mentioned that, the sheeted vein system could represent possible feeder zone for the ascending magmatic aqueous fluids responsible for the deposition of the ore minerals within the marbles of the CBU. The skarn is distinguished into two different stages, one prograde stage where hedenbergite, ilvaite and garnet (andradite) with minor amounts of wollastonite and vesuvianite occur, and one retrograde stage, where secondary magnetite, epidote, calcite, hematite, barite and quartz occur (Ducoux et al., 2017). The retrograde stage corresponds to lower temperature and is related to the main Fe deposit at Serifos (Salemink (1985). According to Korosidis (2019; unpublished Master thesis) the retrograde stage at Megalo Livadi and Koundouro, is characterized by oxides in association with scheelite, as well as sulfides (pyrite, chalcopyrite, arsenopyrite), native elements (native gold and native bismuth) and various Bi-sulfosalts.

This study demonstrates that the sheeted quartz veins at Koutalas include a similar ore mineralogy with the retrograde stage of the neighboring skarn deposit at Megalo Livadi. The main ore minerals at Koutalas are pyrite and chalcopyrite. Within the pyrite crystals, small inclusions of chalcopyrite occur along with pyrrotite and cubanite. As it is previously mentioned, cubanite is characteristic for high-temperature hydrothermal systems. Furthermore, the microthermometric analysis revealed homogenization temperatures between 168° and 550 °C with a peak at 350 °C. Unpublished LA-ICP-MS data in pyrite and chalcopyrite from both the sheeted veins and the skarn mineralization at Megalo Livadi revealed identical chemical composition and strongly suggest a genetic relationship between these types of ore mineralization.

Finally, the sulfide breccia and stockwork mineralization in the Heliport area present some different features from the sheeted veins. Here, the ore mineralogy is more complex with pyrite as a dominant phase in a quartz-dominated matrix. The pyrite crystals contain no pyrrotite and cubanite inclusions like the pyrite from the sheeted veins. Secondary chalcocite, probably after chalcopyrite, surrounds the pyrite crystals and bismuth sulfosalts and native bismuth, sharing similarities to the Megalo Livadi ores (Korosidis, 2019). The presence of Bi-bearing minerals at Heliport and the already discussed possible connection between the sheeted veins system at Koutalas and the skarn deposit at Megalo Livadi, suggest a common source, and a unified ore system in the whole western Serifos island. The Heliport area may correspond to a shallower part of the pluton-related porphyry-style system where the quartz stockwork veins occur. However, these parts are usually characterized by an extensive potassic alteration with secondary K-feldspar and biotite and such an alteration does not exist in the area.

In the southeastern part of the island, another igneous body exists, which is called in this study “aplogranite”. This rock consists of higher amounts of quartz and K-feldspar

and lower amounts of plagioclase than the granodiorite, minor amounts of biotite and apatite, while hornblende is absent. Zircon, monazite and ilmenite also occur as accessory minerals. All these minerals are quite fresh. The aplogranite hosts a disseminated pyrite mineralization in two different locations, the first one in the Sotiras area in the southeastern part and the second one in the Kefala area in the central-southcentral part. In the Sotiras area, large veins of hydrothermal quartz also occur.

For the genesis of this igneous body, two main scenarios can be proposed. The first scenario implies its origin through fractionation from a unique magmatic source. This primitive magma corresponds either to the inner part of the granodiorite or to the mafic enclaves which are found dispersed within the granodiorite. Successive fractionation of this diorite-andesite primitive magma leads first to the creation of the quartz monzodiorite in the inner part, to the granodiorite in the outer part and to the monzogranite-syenogranite, here called aplogranite, as the last product.

The second scenario suggests the existence of two different igneous bodies from two different magmatic sources. The first one is the oxidized magnetite-series I-type granodiorite, which is distinguished into one more primitive inner part in the center and one more evolved outer part on the rim, with a clear boundary between them. The second igneous body is one more reduced ilmenite-series more S- than I-type aplogranite. In Koutalas area the aplogranite has been intruded within a sodic altered granodiorite and it is further testified by the CI images that the aplogranite has not been affected by the sodic alteration as the granodiorite. It is obvious, that the emplacement of the aplogranite postdates the sodic alteration of the granodiorite. This further suggests that aplogranite magmas at Serifos, may result in a distinct style of ore assemblages and do not form part of the same granite-related system affecting the granodiorite.

It is suggested here, that the aplogranite-hosted mineralization shares some features similar with the so-called reduced intrusion-related systems. Some of these features could be the more reduced character of the rock which is testified by the presence of ilmenite instead of magnetite, the presence of double bubble CO₂ fluid inclusions within the quartz veins and a disseminated-type pyrite-molybdenite along with miarolitic cavities mineralization. These systems are believed to be related to Au, Mo, W and Sn deposits (Lang et al 200, Baker et al 2005) where the contribution of the lithophile elements originated from the continental crust is of high importance.

The results from the fluid inclusion microthermometry have shown that the granodiorite-hosted sheeted veins mineralization took place in a temperature range from 250° to 550°C, while the hydrothermal quartz veins within the aplogranite were formed at similar but somehow lower temperatures from 250° to 450°C. As far as the measured salinities is concerned, two main groups can be distinguished. The first one high-salinity group, corresponds to salinities in the range from 28 to 47 wt% NaCl equiv. The second group corresponds to lower salinities ranging from 5 to 24 wt% NaCl equiv. This group is here called low-salinity group. Fluid inclusions from both the granodiorite and the aplogranite are projected in these two groups.

In order to explain the data shown above, one can assume that a single-phase magmatic fluid separates and as a result one hypersaline liquid-rich phase and one vapor-rich low-

salinity phase will form. As the temperature of the whole system was decreasing (decrease of the homogenization temperature) the continuing boiling of the system lead to a further phase separation of the liquid-rich, high-salinity inclusion into one liquid-rich but lower salinity and one vapor-rich low-salinity groups, while simultaneously the decrease of the temperature lead to a salinity decrease.

Another possible explanation for the coexistence of liquid-rich halite bearing- and vapor rich fluid inclusions could be the model described by Monecke et al. (2018). In this model, as the pluton reached the ductile-brittle transition depth (from lithostatic to hydrostatic conditions) two fluid phases are present. The first one is a liquid-rich high-salinity phase with one salt crystal while the second one is a vapor-rich low-salinity phase. As the fluid moves upwards, the temperature and pressure decrease lead to a dramatically SiO_2 solubility decrease and as a result quartz finally precipitates leading to the formation of the sheeted vein system.

Taking all these into account, the existence of two different igneous bodies in Serifos island is proposed as the main model. A supercritical liquid of low salinity may be the original fluid for the deposition of the ore minerals inside the sheeted veins, where phase separation could had taken place with the creation of one high-density hypersaline liquid-rich phase and one low-density vapor-rich phase as a result. Further phase separation of this liquid-rich phase with simultaneous temperature dropping could lead to the deposition of the ore minerals of the sheeted veins in a 250-550°C temperature range. The vapor-rich phase is migrating upwards as a lower density phase. This moderate temperature liquid-rich phase responsible for the deposition of the ore minerals of the sheeted veins could be also responsible for the deposition of the hydrothermal quartz veins within the aplogranite in the Sotiras area. However, fluid inclusion petrography has shown a different composition for this fluid containing in some cases double bubbled CO_2 inclusions and solid phases not observed within the sheeted veins. Therefore, a different fluid originated from a deeper and/or a more reduced environment must be responsible for the hydrothermal activity in the area.

V. Conclusions

1. The coexistence of two different igneous bodies is proposed as the main model of this study
2. The emplacement of the aplogranite into the granodiorite is a later event than the sodic alteration which has affected the outer granodiorite therefore, the aplogranite is a younger body than the granodiorite
3. The sheeted veins system along with the extensive sodic alteration in the Koutalas area may represent the deeper part of one single granite-related porphyry system, where the sulfide stockwork mineralization is either at a shallower part of the same system or it is independent of it.
4. One supercritical magmatic fluid may be responsible for the deposition of the ore minerals from the sheeted veins via phase separation, into one high-density liquid-rich and one low-density vapor-rich phase.
5. This liquid-rich fluid may be also responsible for the deposition of the ore minerals in the southwestern skarn deposit via migration from the sheeted veins into the hosting marbles of the Cycladic Blueschist Unit (proximal skarn).
6. A hydrothermal fluid of different chemical composition (solid phases) and of different origin (a deeper and/or a more reduced environment) might be responsible for the formation of the hydrothermal quartz veins and the disseminated mineralization within the aplogranite in the Sotiras area in the southeastern part of the island. This might be a different hydrothermal system more like the intrusion-related systems which host some of the largest Mo, W and Sn deposits in the world.
7. Serifos mines share some similarities to both porphyry and reduced intrusion related gold systems (ilmenite-series igneous rocks, miarolitic cavities mineralization, aqueous-carbonic fluids, etc).

References

- Alfieris, D., Voudouris, P., Spry, P.G., 2013. Shallow submarine epithermal Pb-Zn-Cu-Au-Ag-Te mineralization on western Milos Island, Aegean Volcanic Arc, Greece: mineralogical, geological and geochemical constraints. *Ore Geol. Rev.* 53, 159-180.
- Ayati F., Yavuz F., Noghreyan M., Haroni H.A., Yavuz R., 2008, Chemical characteristics and composition of hydrothermal biotite from the Dalli porphyry copper prospect, Arak, central province of Iran, *Miner Petrol* 94:107-122
- Azadi M., Mirmohammadi M., Hezarkhani A., 2014, Aspects of magmatic-hydrothermal evolution of Kahang porphyry copper deposit, Central Iran, *Arab J Geosciences* DOI 10.1007/s12517-014-1528-2
- Baker T., Pollard P.J., Mustard R., Mark G., Graham J.L., 2005, A Comparison of Granite-related Tin, Tungsten, and Gold-Bismuth Deposits: Implications for Exploration, *SEG Newsletter* 61, 5-17
- Bissig T., Cooke R. D., 2014, Introduction to the special Issue Devoted to Alkalic Porphyry Cu-Au and Epithermal Au Deposits, *Economic Geology*, 109, 4., 819-825
- Blundy J., Mavrogenes J., Tattitch B., Sparks S., Gilmer A., 2015, Generation of porphyry copper deposits by gas-brine reaction in volcanic arcs, *Nature Geoscience* (2015), DOI: 10.1038/NGEO2351
- Bonsall, T.A., Spry, P.G., Voudouris, P., Tombros, S., Seymour, K., Melfos, V., 2011. The geochemistry of carbonate-replacement Pb-Zn-Ag mineralization in the Lavrion district, Attica, Greece: fluid inclusion, stable isotope, and rare earth element studies. *Econ. Geol.* 106, 619-651.
- Campos A. E., Touret L.R. J., Nikogosian I., 2006, Magmatic Fluid Inclusions from the Zaldivar Deposit, Northern Chile: The role of early Metal-bearing Fluids in a Porphyry Copper System, *Resource Geology*, 56, 1, 1-8
- Cesare B., Satish-Kumar M., Cruciani G., Pocker S., Nodari L., 2008, Mineral chemistry of Ti-rich biotite from pegmatite and metapelitic granulites of the Kerala Khondalite Belt (southeast India): Petrology and further insight into titanium substitutions, *American Mineralogist*, 93, 327-338
- Chang Z., Hedenquist W. J., White C. N., Cooke R. D., Roach M., Deyell L. C., Joey Garcia Jr., Gemell J. Bruce, McKnight Stafford, Cuison Liza Ana, 2011, Exploration Tools for Linked Porphyry and Epithermal Deposits: Example from the Mankayan Intrusion-Centered Cu-Au District, Luzon, Philippines, *Economic Geology*, 106, 1365-1398

- Corbett G. J., Leach T.M., 1997, Southwest Pacific Rim, Gold-Copper Systems: Structure, Alteration and Mineralization
- Corbett G., 2004, Epithermal and Porphyry Gold- Geological Models
- Ducoux M., Branquet Y., Jolivet L., Arbaret L., Grasemann B., Rabillard A., Gumiaux C., Drufin S., 2017, Synkinematic skarns and fluid drainage along detachments: The West Cycladic Detachment System on Serifos Island (Cyclades, Greece) and its related mineralization, *Tectonophysics* 695 1-26
- Einaudi T. M., 1997, Mapping Altered and Mineralized Rocks, an introduction to the "Anaconda Method"
- Fitros M., Tombros F. S., Williams-Jones E. A., Tsikouras B., Koutsopoulou E., Hatzipanagiotou K., 2017, Physicochemical controls on bismuth mineralization: An example from Moutoulas, Serifos Island, Cyclades, Greece, *American Mineralogist*, 102, 1622-1631
- Fornadel P. A., Spry G. P., Melfos V., Vavelidis M., Voudouris Ch. P., 2011, Is the Palea Kavala Bi-Te-Pb-Sb±Au district, northeastern Greece, an intrusion-related system? , *Ore Geology Reviews* 39, 119-133
- Ginibre C., Kronz A., Worner G., 2002, High-resolution quantitative imaging of plagioclase composition using accumulated backscattered electron images: new constraints on oscillatory zoning, *Contrib Miner Petrol* 142: 436-448
- Ginibre C., Worner G., Kronz A., 2002, Minor- and trace-element zoning in plagioclase: implications for magma chamber processes at Parinacota volcano, northern Chile, *Contrib Miner Petrol* 143: 300-315
- Ginibre C., Worner G., Kronz A., 2007, Crystal Zoning as an Archive for Magma Evolution, *Elements*, 3, 261-266.
- Goldstein H. R., Reynolds T. J., 1994, Systematic of fluid inclusions in diagenetic minerals, *SEPM (Society for Sedimentary Geology) Short Course* 31
- Halley S., Dilles H. J., Tosdal M. R., 2015, Footprints: Hydrothermal Alteration and Geochemical Dispersion Around Porphyry Copper Deposits, *SEG Newsletter*, 100, 1-17
- Hawthorne C. F., Oberti R., 2007, Amphiboles: Crystal Chemistry, *Reviews in Mineralogy & Geochemistry*, Vol.67, pp. 1-54
- Hawthorne C. F., Oberti R., 2007, Classification of the Amphiboles, *Review in Mineralogy & Geochemistry*, 67, 55-88

- Holiday J.R., Cooke D.R., 2007, Advances in Geological Models and Exploration Methods for Copper± Gold Porphyry Deposits, *Ore Deposits and Exploration Technology*, 53, 791-809
- Hollings P., Cooke R. D., Waters J. P., Cousens B., 2011, Igneous Geochemistry of Mineralized Rocks of the Baguio District, Philippines: Implications for Tectonic Evolution and the Genesis of Porphyry-Style Mineralization, *Economic Geology*, 106, 1317-1333
- Hovelmann J., Putnis A., Geisler T., Schmidt C. B., Golla-Schindler U., 2010, The replacement of plagioclase feldspars by albite: observations from hydrothermal experiments, *Contrib Miner Petrol* 159: 43-59
- Hurtig C. N., Williams-Jones E. A., 2015, Porphyry- Epithermal Au-Ag-Mo ore formation by vapor-like fluids: New insights from geochemical modeling, *Geological Society of America ???????*
- Iglseder C., Grasemann, B., Schneider, D.A., Petrakakis, K., Miller, C., Klötzli, U.S., Thöni, M., Zámolyi, A., Rambousek, C., 2009. I and S-type plutonism on Serifos (W-Cyclades, Greece). *Tectonophysics* 473, 69–83.
- Imai A., Nagai Y., 2009, Thematic Article: Fluid Inclusion study and Opaque Mineral Assemblage at the Deep and Shallow Part of the Batu Hijau Porphyry Copper-Gold Deposit, Sumbawa, Indonesia, *Resource Geology*, 59, 3: 231-243
- Imai A., Ohno S., 2005, Primary Ore Mineral Assemblage and Fluid Inclusion Study of the Batu Hijau Porphyry Cu-Au Deposit, Sumbawa, Indonesia, *Resource Geology*, 55, 3, 239-248
- Imai A., 2000, Mineral Paragenesis, Fluid Inclusions and Sulphur Isotope Systematics of the Lepanto Far Southeast Porphyry Cu-Au Deposit, Mankayan, Philippines, *Resource Geology*, 50, 3, 151-168
- Jensen P. E., Barton D. M., 2000, Chapter 8, Gold Deposits Related to Alkaline Magmatism, *SEG Reviews*, 13, 279-314
- Jolivet, L., Faccenna, C., Huet, B., Labrousse, L., Le Pourhiet, L., Lacombe, O., Lecomte, E., Burov, E., Denele, Y., Brun, J.-P., Philippon, M., Paul, A., Salaun, G., Karabulut, H., Piromallo, C., Monie, P., Gueydan, F., Okay, .I., Oberhansli, R., Pourceau, A., Augier, R., Gadenne, L., Driussi, O., 2013. Aegean tectonics: strain localization, slab tearing and trench retreat. *Tectonophysics* 597, 1-33.
- Korosidis G. (2019) Distal Fe-Cu-W-Bi-Au skarn deposits of Serifos Island: New petrographical, mineralogical and geochemical constrains on the retrograde ore evolution. Master thesis, National and Kapodistrian University of Athes, 84p.

- Kouzmanov K., Pettke T., Heinrich A. C., 2010, Direct Analysis of Ore-Precipitating Fluids: Combined IR Microscopy and LA-ICP-MS Study of Fluid Inclusions in Opaque Ore Minerals, *Economic Geology*, 105, 351-373
- Kouzmanov, K., Pokrovski, G.S., 2012. Hydrothermal controls on metal distribution in porphyry Cu (-Mo-Au) systems. *Soc. Econ. Geol. Spec. Publ.* 16, 573-618.
- Landtwing R. M., Furrer C., Redmond B. Pa., Pettke T., Guillong M., Heinrich A. C., 2009, The Bingham Canyon Porphyry Cu-Mo-Au Deposit. III. Zoned Copper- Gold Ore Deposition by Magmatic Vapor Expansion, *Economic Geology*, 105, 91-118
- Lang R. J., Baker T., 2001, Intrusion-related gold systems: the present level of understanding, *Mineralium Deposita* 36: 477-489
- Lang R. J., Baker T., Hart J.R. C., Mortensen K. J., 2000, An exploration model for Intrusion-Related Gold Systems, *SEG Newsletter*, 40, 1- 15
- Leake B.E., Woolley A.R., Birch W.D., Burke E.A.J., Ferraris G., Grice J.D., Hawthorne F.C., Kisch H.J., Krivovichev V.G., Schumacher J.C., Stephenson N.C.N., Whittaker E.J.W., 2004, Nomenclature of amphiboles: additions and revisions to the International Mineralogical Association's Nomenclature, *Mineralogical Magazine*, February 2004, 68(1), 209-215
- Mao J., Pirajno F., Lehmann B., Luo M., Berzina A., 2013, Distribution of porphyry deposits in the Eurasian continent and their corresponding tectonic settings, *Journal of Asian Earth Sciences* 79 (2014) 576-584
- Martin F. R., 2007, Amphiboles in the Igneous Environment, 67, 323-358
- Marinos G, Petrascheck W.E (1956) Lavrion. Institute for geology and subsurface research. *Geol Geophys Res* 4: 1-247
- Melfos, V., Voudouris, P., 2017. Cenozoic metallogeny of Greece and potential for precious, critical and rare metals exploration. *Ore Geol. Rev.* 59, 1030-1057.
- Menant, A., Jolivet, L., Tuduri, J., Loiselet, C., Bertrand, G., Guillou-Frottier, L., 2018. 3D subduction dynamics: a first-order parameter of the transition from copper- to gold rich deposits in the eastern Mediterranean region. *Ore Geol. Rev.* 94, 118-135.
- Mercer N. C., Reed H. M., 2013, Porphyry Cu-Mo Stockwork Formation by Dynamic, Transient Hydrothermal Pulses: Mineralogic Insights from the Deposit at Butte, Montana, *Economic Geology*, 108, 1347-1377
- Monecke T., Monecke J., Reynolds T. J., Tsuruoka S., Bennett M. M., Skewes B. W., Palin M. R., 2018, Quartz Solubility in the H₂O-NaCl System: A Framework for

- Understanding Vein Formation in Porphyry Copper Deposits, *Economic Geology*, 113, No5
- Monecke T., Monecke J., Reynolds T. J., 2019, The influence of CO₂ on the solubility of quartz in single-phase hydrothermal fluids: Implications for the formation of stockwork veins in porphyry copper deposits, *Economic Geology*, 114, 6, 1195-1206
- Moritz R., Benkhelfa F., 2009, Fluids in High-Sulfidation Epithermal ore deposits: Constraints from Infrared Microthermometry of Enargite-Hosted Fluid Inclusions, *Proceedings of the Tenth Biennial SGA Meeting*, Townsville, 2009
- Moshefi P., Hosseinzadeh M. R., Moayyed M., Lentz R. D., 2018, Comparative study of mineral chemistry of four biotite types as geochemical indicators of mineralized and barren intrusions in the Sungun Porphyry Cu-Mo deposit, northwestern Iran, *Ore Geology Reviews* 97, 1-20
- Muller A., Herrington R., Armstrong R., Seltmann R., Kirwin J. D., Stenina G. N., Kronz A., 2010, Trace elements and cathodoluminescence of quartz in stockwork veins of Mongolian porphyry-style deposits, *Mineral Deposita* 45: 707-727
- Nakata M., Komuro K., 2010, Chemistry and Occurrences of Native Tellurium from Epithermal Gold Deposits in Japan, *Resource Geology*, 61, 3:211-223
- Neubauer F (2005) Structural control of mineralization in metamorphic core complexes. In: Mao J, Bierlein FP (eds) *Mineral deposit research: meeting the global challenge*, Springer, Berlin-Heidelberg, pp 561–564
- Ortelli M., Moritz R., Voudouris P., Spangenberg J., 2009, Tertiary Porphyry and Epithermal Association of the Sapes-Kassiteres District, Eastern Rhodopes, Greece, *Proceedings of the Tenth Biennial SGA Meeting*, Townsville, 2009
- Parsons I., Magge W. C., Allen M. C., Shelley J.M.G., Lee R. M., 2009, Mutual replacement reactions in alkali feldspars II: trace element partitioning and geothermometry, *Contrib Mineral Petrol* 157: 663-687
- Penniston-Dorland C. S., 2001, Illumination of vein quartz textures in a porphyry copper ore deposit using scanned cathodoluminescence: Grasberg Igneous Complex, Irian Jaya, Indonesia, *American Mineralogist*, 86, 652-666
- Perello J., Carlotto V., Zarate A., Ramos P., Posso H., Neyra C., Caballero A., Fuster N., Muhr R., 2003, Porphyry-style Alteration and Mineralization of the Middle Eocene to Early Oligocene Andahuaylas- Yauri Belt, Cuzco Region, Peru, *Economic Geology*, 98, 1575-1605

- Pettke T., Oberli F., Heinrich A. C., 2009, The magma and metal source of giant porphyry-type ore deposits, based on lead isotope microanalysis of individual fluid inclusions, *Earth and Planetary Science Letters* 296, 267-277
- Pietranik A., Koepke J., 2009, Interactions between dioritic and granodioritic magmas in mingling zones: plagioclase record of mixing, mingling and subsolidus interactions in the Gesinieć Intrusion, NE Bohemian Massif, SW Poland, *Contrib Mineral Petrol* 158: 17-36
- Redmond B. P., Einaudi M., 2010, The Bingham Canyon Porphyry Cu-Mo-Au Deposit. I. Sequence of Intrusions, Vein Formation, and Sulfide Deposition, *Economic Geology*, 105, 43-68
- Richards P. J., 2014, Tectonic, magmatic, and metallogenic evolution of the Tethyan orogen: From subduction to collision, *Ore Geology Reviews* (2014)
- Richards P. J., 2014, The oxidation state, and sulfur and Cu contents of arc magmas: implications for metallogeny, *Lithos* (2014)
- Richards P. J., 2011, Magmatic to hydrothermal metal fluxes in convergent and collided margins, *Ore Geology Reviews* 40, 1-26
- Rusk G. B., Reed H. M., Dilles H. J., 2008, Fluid inclusion evidence for Magmatic-Hydrothermal Fluid Evolution in the porphyry Copper-Molybdenum Deposit at Butte, Montana, *Economic Geology*, 103, 307- 334
- Rusk B., Reed M., 2002, Scanning Electron microscope-cathodoluminescence analysis of quartz reveals complex growth histories in veins from the Butte porphyry copper deposit, Montana, *Geology*, 30, 727-730
- Rusk B., Reed M., Krinsley D., Bignall G., Tsuchiya N., Natural and Synthetic Quartz Growth and Dissolution Revealed by Scanning Electron Microscope Cathodoluminescence, 14th International Conference on the Properties of Water and Steam in Kyoto
- Salemink, J., 1985. Skarn and ore formation at Seriphos, Greece as a consequence of granodiorite intrusion. *Geol. Untr.* 40, 231.
- Scheffer, C., Tarantola, A., Vanderhaeghe, O., Voudouris, P., Rigaudier, T., Photiadis, A., Morin, D., Alloucherie, A., 2017. The Lavrion Pb-Zn-Fe-Cu-Ag detachment-related district (Attica, Greece): structural control on hydrothermal flow and element transfer-deposition. *Tectonophysics* 717, 607-627.
- Seedorff E., Barton D. M., Stavast J.A. W., Maher J. D., 2008, Root zones of Porphyry Systems: Extending the Porphyry Model to Depth, *Economic Geology*, 103, 939-956

- Seedorff, E., Dilles, J.H., Proffett, J.M., Einaudi, M.T., Zurcher, L., Stavast, W.J.A., Johnson, D.A., Barton, M.D., 2005. Porphyry deposits: characteristics and origin of hypogene features. *Econ. Geol.* 100, 251-298.
- Selby D., Nesbitt E. B., 2000, Chemical composition of biotite from the Casino Porphyry Cu-Au-Mo mineralization, Yukon, Canada: evaluation of magmatic and hydrothermal fluid chemistry, *Chemical Geology* 171 (2000) 77-93
- Sillitoe H. Richard, 2008, Major Gold Deposits and Belts of the North and South American Cordillera: Distribution, Tectonomagmatic Settings, and Metallogenic Considerations, *Economic Geology*, 103, 663-687
- Sillitoe H. R., 2010, Porphyry Copper Systems, *Economic Geology*, 105, 3-41
- Skarpelis N (2002) Geodynamics and evolution of the Miocene mineralization in the Cycladic-Pelagonian belt, Hellenides. *Bull Geol Soc Greece* 34: 2191–2206
- Stouraiti C., Baziotis I., Asimow P.D., Downes H., 2017, Geochemistry of the Serifos calc-alkaline granodiorite pluton, Greece: constraining the crust and mantle contributions to I-type granitoids, *International Journal of Earth Sciences*, <https://doi.org/10.1007/s00531-017-1565-7>
- Thompson J.F.H., Sillitoe R.H., Baker T., Lang J.R., Mortensen J.K., 1999, Intrusion-related gold deposits associated with tungsten-tin provinces, *Mineralium Deposita* 34: 323-334
- Tschegg C., Grasemann B., 2009, Deformation and alteration of a granodiorite during low-angle normal faulting (Serifos, Greece), *Lithosphere* 1, 139-154
- Tombros, S., St. Seymour, K., Spry, P.G., Williams-Jones, A., 2007. The genesis of epithermal Au-Ag-Te mineralization, Panormos Bay, Tinos Island, Cyclades, Greece. *Econ. Geol.* 102, 1269–1294.
- Ulrich T., Heinrich A. Christoph, 2002, Geology and Alteration Geochemistry of the Porphyry Cu-Au Deposit at Bajo de la Alumbrera, Argentina, *Economic Geology*, 97, 1865-1888
- Voudouris, P., Melfos, V., Spry, P.G., Bonsall, T., Tarkian, M., Economou-Eliopoulos, M., 2008a. Mineralogical and fluid inclusion constraints on the evolution of the Plaka intrusion-related ore system, Lavrion, Greece. *Mineral. Petrol.* 93, 79–110.
- Voudouris, P., Melfos, V., Spry, P.G., Bonsall, T., Tarkian, M., Solomos, Ch., 2008b. Carbonate-replacement Pb-Zn-Ag±Au mineralization in the Kamariza area,

- Lavrion, Greece: mineralogy and thermochemical conditions of formation. *Mineral. Petrol.* 94, 85–106.
- Voudouris, P., Melfos, V., Moritz, R., Spry, P.G., Ortelli, M., Kartal, T., 2010. Molybdenite occurrences in Greece: mineralogy, geochemistry and depositional environment. In: Christofides, G. (Ed.), *Proceedings of the XIX Congress of the Carpathian-Balkan Geological Association, Thessaloniki*. *Scientific Annals of the School of Geology A.U.Th.* 100, pp. 369–378.
- Voudouris, P., Spry, P.G., Sakellaris, G.A., Mavrogonatos, C., 2011b. A cervelleite-like mineral and other Ag-Cu-Te-S minerals [Ag₂CuTeS and (Ag, Cu)₂TeS] in gold-bearing veins in metamorphic rocks of the Cycladic Blueschist Unit, Kallianou, Evia Island, Greece. *Mineral. Petrol.* 101, 169–183.
- Voudouris P, Mavrogonatos C, Spry PG, Baker T, Melfos V, Klemd R, Haase K, Repstock A, Djiba A, Bismayer U, Tarantola A, Scheffer C, Moritz R, Kouzmanov K, Alfieris D, Papavassiliou K, Schaarschmidt A, Galanopoulos E, Galanos E, Kołodziejczyk J, Stergiou C, Melfou M. (2019) Porphyry and epithermal deposits in Greece: an overview, new discoveries, and mineralogical constraints on their genesis. *Ore Geol. Rev* 107, 654-691.
- Wilkinson J. J., 2013, Triggers for the formation of porphyry ore deposits in magmatic arcs, *Nature Geoscience*, DOI: 10.1038/NGEO1940
- Xu X.-W., Mao Q., Li X.H., Pirajno M. F., Qu X., Deng G., Chen D.Z., Zhang B.L., D. L.H., 2013, Copper-zinc albite porphyry in the Hersai porphyry copper deposit, East Junggar, China: A transition between late magmatic and hydrothermal porphyry copper deposit, *Ore Geology Reviews* 61, 141-156
- Zajacz Z., Seo Jung H., Candela A. P., Piccoli M. P., Heinrich A. C., Guillong M., 2010, Alkali metals control the release of gold from volatile-rich magmas, *Earth and Planetary Science Letters* 297, 50-56
- Παπανικολάου Ι. Δ., 2015, Γεωλογία της Ελλάδας, Τεκτονική δομή και Παλαιογεωγραφική-Παλαιογεωδυναμική Εξέλιξη, σελ. 168-175, 234-239, 360-363